Universidad Carlos III de Madrid
www.uc3m.es

TESIS DOCTORAL

Design and development of a multi-wavelength optoacoustic system based on high-power diode laser sources. Optoacoustic signal generation with nanoparticles for biomedical applications

Diseño y desarrollo de un sistema optoacústico de múltiples longitudes de onda basado en fuentes de diodos láseres de alta potencia. Generación de señales optoacústicas con nanoparticulas para aplicaciones biomédicas

Autor:

Luca Leggio

Directores:

Prof. Horacio Lamela Rivera

Prof. Guillermo Carpintero del Barrio

DEPARTAMENTO DE TECNOLOGÍA ELECTRÓNICA

Leganés, Septiembre 2017

Universidad Carlos III de Madrid
www.uc3m.es

TESIS DOCTORAL

Design and development of a multi-wavelength optoacoustic system based on high-power diode laser sources. Optoacoustic signal generation with nanoparticles for biomedical applications

Autor: ***Luca Leggio***

Directores: **Prof. Horacio Lamela Rivera**

Prof. Guillermo Carpintero del Barrio

Firma del Tribunal Calificador:

		Firma
Presidente:	_____	_____
Vocal:	_____	_____
Secretario:	_____	_____
Calificación:	_____	_____

Leganés, de de

Acknowledgements

First of all, I would like to express my gratitude to my thesis directors, Professor Horacio Lamela and Professor Guillermo Carpintero, who have been my supervisors since the beginning of my work here in University Carlos III of Madrid, giving me the opportunity to come here to perform my doctoral studies and acquire new knowledge, both scientific and human, and allowing me working in a dynamic and passionate group of people. They provided me with constant encouragement and constructive advices that have motivated me in the continuation of my studies here, despite the many difficulties. I would like to acknowledge the scientific collaboration of Professor Marek Osiński, the personnel of the Department of Electronic Technology and all the colleagues of OILTEBIA project for the time shared together during the events of the project.

I had the occasion to grow up scientifically thanks to the guidance and support of my supervisors. I also want to thank my colleagues who have collaborated significantly with me in the lab during these years: Daniel, Omar, Ehsan, Sandeep, Miguel, Sergio, and finally Bartosz. I appreciate all their contributions of work and ideas that have been useful for my publications, but also their friendship. I also could not forget the sincere and joyful friendship of Julio and Guillermo, with whom I spent pleasant time after work.

I am grateful with my parents Gianfranco and Mara for their great and unequivocal encouragement during these years. They supported and motivated me unconditionally during my studies. I also thank my lovely grandmother Bruna for giving me her affection despite not having shared so much time together during the last five years.

I am grateful with all my close relatives for having believed in me and demonstrated their affection.

To my soul friends Fabio, Luca L., Luca F., Andrea, Dario, Marco, and Roberto for having always given me their friendship, sincerity and support in every meeting in Rome.

Finally, I would like to express my special thanks to my wife Maria Belen for her love, patience and encouragement during all these years, without which I would not have been able to reach this stage of my life.

You have supported and motivated me every day of this great experience. Thank you for giving me many reasons to reach the end of this adventure together.

It was a pleasure having made this journey with you all.

Agradecimientos

En primer lugar quisiera expresar mi agradecimiento a mis directores de tesis, Profesor Horacio Lamela y Profesor Guillermo Carpintero, que han sido mis supervisores desde el comienzo de mi trabajo aquí en la Universidad Carlos III de Madrid, brindándome la oportunidad de estar aquí para realizar mis estudios de doctorado y adquirir nuevos conocimientos, tanto científicos como humanos. Especialmente permitiéndome trabajar en un grupo dinámico y apasionado de gente y a su vez proporcionando un estímulo constante y consejos constructivos que me han motivado en la continuación de mis estudios, a pesar de los obstáculos. Quiero agradecer la colaboración científica del Profesor Marek Osiński, al personal del Departamento de Tecnología Electrónica y a todos los colegas del proyecto OILTEBIA por el tiempo compartido juntos en los eventos del proyecto.

He tenido la oportunidad de crecer científicamente gracias a la orientación y el apoyo de mis supervisores. También quiero agradecer a mis compañeros del laboratorio que colaboraron significativamente conmigo en estos años: Daniel, Omar, Ehsan, Sandeep, Miguel, Sergio y finalmente Bartosz. Aprecio todas sus contribuciones de trabajo e ideas que han sido útiles para mis publicaciones, pero también su amistad. Tampoco puedo olvidar la sincera y alegre amistad de Julio y Guillermo, con quienes he pasado un tiempo agradable después del trabajo.

Estoy agradecido con mis padres Gianfranco y Mara por su gran e inequivocable aliento durante estos años. Por haberme apoyado y motivado incondicionalmente a lo largo de mis estudios; del mismo modo agradezco a mi abuela amorosa Bruna por brindarme su cariño a pesar de no haber compartido tanto tiempo junto durante los últimos cinco años. Agradezco a todos mis familiares cercanos por haber creído en mí y demostrado su afecto.

A mis amigos del alma Fabio, Luca L., Luca F., Andrea, Dario, Marco y Roberto por siempre haberme brindado su amistad, sinceridad y apoyo en cada rencuentro en Roma.

Por último, quisiera expresar mi agradecimiento especial a mi esposa María Belén por su amor, paciencia y aliento durante todos estos años, sin la cual no habría podido llegar a esta etapa de mi vida.

Tú me has apoyado y motivado cada día de esta gran experiencia. Gracias por darme muchas razones para llegar al final de esta aventura juntos.

Ha sido un placer haber hecho este viaje con todos vosotros.

Abstract

Over last few years, the rapid growth of optical technologies for biomedical imaging makes possible to reveal important biological information of tissues from light-tissue interaction. The emerging interest on new biomedical imaging techniques is motivated by the necessity to detect malignant cells and other diseases at early growth stages. The limited penetration depth of optical energy in biological media is primarily due to the high level of optical scattering. In addition, the diffusion of light in biological tissues limits the spatial resolution of the images acquired. The optoacoustic technique overcomes these issues combining the high contrast of optical imaging with the high spatial resolution of ultrasound systems in deep tissues. As well, the low scattering of the ultrasound waves produced in the biological tissues facilitates the acquisition of high-resolution images.

Two more important aspects to be considered in optoacoustic applications for a functional imaging are the use of optical contrast agents to increase the absorption of optical energy in those areas where the scattering is dominant, and the amount of optical energy delivered by laser sources to penetrate in depth. The necessity of compact and cost-effective laser sources with the characteristics required by optoacoustic applications has encouraged the studies presented in this thesis, proposing the use of high-power diode lasers instead of the classical solid state lasers.

Generally, solid-state lasers like Nd:YAG and optical parametric oscillators are used for the generation of optoacoustic signals, but their use in clinical environment is limited by their high costs, low repetition rates and bulky sizes. On the other hand, high-power diode lasers emerge as a potential alternative, due to their relatively low costs, high repetition rates required for fast image acquisition and compact sizes. However, the power of high-power diode lasers is still relatively low compared to solid-state lasers and for this reason they need to be combined in arrays to reach the amount of the optical power required for optoacoustic applications.

An optoacoustic setup based on small arrays of high-power diode lasers has been implemented and improved along the studies presented in this thesis. Optoacoustic experiments have been performed at different wavelengths using several kinds of absorbers hosted in a quartz cuvette or embedded within a phantom that simulates the optical scattering of a soft tissue. Solutions of carbon nanotubes, graphene oxide and gold nanorods have been used as absorbers in the experiments. The first experiments done in free space to focus the light in the absorbers have been improved by using optical fibers in a second stage.

Lastly, some commercially available diode laser bars have been proposed to replace the high-power diode lasers with the aim to increase the optical power for future implementations in the optoacoustic systems. Optical simulations have demonstrated the possibility to focus the beam of diode laser bars operating at different wavelengths into optical fibers by means of cylindrical microlenses. In a second step, the diode laser bars have been assembled together to simulate a multi-wavelength system. The beams have been combined by dichroic mirrors and focused in a multi-mode optical fiber. This research work has opened up new lines of investigation in the development of high-power laser sources for optoacoustic endoscopy and tomography in biomedical applications.

Resumen

Durante los últimos años, el rápido avance de las tecnologías ópticas para la obtención de imágenes biomédicas hace posible revelar importantes informaciones biológicas a partir de la interacción entre la luz y el tejido. El interés emergente en nuevas técnicas de obtención de imágenes biomédicas está motivado por la necesidad de detectar células malignas y otras enfermedades durante las etapas precoces de evolución. La limitada profundidad de penetración de la energía óptica en medios biológicos se debe principalmente al alto nivel de dispersión óptica. Además, la difusión de la luz en los tejidos biológicos limita la resolución espacial de las imágenes adquiridas. La técnica optoacústica sobresale estos problemas combinando el alto contraste de la imagen óptica con la alta resolución espacial de los sistemas de ultrasonido en los tejidos profundos. Asimismo, la baja dispersión de las ondas ultrasónicas producidas en los tejidos biológicos facilita la adquisición de imágenes de alta resolución.

Dos importantes aspectos a considerar demás en las aplicaciones optoacústicas para una imagen funcional son el uso de agentes de contraste óptico para mejorar la absorción de energía óptica en aquellas áreas donde la dispersión es dominante y la cantidad de energía óptica suministrada por las fuentes láseres para penetrar en profundidad. La necesidad de fuentes láseres compactas y de bajo coste con las características requeridas por las aplicaciones optoacústicas ha impulsado los estudios presentados en esta tesis, proponiendo el uso de diodos láseres de alta potencia en lugar de los clásicos láseres de estado sólido.

Generalmente, los láseres de estado sólido como el Nd:YAG y los osciladores ópticos paramétricos se utilizan para la generación de señales optoacústicas, pero su uso en el ambiente clínico está limitado por sus altos costes, bajas frecuencias de repetición y tamaños voluminosos. Por otro lado, los diodos láseres de alta potencia emergen como una potencial alternativa, debido a sus relativamente bajos costes, altas frecuencias de repetición requeridas para una rápida adquisición de imágenes y tamaños compactos. Sin embargo, la potencia de los diodos láseres de alta potencia es todavía relativamente baja en comparación con los láseres de estado sólido y por esta razón se necesita combinarlos para conseguir la cantidad de potencia óptica requerida para las aplicaciones optoacústicas.

Un sistema optoacústico basado en diodos láseres de alta potencia ha sido implementado y mejorado a lo largo de los estudios presentados en esta tesis. Se han realizado experimentos optoacústicos a diferentes longitudes de onda utilizando varios tipos de absorbentes colocados en cubeta de cuarzo u hospedados dentro de un “phantom” que simula la dispersión óptica de un tejido blando. Soluciones de nanotubos de carbono, óxido de grafeno y nanoparticulas de oro se han utilizado como absorbentes a lo largo de los experimentos. Los primeros experimentos realizados en espacio libre para enfocar la luz en los absorbentes se han mejorado mediante el uso de fibras ópticas en una segunda etapa.

Por último, se han propuesto barras de diodos láseres comercialmente disponibles para sustituir los diodos láseres de alta potencia con el objetivo de aumentar la potencia óptica para futuras implementaciones en los sistemas optoacústicos. Las simulaciones ópticas han demostrado la posibilidad de enfocar el haz emitido por barras de diodos láseres de diferentes longitudes de onda en fibras ópticas por medio de microlentes cilíndricas.

En una segunda etapa, las barras de diodos láseres han sido ensambladas en un único sistema para simular un sistema de múltiples longitudes de onda. Los haces han sido combinados por medio de espejos dicroicos y enfocados en una fibra óptica multimodo. Este trabajo de investigación ha abierto nuevas líneas de investigación en el desarrollo de fuentes láser de alta potencia para la endoscopia optoacústica y la tomografía en aplicaciones biomédicas.

Contents

Index of figures

Index of tables

Chapter 1

Introduction

1.1.Introduction

The optoacoustic effect was first reported by Alexander Graham Bell and Summer Tainter in 1880 [1]. Later, Bell stated *"...sonorousness, under the influence of intermittent light, is a property common to all matter"* [2]. Almost 120 years after his original discovery, optoacoustic signal generation has found a wide range of applications in different fields for material characterization of solids [3], liquids [4] and gases [5, 6]. During the last 20 years, the use of optoacoustic techniques for biomedical applications has inspired a growing interest in the scientific community [7-14]. This is due to persistent demand, within the biomedical field, for real time, effective and minimally invasive (or completely non-invasive) diagnostic procedures which provide efficient therapeutic procedures. A quantitative analysis of the optical properties of biological tissues provides essential physiological information required for effective diagnosis.

Up to the present time, the most commonly used methods to determine the optical properties require invasive procedures and *in-vitro* techniques based on spectrophotometry [15], reflectance [16], fluorescence spectroscopy [17], Raman spectroscopy [18] and optoacoustics [19]. The principal reason for this *in-vitro* quantification is due to the high optical *scattering* of the tissue that surrounds the sample of interest. The potential benefits of an *in-vivo* non-invasive technique would be significant and helpful to speed up the therapeutic response times. *Absorption* and *scattering* are the two physical phenomenons that affect light propagation in biological media. Although both parameters are important, *scattering* is the dominant mechanism in healthy soft tissues [20], where the *absorption* is relatively low. The optical *absorption* in biomaterials is wavelength dependent [21]. This is because the *absorption* spectrum of tissue chromophores depends on their molecular composition: molecules absorb photons when the photons energy matches an interval between internal energy states.

In-vivo quantification of the spectral characteristics of tissue chromophores has been performed using *Diffuse Optical Spectroscopy* (DOS). This technique can simultaneously measure both light *absorption* and *scattering* in turbid media and biomaterials [22-26]. Generally, DOS technique is carried out within the visible range or near-infrared (NIR), and more specifically in diagnostic optical window, which contains the most important chromophores. DOS provides information regarding the concentration of functional tissues, hemodynamics, water content, and lipids. Clinical trials using this technique for breast cancer detection have reported a penetration depth in the order of 1 cm [27]. These procedures are based on the detection of the amplitude and phase of modulated and highly attenuated optical signals using high sensitive optical detectors. The optical attenuation of healthy tissues, where multiple events of *scattering* occur, is the main obstacle to the penetration depth, thus limiting the use of DOS technique [27].

Optoacoustic tomography (OAT), also known as photoacoustic tomography (PAT) [28, 29], is an emerging modality of biomedical imaging that allows minimally invasive (or completely non-invasive) visualization and quantification of soft tissues by using non-ionizing radiation. One of the major advantages of this method over the classical diagnostic techniques is the use of ultrasound generated with laser radiation that suffers from low *scattering*, thus allowing penetration depths of several centimeters in biological tissues [30]. OAT is a hybrid modality that is considered a valid alternative to the techniques commonly used for early stage cancer detection, since it combines the high contrast and spectroscopic specificity of the optical imaging techniques with the high spatial resolution of the ultrasound systems in deep tissues.

In fact, in OAT the light *scattering* does not affect the image resolution that instead is correlated to the characteristics of the optoacoustic signal. On the other hand, the power/energy losses due to the turbidity of the tissue are responsible for light and optoacoustic signal attenuation. For this reason, laser sources able to provide high energy per pulse (~ mJ) are required for optoacoustic techniques. OAT allows the visualization of optical contrasts in tissues between a few millimeters to several centimeters with typical resolutions of ultrasound techniques (i.e. ~10 μm to ~ 1 mm). As a consequence, OAT permits better tissue specificity if compared to the typical ultrasound techniques, thus allowing the detection of hemoglobin, lipids, water and other endogenous chromophores [7, 8]. Numerous studies have experimentally investigated the laser-excited OAT to detect chromophores within turbid tissues with different optical properties [31-37].

During the last few years, OAT has been increasingly employed in biomedical applications involving blood vessels visualization and blood oxygenation assessment [21], breast tumor detection [38-40], small animal imaging [41] and functional imaging [42]. Non-invasive *in-vivo* trials on the visualization of the dynamic and functional properties of the nervous system on rat models have been reported [41]. Clinical trials using OAT were capable to visualize 18 over 20 malignant lesions, suspected from mammography or ultrasound images, which were posteriorly confirmed after biopsy [43]. In addition, whole-body 3D imaging of mice has been demonstrated [44, 45]. In clinical applications requiring high resolution images of deep tissues, the optoacoustic techniques can only be used in combination with endoscopic techniques, due to the high optical attenuation of tissues.

OAT relies on the contrast between the optical *absorption* properties of a cancer tissue and the surrounding healthy tissues. For early cancer detection during the vascularization process, commonly referred to as angiogenesis, the optical properties of healthy and unhealthy tissues are similar, thus impeding the detection process [46, 47]. The presence of carcinomas and harmful microorganisms can be revealed with the support of nontoxic biodegradable contrast agents, whose absorption properties are prominent in the "diagnostic window" spectral range (600-1200 nm) where the biological tissues are relatively transparent [48, 49]. The main role of the optical contrast agents targeted to cancerous tissues is to significantly improve the optoacoustic signal detection by increasing the *absorption* of the laser energy [50-52]. Several *in-vivo* studies using gold nanorods have been performed on rats and have demonstrated a significant increase of image contrast [53-55].

Most OAT systems generally utilize expensive and bulky lasers for optical excitation, such as passively Q-switched Nd:YAG lasers. Moreover, to realize functional imaging, complex wavelength-tunable laser sources are usually employed with additional instruments, such as Ti:sapphire or dye lasers, or optical

parametric oscillators (OPOs). Pulsed high-power diode lasers (HPDLs) are very attractive for OAT applications due to their low cost, small size, high repetition rates, high efficiency, and compatibility with optical fibers, which enable reduction of optoacoustic instrumentation to a portable size [56-62]. Due to the danger of catastrophic degradation to laser facets, diode lasers suffer from peak power limitation, typically in the range of ~ 100-200 W, which limits the energy per pulse in the ns range to a few tens of μJ, compared to mJ level in the case of Nd:YAG lasers. This in turn limits the strength of the optoacoustic signal and the depth of three-dimensional OAT, and requires averaging over thousands of optoacoustic signals in order to achieve signal-to-noise ratios comparable to those produced by Nd:YAG lasers. One possible solution to this problem is to use combined power from synchronized multiple HPDLs [63, 64]. Initially, multiple HPDL sources were used for generating the optoacoustic response of ink samples in a biological phantom [63] and in blood vessel phantoms [58]. Recent implementations include utilization of diode laser stacks, with pulse energies exceeding 0.5 mJ, sufficient to perform in-vivo imaging of human vasculature [65-66]. An additional advantage of diode lasers is that they are available in a wide range of wavelengths, which is important for multiwavelength applications, for example in spectroscopic quantification of specific tissue chromophores such as oxygenated and deoxygenated hemoglobin [67], as well as in contrast agent analysis [68].

The research work presented in this thesis is dedicated to the design of an optoacoustic system based on high-power pulsed laser sources. Small arrays of HPDLs operating at 870 nm and 905 nm are combined side-by-side to generate optoacoustic signals from different absorbers (i.e. ink, carbon nanotubes, graphene oxide nanoparticles, and gold nanorods) embedded in quartz cuvette or phantom. These absorbers are chosen for their capability to be used as contrast agents in optoacoustic applications. Their geometrical and optical properties will be presented in this thesis. As first approach, the HPDLs are combined in a semicircular configuration focusing their beams in the absorbers. Successively, the beams of the HPDLs are combined and coupled to multimode optical fibers that are joined together in a 675-μm fiber bundle. The output of the fiber bundle illuminates the samples under test. In the last experiment with gold nanorods, a third wavelength (i.e. 972 nm) will be added to the optoacoustic system. The choose of optical fibers as beam coupling media is due to their capability of transmitting light at any distance, but also to their potential use in optoacoustic endoscopy (OAE). OAE is a novel biomedical imaging technique that allows OAT using a small probe to image the internal organs of the body [69-73]. Some *in-vivo* endoscopic imaging applications are early-stage detection of tumors [74], lipid detection [75, 76], gastroenterology, fetal medicine, and vascular interventional radiology [77, 78].

The high penetration depths and the high optical scattering of biological media require the use of powerful laser sources to generate sufficiently high optoacoustic signals. HPDLs should be combined in very large arrays to emit the same power levels of solid-state lasers, making the system bulky and expensive. In this regard, the use of alternative diode lasers sources would be necessary to overcome these limitations. Diode laser bars (DLB) are devices composed of large arrays of diode laser emitters, which are able to emit optical peak power of several hundreds of Watts. They are much more compact than HPDLs because they consist in a large number of emitters (normally 25-60) gathered in a small space (~ 1 mm), but require complex optical lenses for beam shaping. In the last part of this thesis it will be shown the modeling of some commercially available high-power DLBs by using the software Zemax. Their emission wavelengths lie in the near-infrared spectrum (i.e. 808 nm, 880 nm, 910 nm, 940 nm, and 980 nm). Their beams are efficiently coupled into 400-μm optical fibers by using optical microlenses taken from catalogue. Finally, the DLBs are simulated all together in a single design where their optical beams

are first collimated, and after combined in a single beam that is focused into a 400-μm optical fiber. As a result, it will be discussed the capability of this assembled system to be applied in real optoacoustic applications, such as OAE.

Chapter 2 will present the conceptual background related with the light propagation in biological tissues and the generation of optoacoustic signals. This includes a study of optical energy propagation in attenuating media, discussing the concepts of optical *absorption* and *scattering*, and the process of optical to acoustic energy conversion. The conditions required for efficient generation of optoacoustic signals, which is based on the thermoelastic expansion caused by the optical *absorption*, will be introduced. In addition, the temporal and spectral characteristics of the acoustic transients produced by optical absorption and their propagation in the media will be described.

In Chapter 3, the optical properties of some nanoparticle structures will be presented for a successive optoacoustic application in Chapter 4: carbon nanotubes, graphene oxide and gold nanorods. It will be remarked how the gold nanorods are the most suitable candidates for optoacustic applications, since they exhibit high absorption peaks in the NIR range, depending on their geometrical characteristics.

In Chapter 4, the nanoparticles presented in Chapter 3 are applied in optical phantoms for optoacoustic measurements performed with the HPDLs-based setup that has been designed. Finally, different mixtures of gold nanorods solutions hosted in quartz cuvette are used to estimate their absolute concentrations from the optoacoustic signals detected at 870 nm, 905 nm and successively at also 972 nm.

Finally, in Chapter 5 it will be discussed the importance to achieve high optical energy levels for optoacoustic applications. In this regard, the last work presented in this dissertation concerns the modeling of a multi-wavelength design (i.e. 808 nm, 880 nm, 910 nm, 940 nm, and 980 nm) based on high-power diode laser sources (i.e. diode laser bars) for beam coupling into optical fibers with small core diameter (i.e. 400 μm). In this regard, it will be remarked that one potential application of diode laser bar sources is OAE that requires a non-invasive inspection of the human body.

1.2. Research project

This research has been financed by OILTEBIA project (Optical Imaging and Laser TEchniques for BIomedical Applications), coordinated by Prof. Horacio Lamela Rivera, which was an Initial Training Network (ITN) funded by the European Community Seventh Framework Programme, Grant Agreement Number 317526.

Chapter 2

Optical propagation in tissues and optoacoustic signal generation

2.1. Introduction

The basic concepts related to the generation of acoustic transients from absorbing media excited by short optical pulses will be examined in this chapter. It will be shown how the properties of the optoacoustic signals are a consequence of the wavelength-dependent optical attenuation of the medium being irradiated. To fully understand the process of optical to acoustic conversion of embedded absorbers, such as biological abnormalities (i.e. cancers or arteriosclerotic plaques) surrounded by healthy tissues, it is essential to comprehend the light interaction with such medium.

The two main physical phenomena affecting the light propagation in media will be presented. The fundamental parameters related with each process will be defined and used to describe the nature of diffuse optical transmission in soft biological media. The objective of this review is necessary to introduce the mechanisms behind the generation of the optoacoustic signals that will be applied in Chapter 4, in which several experiments performed with different kinds of nanoparticles are described.

It will be shown that the optical properties of a medium have a crucial role in the determination of the conditions required for an efficient conversion from optical to acoustic energy. In addition, an analysis of both the temporal and spectral properties of the acoustic transients generated will be presented. It will be shown how the acoustic wave propagation takes place from the point of generation to the surface of the tissue where they are detected.

Finally, this chapter concludes with a description of the most commonly used short pulsed laser sources used in optoacoustic biomedical applications.

2.2. Optical propagation in turbid media

Light attenuation in biological media is mainly caused by their *absorption* and *scattering* properties that are wavelength dependent. In this section, the mechanisms behind the aforementioned phenomena will be discussed. In order to understand the light propagation in biological media, an analysis of the coefficients of *absorption* and *scattering* will be presented, including a description of the diffusion related to the optical propagation in biological tissues, which present multiple *scattering* events.

2.2.1. Optical absorption: light-matter interaction

The *absorption* of electromagnetic radiation is the process in which the energy of a photon is transmitted in the matter. The process of *absorption* produces the transition of an electron, atom, or molecule, to an

excited state (i.e. with higher energy level). For *absorption* to take place, the energy of a photon $E = h\nu$, must be equal to the difference between two energy levels of an atom or molecule (Fig. 2.1).

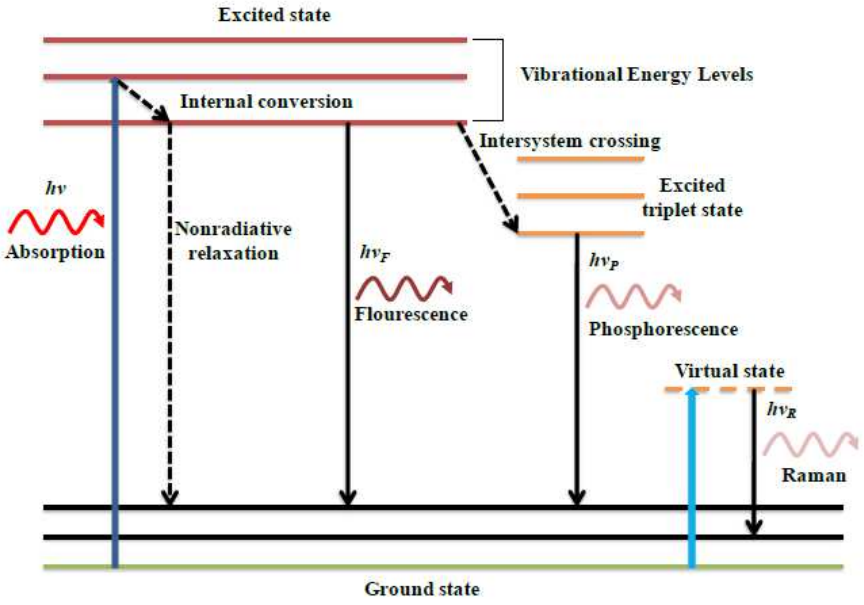

Figure 2.1. Jablonski energy level diagram showing the different kinds of transition from the ground state to the possible excited states caused by photon absorption [79].

When an excited electron relaxes, there are several routes that it can follow to the ground state. The excited electron may relax to the ground state and generate another photon, producing *fluorescence* or *phosphorescence* which depends on the lifetime of the excited electron, or it may convert into heat in a process known as *non-radiative relaxation*. In Figure 2.1, a Jablonski energy level diagram explaining the different transitions between energy states is presented [79]. The energy states can be grouped into two broad categories, *singlet states* and *triplet states*. In singlet states all of the electrons in the molecule have their spins paired, while in triplet states one set of electron spins is unpaired. Triplet states and singlet states differ significantly in their properties as well as in their energies. A triplet state will always have lower energy than its corresponding singlet state. In Figure 2.1 it may be seen that fluorescence is a process composed of three events with different timescales [79]. The excitation of a photon takes place in femtoseconds ($\sim 10^{-15}$ s) that is a relatively short time if compared with other electronic and nuclear processes. The *internal conversion* is a vibrational relaxation to the lowest vibrational energy level in the excited state that takes place in the order of picoseconds ($\sim 10^{-12}$ s) and does not result in the emission of a photon (i.e. nonradiative). *Fluorescence* emission takes in the order of nanoseconds ($\sim 10^{-9}$ s). The phosphorescence process is similar to fluorescence, but the molecule makes a further transition from the lowest excited state to a metastable state by a process known as *intersystem crossing* (see Fig. 2.1) [79]. Since the relaxation from the excited state to the ground state is spin-forbidden, the emission occurs only when the thermal energy raises the electron to a state where the relaxation is allowed. As a result, the *phosphorescence* depends on temperature and has a long lifetime (from 10^{-4} to 10 s).

There are two kinds of photon *scattering* produced by a molecule: elastic and inelastic. In the former, no energy transfer occurs between the photon and the molecule, whereas in the latter that is commonly

referred to as Raman *scattering*, it does. In Raman *scattering*, the molecule is excited to a virtual state before relaxing to the ground state emitting a photon. In this process, the molecule and the photon can interchange part of their energy. If the molecule gains energy, the transition if referred to as Stokes transition and the emitted photon will have a lower frequency as the total energy is conserved. Differently, the transition is referred to as anti-Stokes transition emitting a photon with higher frequency.

2.2.2. Optical absorption process

The absorption process is characterized by the *absorption cross section* σ_{abs} (cm^2) and the *absorption coefficient* μ_{abs} (cm^{-1}), which are wavelength-dependent. The former represents the probability of absorption of a photon. It is defined as the ratio between the power absorbed P_{abs} (W) from an initially uniform plane wave and the irradiance (or intensity) I_0 (W/cm^2), by the following equation:

$$\sigma_{abs} = \frac{P_{abs}}{I_0}. \tag{2.1}$$

Considering a medium with a uniform distribution of identical absorbing particles, the absorption coefficient μ_{abs} (cm^{-1}) is defined as the probability of absorption of a photon per infinitesimal unit of length. It can be considered as the *absorption cross section* per unit of volume:

$$\mu_{abs} = N\sigma_{abs}, \tag{2.2}$$

where N (cm^{-3}) is the density of absorbers in the medium per unit of volume. The absorption coefficient determines how deep a material can be penetrated by light at a specific wavelength before it is absorbed. The mean free path travelled by a photon before being absorbed by the medium is given by:

$$L_a = \frac{1}{\mu_{abs}}, \tag{2.3}$$

where L_a (cm) is defined as the *characteristic linear dimension* (or *absorption mean free path*) of the absorbing material. A description of the propagation of light in a homogenous absorbing medium is presented in Figure 2.2. The fraction of light intensity attenuated by the medium, dI / I_0, is directly proportional to the optical path distance dx where the constant of proportionality is the absorption coefficient μ_{abs} and can be expressed as:

$$\frac{dI}{I_0} = -\mu_{abs} dx. \tag{2.4}$$

Thus, the light intensity absorbed in the interval from x to $x + dx$ is proportional to the absorption coefficient μ_{abs} and the optical path distance dx. The minus sign indicates a decrease in intensity.

Integrating this over the thickness of the medium, d , we get the following equation:

$$\int_{I_0}^{I(d)} \frac{dI}{I} = \int_0^d -\mu_{abs} dx \,, \tag{2.5}$$

which gives the Beer-Lambert law, relating the transmitted light intensity with the input light intensity I_0, the absorption coefficient μ_{abs} and the thickness of the medium d [50]:

$$I(d) = I_0 \exp\left(-\mu_{abs} d\right). \tag{2.6}$$

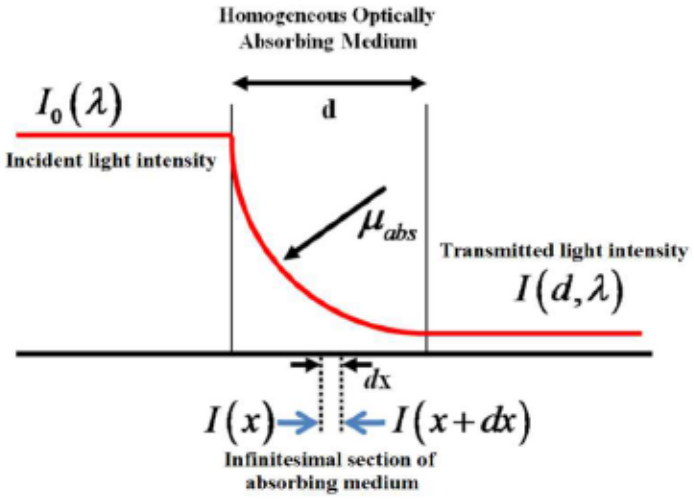

Figure 2.2. Propagation of light in a homogeneous absorbing medium with absorption coefficient μ_{abs} [80].

2.2.3. Optical scattering

Similarly to the absorption, the wavelength-dependent optical scattering is characterized by the *scattering cross section* σ_{sca} (cm^2) and the *scattering coefficient* μ_{sca} (cm^{-1}). The former is defined as the ratio between the power scattered P_{sca} (W) and the irradiance I_0 (W/cm^2), of a uniform plane wave, given as:

$$\sigma_{sca} = \frac{P_{sca}}{I_0} \,. \tag{2.7}$$

For a medium with a uniform distribution of identical scatterers, the scattering coefficient μ_{sca} (cm^{-1}) is defined as:

$$\mu_{sca} = N\sigma_{sca} \,, \tag{2.8}$$

where N (cm^{-3}) is the density of scatterers in the medium per unit of volume. The scattering coefficient determines how deep a material can be penetrated by light at a specific wavelength before it is scattered. The mean free path travelled by a photon before being scattered by the medium is given by $L_s = \mu_{sca}^{-1}$ (cm) that is commonly referred to as the *scattering mean free path* of the scattering material.

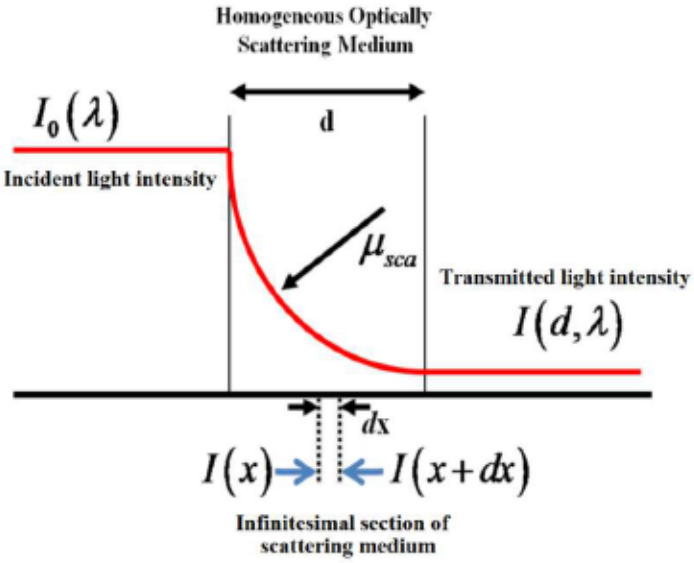

Figure 2.3. Propagation of light in a homogeneous scattering medium with scattering coefficient μ_{sca} [80].

In a homogeneous scattering medium (i.e. $\mu_{sca} >> \mu_{abs}$), light is attenuated following Beer-Lambert law for scattering [56] (Fig. 2.3):

$$I(d) = I_0 \exp(-\mu_{sca} d). \tag{2.9}$$

2.2.4. Light anisotropy

The light scattering in a medium is generally anisotropic, since it is directionally dependent. The angle at which the incident light is scattered in a medium is a function of the size and shape of the scattering particles, as well as the wavelength and the angle of incidence. More generally, each type of particle will have a different scattering profile. This profile is commonly referred to as the phase function $p(\hat{s},\hat{s}')$, which describes the amount of light scattered from the direction of the incident photon trajectory $\hat{s}$ into the direction $\hat{s}'$ (Fig. 2.4). The condition of normalization of the probability distribution requires that the integral of the phase function over all the differential units of the solid angle $d\Omega$ is equal to unity, such that:

$$\int_{4\pi} p(\hat{s},\hat{s}')\, d\Omega = 1, \tag{2.10}$$

where $p(\hat{s},\hat{s}')\, d\Omega$ is the probability that a photon incident from the $\hat{s}$ direction will be deviated in the $\hat{s}'$ direction in the differential unit of the solid angle $d\Omega$. Generally, the phase function will be different from particle to particle because of the anisotropy of the medium. For this reason, an average phase function is required to describe the scattering process. It is assumed that the probability of scattering from one direction into another is only a function of the scattering angle θ between the two directions, so that:

$$p(\hat{s},\hat{s}') = p(\hat{s}\times\hat{s}') = p(\cos(\theta)). \tag{2.11}$$

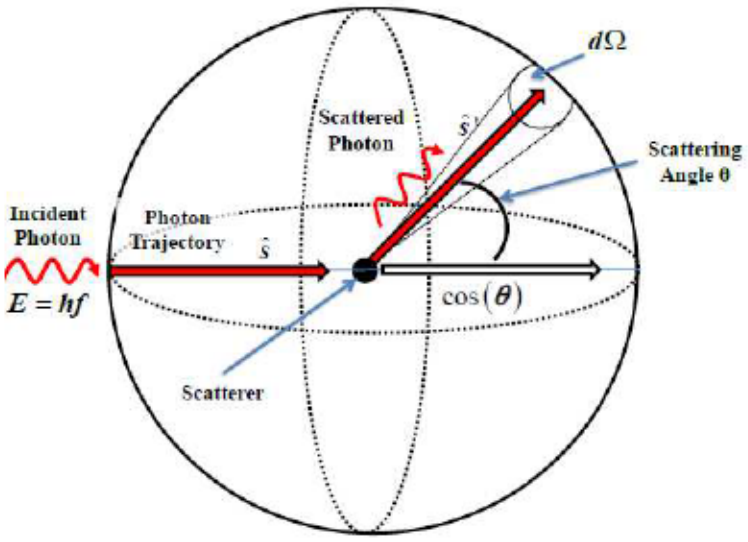

Figure 2.4. Scattering of a photon within a sphere with solid angle $d\Omega$ [80].

A measure of the scattering anisotropy is given by the coefficient of anisotropy g , which is expressed as the average value of the cosine of the scattering angle θ (see Fig. 2.4):

$$g = \langle \cos(\theta) \rangle = \int_{-1}^{1} \cos(\theta) \times p\left(\cos(\theta)\right) d\left(\cos(\theta)\right). \tag{2.12}$$

The anisotropy coefficient g describes three kinds of scattering: extremely forward, isotropic, and backward, when it approaches the value 1, 0, and -1, respectively. Combining the scattering and the anisotropy coefficients, we get the reduced scattering coefficient:

$$\mu_{sca}^{'} = \mu_{sca}(1-g). \tag{2.13}$$

This expression relates the number of anisotropic scattering events given by $m = 1/(1-g)$, equivalent to an isotropic event. For instance, if the anisotropy coefficient is $g = 0.9$, i.e. a typical value in biological media, an average of $m = 10$ scattering events will be necessary to scatter a population of photons isotropically. The definition of the reduced scattering coefficient allows an expression for the transport attenuation $\mu_t^{'}(\text{cm}^{-1})$, to be defined as:

$$\mu_t^{'} = \mu_{abs} + \mu_{sca}^{'}, \tag{2.14}$$

where the reciprocal of this is the mean free transport path, $L_t = \mu_t^{'-1}$ (cm).

In biological tissues the *scattering* predominates and the collimated light gets diffuse. When light is diffuse in turbid media, the optical penetration depth is better characterized by the effective attenuation coefficient μ_{eff} , which is derived by the diffusion theory and is defined as [81]:

$$\mu_{eff} = \sqrt{3\mu_{abs}\mu_t^{'}} = \sqrt{3\mu_{abs}\left(\mu_{abs} + \mu_{sca}^{'}\right)}. \tag{2.15}$$

In this case, the light penetration depth in tissues is defined as $L_{eff} = \mu_{eff}^{-1}$ (cm), and light attenuation is described by $I(d,\lambda) = I_0 \exp\left(-\mu_{eff}(\lambda) d\right)$, showing and exponential decay with increasing depth into the medium.

2.3. Diagnostic window

A summary of the different optically attenuating media commonly found in biological tissues are presented in Figure 2.5 over the wavelength range from 200 nm to 1200 nm. The range of wavelengths between 650 nm and 1350 nm is referred to as the *therapeutic window* or *diagnostic window* for optical-based technologies and it is where the light exhibits the maximum penetration into the biological tissues. This range contains the typical spectroscopic profiles of the most common endogenous chromophores, which are essential for several diagnostic purposes. Within this wavelength range, *scattering* is dominant over *absorption*, so that the light propagation becomes diffuse. The major absorbing components in soft tissues are water, lipids, oxygenated and deoxygenated hemoglobin.

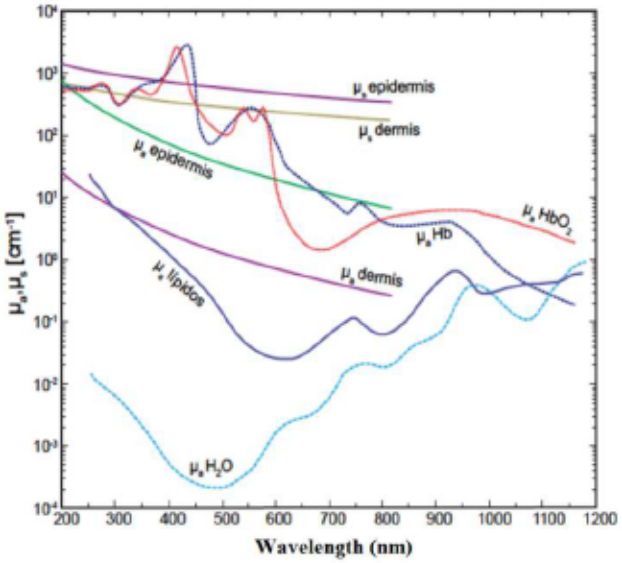

Figure 2.5. Absorption μ_{abs} and scattering μ_{sca} coefficients of various biological components of soft tissues [82].

Angiogenesis is the peculiarity of any kind of malign tumor when it gets a determined growth stage. For that reason, the blood is the interested tissue for the detection of breast tumors. The oxygenated and deoxygenated hemoglobin are their main chromophores. Blood has a higher optical absorption than the other biological components in visible and NIR range. Special interest for optoacoustic applications has a region beyond 650 nm, where the other breast tissues have a lower effective attenuation coefficient. From the spectroscopic analysis of the blood it is possible to calculate the concentration of both oxygenated and deoxygenated hemoglobin, providing information on the oxygen saturation in the blood (SO_2) that is the quotient between the concentration of oxygenated hemoglobin and the total concentration of hemoglobin. In the following subsections a brief description of each of the abovementioned chromophores will be presented.

2.3.1. Water

Although water is nearly transparent in the range of visible light, it becomes absorbing over the NIR region. Water is considered as one of the most critical chromophores, since its concentration is high in most biological tissues. The relation between the absorption coefficient (cm^{-1}) of water and the wavelength is presented in Figure 2.6. It can be observed that the attenuation due to water absorption is low within the wavelength range from 600 nm to 900 nm. After 900 nm, the absorption increases abruptly with the wavelength and exhibits a peak at ~ 970 nm. The value of the absorption coefficient μ_{abs} of water at 700 nm is 10^{-2} cm^{-1} and at 475 nm is 10^{-4} cm^{-1} [4]. For longer wavelengths, the absorption coefficient increases significantly, i.e. at 15 μm it becomes 3 x 10^{3} cm^{-1} [4].

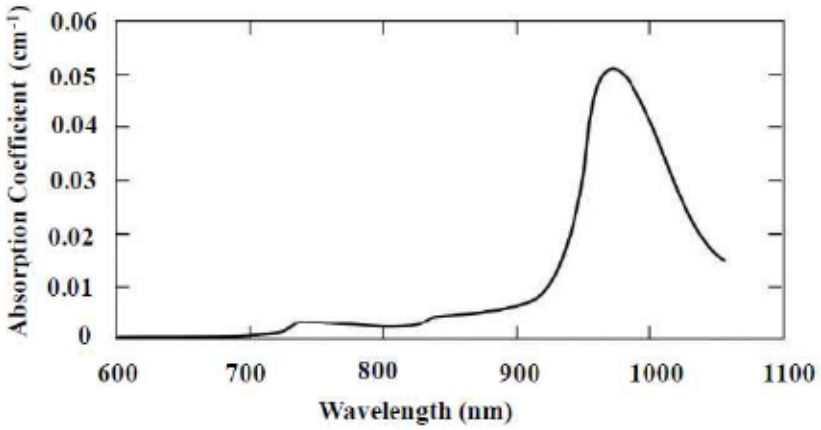

Figure 2.6. Absorption spectrum of pure water from 600 nm to 1050 nm [83].

2.3.2. Lipids

The lipids are one of the major components that can comprise 10-40% of human body. Most of the lipid content in the body exists in the form of triglycerides (neutral fats) and is found in the subcutaneous tissues and around internal organs. The absorption spectrum of lipids is similar to that of water, but is distinguished from it by the sharp absorption band close to 930 nm and the absence of the peak at 970 nm.

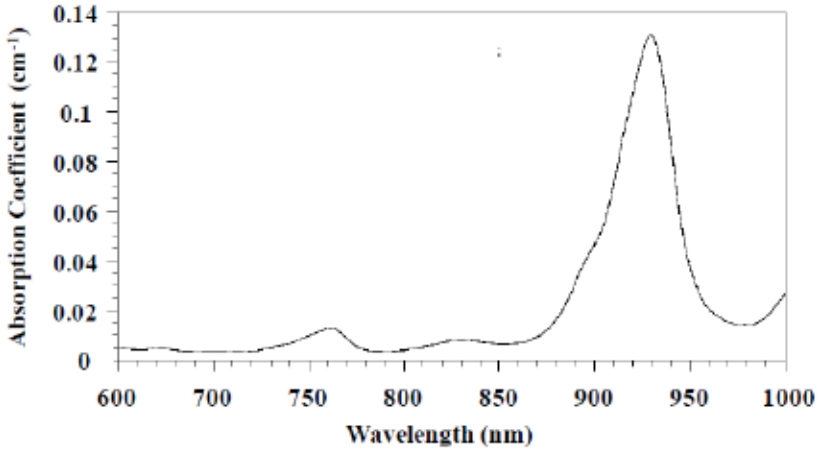

Figure 2.7. Absorption spectrum of pig fat from 600 nm to 1000 nm [84].

In Figure 2.7, the absorption spectrum of pig fat, basically identical to that of human lipids, is presented between 600 nm and 1000 nm [84].

2.3.3. Blood (Hemoglobin)

Blood is an important chromophore within the diagnostic window that is commonly used for the detection and diagnosis of tumor growth. Blood consists of two different types of hemoglobin: oxygenated hemoglobin (HbO2) and deoxygenated hemoglobin (Hb). These two different types of hemoglobin exhibit different absorption spectra, as shown in Figure 2.8.

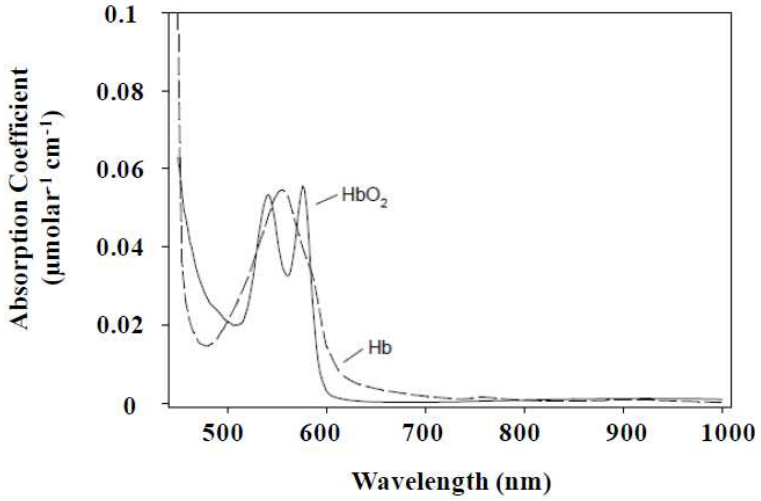

Figure 2.8. Absorption spectrum of oxygenated and deoxygenated blood [80].

Blood is a strong absorber for wavelengths up to 600 nm, beyond which the absorption of oxygenated hemoglobin is observed to drop off abruptly, while the absorption of deoxygenated hemoglobin drops more steadily. The points where the oxygenated and deoxygenated hemoglobin intersect are referred to as the *isobestic points*. From a optoacoustic spectroscopy analysis of blood it is possible to calculate the concentration of both the oxygenated hemoglobin and the deoxygenated hemoglobin, providing information of the oxygen saturation (SO2), which is the ratio of the oxygenated hemoglobin concentration to the total hemoglobin concentration.

2.3.4. Melanin

Other tissue component with less significant contribution to the total absorption spectrum of tissues is melanin. Melanin is a chromophore that exists in the human epidermal layer of skin and is responsible for protection from harmful UV radiation. Melanin is one of the major absorbers of light in some biological tissues (although its contribution is smaller than other components).

2.4. Process of optical to acoustic energy conversion

In Figure 2.9 it is shown a graphical description of the conversion from an optical pulse to acoustic energy in a light absorbing medium. This process involves two different steps: first the optical energy

from a short optical pulse is absorbed by an object, which may be any of the chromophores discussed in the previous section, and then is transformed into thermal energy; second, an ultrasonic pressure wave is induced from the thermal energy generated, due to the fast thermoelastic expansion of the absorber embedded in the tissue. In this section, the processes and key parameters required in each of the two steps for efficient optical to acoustic energy conversion will be described in detail.

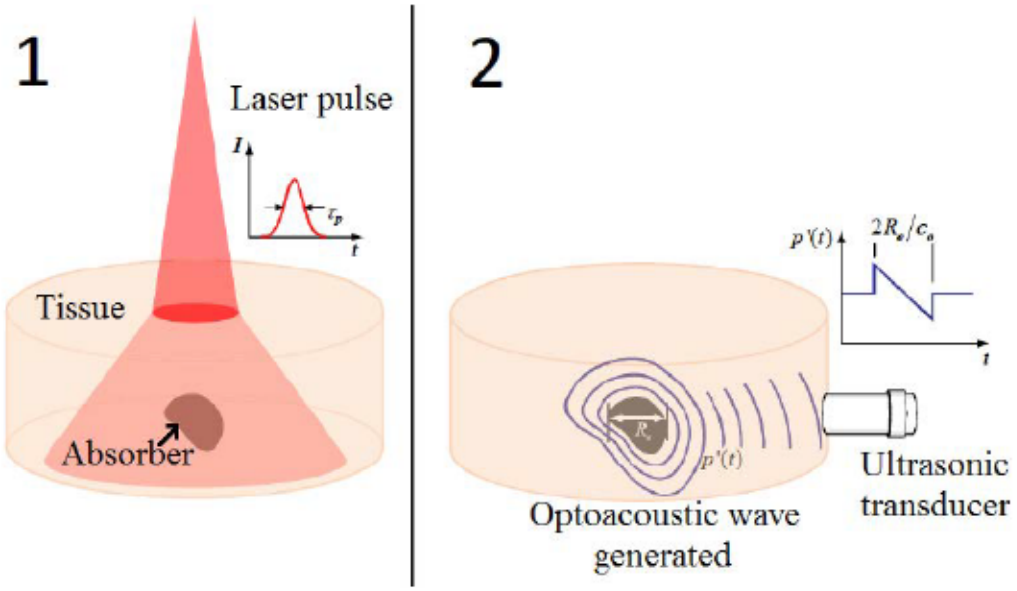

Figure 2.9. General scheme of the generation of optoacoustic signals caused by the thermoelastic expansion of an absorber embedded in a tissue [85].

2.4.1. Optical to thermal energy conversion

From Beer-Lambert law it has been seen that the light power P_T transmitted by an absorber is related to the initial light power P_0, the absorption coefficient μ_{abs}, and the optical path distance d travelled in the medium, as [50]:

$$P_T = P_0 \exp(-\mu_{abs} d), \tag{2.16}$$

thus the absorbed light power P_{abs} can be described by:

$$P_{abs} = P_0 - P_T. \tag{2.17}$$

The laser pulse energy absorbed by the medium, $E_{abs} = P_{abs}\tau_p$, where τ_p is the optical pulse duration, determines the amount of thermal energy E_{th} induced in the absorbing material. The amount of the incident laser energy is directly proportional to the thermal energy induced into the absorber. From Eq. (2.16) and (2.17) it can be inferred that the thermal energy induced is directly related to the absorption of the material. In case of strong absorption, i.e. $\mu_{abs} r_{spot} >> 1$, where r_{spot} is the radius of the incident laser

spot, the acoustic pressure waves will have higher amplitude [86]. The thermal energy generated E_{th} can be expressed in terms of μ_{abs} and the absorption depth L_a, as:

$$E_{th} \approx E_{abs}\mu_{abs}L_a . \tag{2.18}$$

The thermal energy deposited in the medium is wavelength-dependent by means of the absorption coefficient. Consequently, the thermal energy deposited in the medium per volume unit, $E_{th}(\lambda)$ (J/cm^3) can be expressed as [15, 50, and 79]:

$$E_{th}(\lambda) = \mu_{abs}(\lambda)\frac{E_{abs}}{A} = \mu_{abs}(\lambda)F , \tag{2.19}$$

where F (J/cm^2) is the optical energy density, or fluence, deposited by the laser per area unit A (cm^2). On the surface of the absorber we have $F_0 = E_0 / A$, where the incident optical energy is $E_0 = I_0\tau_p$. Therefore, the optical fluence at a distance d (cm) within the medium, using Beer-Lambert law, is [87]:

$$F(\lambda, d) = F_0 \exp(-\mu_{eff}(\lambda)d) . \tag{2.20}$$

The conversion from the optical energy to the thermal energy creates a temperature increase ΔT in the embedded absorber, which can be evaluated using the following expression [88]:

$$\Delta T(\lambda) = \frac{\mu_{abs}(\lambda)F}{\rho C_V} = \frac{E_{th}(\lambda)}{\rho C_V} , \tag{2.21}$$

where the temperature increase ΔT (ºC) is dependent on the wavelength of the laser source and is given in function of the density of the medium ρ (g/cm^3), the heat capacity at constant volume C_V (J/g ºC) and is directly proportional to the thermal energy deposited by the laser source per volume unit.
To efficiently generate optoacoustic signals, the condition of *Thermal Confinement* must be satisfied. The heat generated from the absorbed optical energy is propagated to the neighboring absorbing region for thermal conduction. The time scale for heat dissipation of the absorbed energy by thermal conduction is related to the linear volume of the tissue being heated by the optical source. The *thermal relaxation time* τ_{th} of the heated volume can be approximated by [11]:

$$\tau_{th} \approx \frac{\rho C_p L^2}{4k} = \frac{L^2}{4\alpha_T} , \tag{2.22}$$

where L (cm) is the penetration depth, k (W/ºC· cm) the thermal conductivity, ρ (g/cm^3) the density of the material, and C_p (J/g ºC) the specific heat capacity of the absorber at constant pressure. The thermal diffusivity of the medium is $\alpha_T = k / \rho C_p$ (m^2/s). Evaluating Eq. (2.22) it can be seen how fast the heated volume returns to the equilibrium adjusting to the temperature of its surroundings.

A typical value for the thermal diffusivity in most biological tissues is $\alpha_T \approx 1.4\times10^{-3}$ (cm^2/s) [11]. For a medium in which the absorption dominates over the scattering, i.e. $\mu_{abs} >> \mu_{sca}$, the penetration depth is given by $L = L_a = \mu_{abs}^{-1}$, defined in Eq. (2.3). In order to fulfill the condition of thermal confinement, the optical pulse duration τ_p should be shorter than the thermal relaxation time, i.e. $\tau_p < \tau_{th}$, of the heated volume, so that there is no heat loss by thermal diffusion during the heating process (Fig. 2.9).

Considering a highly absorbing biological tissue where $\mu_{abs} = 200$ cm^{-1}, from Eq. (2.3) we get $L_a = 50$ μm. In addition, using Eq. (2.22) we find that the laser pulse width τ_p, required for the thermal confinement of the optoacoustic signal generation, must be $\tau_p < \tau_{th} = 4.5$ ms, which is easily satisfied. If the absorption coefficient is lower, the thermal relaxation times are higher.

2.4.2. Thermal to acoustic energy conversion: optoacoustic signal generation

All materials change in size when go through to a temperature change ΔT. The thermal energy deposited in the medium through optical absorption produces an increase of pressure ΔP (Pa) that is determined by the relative change in volume $\Delta V / V$, the coefficient of thermal expansion β (°C^{-1}), and the thermodynamic coefficient of isothermal compressibility of the medium γ (Pa^{-1}) and is given by [10, 89]:

$$\Delta P(\lambda) = -\frac{1}{\gamma}\frac{\Delta V}{V} + \frac{1}{\gamma}\beta\Delta T(\lambda), \tag{2.23}$$

where the coefficient of isothermal compressibility of the medium:

$$\gamma = \frac{1}{\rho v_{med}^2}\frac{C_p}{C_V}, \tag{2.24}$$

where ρ (g/cm^3) is the density, v_{med} (m/s) is the speed of sound in the medium and C_p (J/g·°C) and C_V (J/g·°C) are the specific heat capacities at constant pressure and volume, respectively. When a short laser pulse illuminates the absorbing tissue and there is no appreciable dilatation of the medium, we can approximate $\Delta V / V \approx 0$ and Eq. (2.23) it is reduced as:

$$\Delta P(\lambda) \approx \frac{1}{\gamma}\beta\Delta T(\lambda). \tag{2.25}$$

The change in volume is negligible only when the condition of *Stress Confinement* is satisfied. This condition requires that the time for deposition of thermal energy in the absorbing medium must be shorter than the time taken by the medium to change in volume for thermal expansion. To satisfy this condition, the pulse width of the optical radiation must be shorter than the time taken by the thermoelastic wave to propagate a distance equal to the optical penetration depth. This time is referred to as *stress relaxation*

time τ_{stress}. The condition of stress confinement can be expressed in terms of the characteristic linear dimension L_a of the tissue volume being heated and the speed of sound in the medium v_{med} by the following equation [88]:

$$\tau_p < \tau_{stress} = \frac{L}{v_{med}}. \tag{2.26}$$

This condition establishes the resolution limit of an optoacoustic imaging (OAI) system in function of the pulse width of the laser source applied. Considering for instance $L_a = 50$ μm and a speed of sound in biological tissue of 1.5 mm/μs, then the laser pulse width must be $\tau_p < \tau_{stress} = 33.3$ ns. If this condition is not satisfied, the temporal profile of the pressure generated will be expanded by the temporal profile of the laser pulse. From Eq. (2.25) it can be noticed that the pressure induced is directly proportional to the temperature increase. It should be underlined that the pressure generated from the optical interaction with the medium is dependent on the wavelength of the optical source. Replacing Eq. (2.21) into Eq. (2.25) we get the expression of the pressure increase in function of the thermal energy generated:

$$\Delta P(\lambda) = \frac{1}{\gamma}\frac{\beta}{\rho C_V} E_{th}(\lambda). \tag{2.27}$$

In Eq. (2.27) we can identify a term of optoacoustic efficiency, which is commonly defined as *Grüneisen Parameter*. The value of this parameter depends on the specific tissue and indicates the portion of the laser energy that is available for conversion into acoustic energy. It is defined as [10, 79]:

$$\Gamma = \frac{1}{\gamma}\frac{\beta}{\rho C_V} = \frac{\beta v_{med}^2}{C_p}. \tag{2.28}$$

The Grüneisen parameter is a dimensionless factor dependent on the temperature. For water and aqueous solutions at environmental temperature (T = 20 ºC), the Grüneisen parameter equals 0.1 [90, 91]. For instance, muscular tissues typically contain ~ 75 % of water, the coefficient of thermal expansion is $\beta \approx 3.8\times10^{-4}$ (ºC^{-1}), the heat capacity at constant pressure is $C_p = 3.7$ (J/g·ºC), and the speed of sound is $v_{med} = 1.5$ mm/μs. Therefore, from Eq. (2.28) the Grüneisen parameter is calculated as ~ 0.23 in the muscle [92]. Replacing Eq. (2.28) into Eq. (2.27), we get:

$$\Delta P(\lambda) = \Gamma E_{th}(\lambda) = \Gamma \mu_{abs}(\lambda) F_0. \tag{2.29}$$

From Eq. (2.29) it can be observed that the initial pressure of the optoacoustic signal generated is directly proportional to the optical energy absorbed, which depends on the wavelength. Eq. (2.29) covers an important role in optoacoustic spectroscopy (OAS), where the spectroscopic profile of a tissue can be obtained from the pressure related to the optoacoustic signals generated in a certain range of different wavelengths. Figure 2.10 shows the amplitude of the pressure wave generated at a distance *d* from the interface of a medium (i.e. a biological tissue) when both *absorption* and *scattering* are present.

This process can be described by the following equation [90]:

$$p(d,\lambda) = \Gamma \mu_{abs}(\lambda) F_0 \exp(-\mu_{eff}(\lambda) d), \tag{2.30}$$

where p is the initial pressure, dependent on the wavelength, at a distance d from the surface of an absorbing medium.

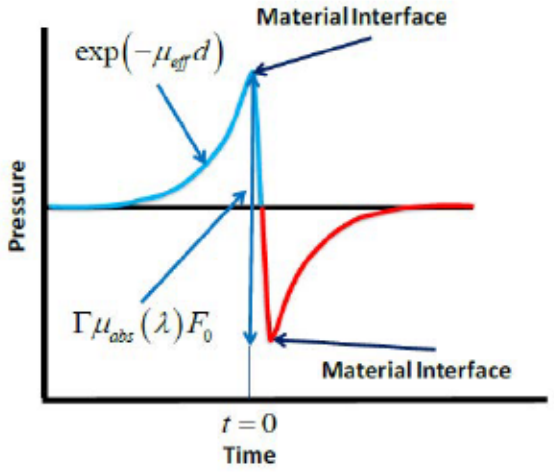

Figure 2.10. Pressure transient generated at the interface of a turbid absorbing medium [80].

2.4.3. Temporal and spectral profile of an optoacoustic signal

Previously, it has been shown that the pressure transients generated optoacoustically from the optical absorption and thermoelastic expansion contain information about the optical properties of the medium that is exposed to the laser light. The temporal profile of the pressure wave transmitted by an absorber with a complex geometry, such as a tumor growth, can be represented by the convolution of acoustic waves emitted by a number of small spherical sources. Considering a sphere of radius r where the condition $\mu_{abs} >> \mu_{sca}$ is satisfied with the following conditions:

1. Uniform absorption of the optical energy, i.e. $\mu_{abs} << 1/r$;
2. Thermal confinement: $\tau_p < \tau_{th}$;
3. Stress confinement: $\tau_p < \tau_{stress}$;
4. The acoustic properties of the spherical absorber are identical to the surrounding medium,

then the acoustic pressure generated by the thermoelastic expansion of the absorber will propagate isotropically and can be expressed as [10]:

$$p'\left(\tau = t - \frac{R}{v_{med}}\right) = \frac{1}{2R}\Gamma \frac{\mu_{abs} F_0}{V_{sph}} (-v_{med}\tau) H(r - |v_m \tau|), \tag{2.31}$$

where H is Heaviside function (or step), the volume of the sphere is $V_{sph} = 4\pi r^3/3$, R is the distance from the point of observation to the center of the spherical absorber, v_{med} is the speed of sound in the medium and F_0 is the laser fluence incident on the sphere.

The optoacoustic wave produced presents the typical *N-shape* profile with triangle phase compression followed by an expansion (see Fig. 2.11) [10]. The duration of the optoacoustic signal is defined by the speed of sound along the diameter of the sphere, given as:

$$2r = (t_2 - t_1)v_{med}. \tag{2.32}$$

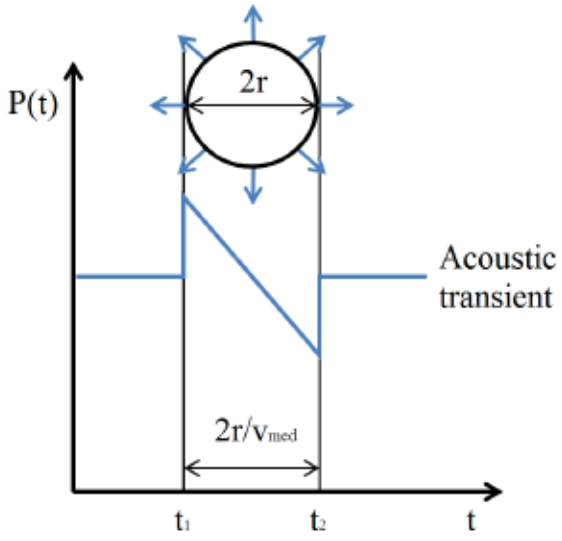

Figure 2.11. Temporal waveform of the optoacoustic signal generated by a sphere or radius *r*, where the speed of sound in the medium is v_{med} [reprinted from 80].

The spectral response of the optoacoustic transients can be calculated by the Fourier Transform of the temporal signal (Eq. (2.31)), given as [93]:

$$P(\omega) = \int_{-\infty}^{\infty} p'(\tau)e^{-i\omega\tau}d\tau \propto \frac{(\omega r/v_{med})\cos(\omega r/v_{med}) - \sin(\omega r/v_{med})}{(\omega r/v_{med})^2}, \tag{2.33}$$

where ω is the frequency of the ultrasonic signal. The amplitude of the spectrum is represented in Figure 2.12. From the optoacoustic spectrum given by Eq. (2.33) we can obtain both the central frequency and the bandwidth of the optoacoustic emission from a sphere. The parameters $f_{\max}$ and Δf_{-3dB}, indicated in Fig. 2.12, are fundamental for the design of any ultrasonic sensor for the detection of optoacoustic waves:

$$f_{\max} = 0.33\frac{v_{med}}{r}, \tag{2.34}$$

$$\Delta f_{-3dB} = f_{upper} - f_{lower} = 0.51\frac{v_{med}}{r} - 0.16\frac{v_{med}}{r} = 0.35\frac{v_{med}}{r}, \tag{2.35}$$

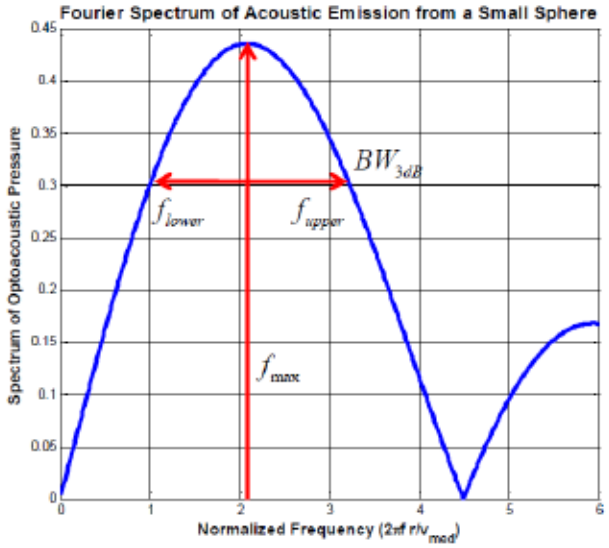

Figure 2.12. Spectral amplitude of the optoacoustic pressure from a small sphere as a function of the normalized frequency [80].

However, it should be considered that the central frequency and the acoustic signal bandwidth defined in Eqs. (2.34) and (2.35) for an absorbing sphere correspond to the low frequency part of the optoacoustic signal (i.e. the first lobe of the spectrum) that decreases linearly (see *N-shape* in Fig. 2.11).
In order to detect the fast rise and fall transitions of the optoacoustic signal at the boundaries of the sphere, a higher bandwidth is necessary. However, by increasing the bandwidth, the thermal noise in the detection process is also amplified; hence a compromise between both is necessary [93]. This can be done by considering a rise time of the acoustic signal to be 0.3 times the total transition time, in this case $0.3\times(2r/\upsilon_{med})$, which in terms of frequency (that corresponds to the bandwidth) is equivalent to:

$$f_{upper}=1.5\frac{v_{med}}{r}. \tag{2.36}$$

In soft tissues, the absorption distribution is complex due to the existence of spherical particles of many different dimensions. If a characteristic size of the absorber is defined, we can estimate the necessary bandwidth to detect it by using Eq. (2.36). For instance, considering two spherical tumors embedded in a soft tissue with radius of 1 mm and 5 mm, respectively, and taking into account that the acoustic speed in the tumor is 1.5 mm/μs, then the bandwidths f_{upper} of the optoacoustic signals generated from each sphere are 2.25 MHz and 450 kHz, respectively.

2.5. Propagation of an optoacoustic wave

In this section it is described how the acoustic wave propagates in the elastic medium and how we can retrieve the information about the initial pressure distribution. In Eq. (2.31) it has been seen that if the conditions of thermal and stress confinement are satisfied, the initial pressure distribution is proportional to the absorption coefficient and to the optical fluence. We consider that $p_0(\vec{r}')$ is the initial pressure distribution generated by a laser pulse with temporal profile $L(t)$ in an optically heterogeneous tissue

with properties of *absorption* and *scattering* (Fig. 2.13). Assuming that the laser excitation is a Dirac delta function, i.e. $L(t)=\delta(t)$, the pressure $p_\delta(\vec{r},t)$ in the position $\vec{r}$ and time t can be expressed as [94]:

$$p_\delta(\vec{r},t)=\frac{1}{4\pi v_{med}^2}\frac{\partial}{\partial t}\left[\frac{1}{v_{med}t}\iiint p_0(\vec{r}\,')\delta\left(t-\frac{|\vec{r}\,'-\vec{r}|}{v_{med}}\right)d\vec{r}\,'\right], \tag{2.37}$$

where v_{med} is the speed of sound in the tissue. Eq. (2.37) calculates the acoustic pressure in the position $\vec{r}_0$ and time $t=|\vec{r}\,'-\vec{r}|/v_{med}$ integrating the initial pressure distribution over a sphere with radius $|\vec{r}\,'-\vec{r}|$. If we consider a finite pulse duration, the pressure distribution will be equal to the convolution of impulse pressure $p_\delta(\vec{r},t)$ and the temporal profile of the laser $L(t)$:

$$p(\vec{r},t)=\int_{-\infty}^{+\infty}L(t-\tau)p_\delta(\vec{r},\tau)d\tau\,. \tag{2.38}$$

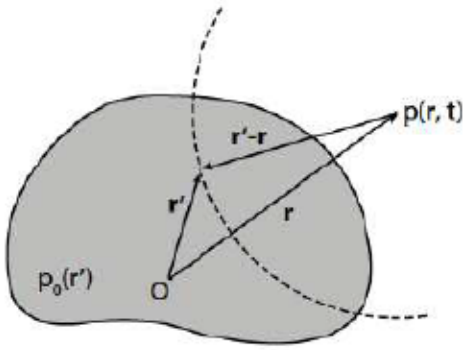

Figure 2.13. Diagram of optoacoustic wave propagation [85].

The optoacoustic pressure in the position $\vec{r}$ and time t can be calculated integrating the initial pressure distribution $p_0(\vec{r}\,')$ over a spherical surface with radius $|\vec{r}\,'-\vec{r}|=v_{med}t$. The objective of optoacoustic tomography is to invert Eq. (2.37) from the measurement of $p_\delta(\vec{r},t)$ to retrieve the initial pressure distribution $p_0(\vec{r}\,')$. For this, it is necessary to resort to computational image reconstruction algorithms.

2.6. Short pulsed laser sources for efficient optoacoustic signal generation

The most efficient laser sources which produce optoacoustic signal generation are based on the emission of short pulses. Such sources have many advantages over modulated continuous sources. The major advantage is based on the high energy stored in each pulse, which produces high acoustic signals improving the signal to noise ratio. Pulsed laser sources deposit large amounts of energy in a short slot of time. It has already been demonstrated that the pulse width of the laser source should be shorter than the thermal relaxation time of the heated volume, i.e. $\tau_p<\tau_{th}$, to avoid that the thermal energy generated is dispersed inside the biological medium (thermal confinement condition). In addition, the time for deposition of thermal energy in the absorbing medium must be shorter than the time taken by the medium to change in volume for thermal expansion, i.e. $\tau_p<\tau_{stress}$ (i.e. stress confinement condition).

The main laser sources used for optoacoustic signal generation within the therapeutic window in biomedical applications are:

1. Q-Switched Nd:YAG,

2. Pulsed high-power diode lasers (HPDLs),

3. Q-Switched Nd:YAG-laser pumped Optical Parametric Oscillator (OPO).

Typically, solid state lasers are used for the generation of ultrasounds but their use in clinical environment is inconvenient due to their large sizes, high costs, and low repetition rates (a few Hz). Currently, there is a lot of interest in HPDLs as sources for optoacoustic signal generation in biomedical applications [57-59, 61, 62, 64-66, 68]. This is due to their numerous advantages over traditional pulsed laser systems, such as: small sizes, low costs, and high repetition rates (up a few kHz). However, the main drawbacks of such optical sources rise from their low peak power emitted in comparison with solid state lasers, but they can be combined side-by-side to deliver a higher contribution of optical power.
The Nd:YAG laser (more precisely Nd3+:YAG, which is an acronym for neodymium–doped yttrium aluminum garnet) is the preferred choice of laser source for OAI applications, since it efficiently satisfies both the thermal and stress confinement conditions discussed previously.
Another commonly used short pulsed optical source is the multi-wavelength Nd:YAG-laser pumped OPO. This device operates similarly to a laser cavity, but is based on the gain from parametric amplification in a nonlinear crystal rather than from stimulated emission. This device produces a wide range of wavelength-controllable optical pulses within the therapeutic window.

2.7. Conclusions

In this chapter, the key concepts related to the optical propagation in tissues and to the optoacoustic signal generation have been presented. It has been shown that the attenuation of light is principally governed by the wavelength-dependent optical absorption and scattering coefficients of the medium μ_{abs} and μ_{sca}, respectively, from which the exponential decay of the transmitted optical intensity is directly related, in according to Beer-Lambert law.

A review of the anisotropic nature of electromagnetic radiation scattering in biological tissues has been provided. From a spectroscopic review of the main biological chromophores used for diagnostic purposes, the optimum wavelength range of the optical source for biomedical applications has been identified between 200 nm and 1200 nm.

The main parameters associated with efficient optical to thermal and thermal to acoustic energy conversion processes have been obtained by means of a step-by-step analysis of the behavior of optical energy in attenuating media. It has been shown how the acoustic pressure transients are generated by the thermoelastic expansion of a medium, which in turn is caused by the thermal and stress confinement of the short pulsed optical energy absorbed by the medium. From this analysis it has been seen that the pressure wave generated at a distance d from the interface of a medium is directly related to the wavelength-dependent absorption coefficient and to the incident fluence on the surface of the medium,

and undergoes an exponential decay inside it. Based on this theory, optoacoustic measurement schemes are implemented to quantify the optical properties and the optoacoustic responses of some nanoparticles solutions as absorbers of different nature.

A brief review on the temporal profile and the spectral response of an optoacoustic signal has been discussed taking into account the optoacoustic emission from a sphere of radius *r*. Finally, it has been discussed how we can retrieve the information about the initial pressure distribution, which is the base of the image reconstruction algorithms. Nevertheless, they are not applied in this dissertation.

In the next chapter, a study of some kinds of nanoparticles as absorbing media for optoacoustic applications will be undertaken.

The general concepts of optoacoustics presented in this chapter will be applied to the nanoparticles solutions described in Chapter 3. In this regard, Chapter 4 will show the optoacoustic signal generation from different kinds of nanoparticles with high optical absorption in the NIR range.

Chapter 3

Optical properties of some kinds of nanoparticles for optoacoustic applications

3.1. Introduction

The detection of cancer at early stages is necessarily important for preventing the growth of the cancer cell population within the corporeal organs in successive stages. Among all cancers, some of them are more statistically diffused and harmful. Breast cancer is one of the most diffused and differentiated kind of cancer in the world existing in a wide variety of forms [95]. The increasing demand for new techniques to enhance spectroscopic characterization and optical contrast in-vivo of unhealthy tissue is at the forefront of new innovations in nanomedicine. In this regard, specific kinds of nanostructures are often required to target the tumoral cells in their early stages of growth. The nanometric sizes of nanoparticles give them advantageous characteristics in a wide variety of medical research, including *in vivo* imaging and therapy.

Recent advances in synthesis and functionalization of nanoparticles have brought a significant intensification in their applications as highly specific and effective optical contrast agents in various optical imaging techniques, such as optical coherence tomography, fluorescence imaging, optical reflectance microscopy and recently, OAI. The specific biomedical applications include imaging of cell and tissues, drug delivery, and sensing of target molecules. OAI is one of the biomedical fields that have increasingly developed experiments with nanoparticles in the last two decades [96-98]. Because of their high photo-stability, narrow ranges of emission, and broad excitation wavelengths, the nanoparticles have attracted much attention from numerous groups of scientists. Popular nanoparticles in biomolecular and biomedical imaging include fluorescent particles for optical imaging, such as quantum dots, gold nanoparticles and magnetic particles. In addition, recent advances in the area of plasmonic nanotechnology opened new opportunities for the development of nanoparticle-based contrast agents with high absorption properties in the NIR spectral range for OAI applications [99].

In this chapter, the optical properties of different kinds of nanoparticles will be presented for their applications in biomedical imaging and therapeutics. Specifically, the optical properties of carbon nanotubes (CNTs), graphene oxide nanoparticles (monolayer graphene oxide (GO), reduced graphene oxide (rGO), reduced graphene oxide-gold nanoparticle hybrid (rGO@Au)), and gold nanorods are presented.

3.2. Carbon nanotubes

The discovery of carbon allotropes, including graphene oxide nanoparticles and CNTs, has revolutionized the biomedical research for their remarkable structural, mechanical and electronic properties, such as small sizes, high strength, and high electrical and thermal conductivity [100, 101]. In addition, they have

shown unique features that are suitable as optical contrast agents, such as strong NIR absorbance, large surface-to-volume ratio, rigid structure, good thermal conductivity, and the potential for high biocompatibility. The CNTs are hexagonal networks of carbon atoms with diameter of ~1 mm and length of ~1-100 μm, consisting of a layer of graphite rolled up into a cylinder [102].

There are two kinds of CNTs: single-walled nanotubes (SWNTs) and multi-walled nanotubes (MWNTs), which differ in the arrangement of their graphene cylinders. SWNTs have only a single rolled layer of graphene cylinders; while MWNTs have many rolled layers (approximately 50), as shown in Figure 3.1 [103]. In the experiments presented in the next chapter (section 4.2.1), double-walled carbon nanotubes (DWCNTs) that are composed of only two layers of graphene cylinders will be used. Normally, the optical absorption of the CNTs increases with the number of layers.

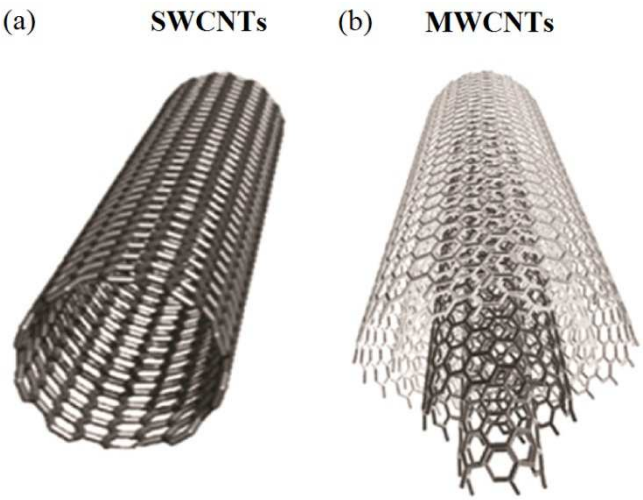

Figure 3.1. Schematic representations showing the structures of CNTs: a) SWCNTs and b) MWCNTs [104].

The rolling can be done at different angles and curvatures, which result in different properties. The diameter typically varies in the range 0.4–40 nm, but the length can reach several centimeters [105]. The aspect ratio of the CNTs (i.e. the length-to-diameter ratio) can reach more than one hundred millions [106], which is incomparable by any other material. Consequently, all the properties of the CNTs (i.e. mechanical, electronic and optical) are extremely anisotropic and tunable. A CNT can be exhibit a certain angle with respect to a plane perpendicular to the long axis in a range between 0 and 30°.

This tunability of the properties of CNTs is potentially useful in optics and photonics, in particular for the production of light-emitting diodes (LEDs) and photo-detectors based on a single CNT. Their unique feature is the narrow selectivity in the wavelength of emission and detection of light.

In recent years, carbon-based nanocomposites have been developed as OAI contrast agents, due to their advantages of nontoxicity, photostability, strong optical absorbance in the NIR spectrum, and easy surface modification [107]. Among the carbon nanomaterials, CNTs are considered one the most promising contrast agents for enhanced OAI because of their intrinsic optical absorbance in the NIR spectrum.

Particularly, DWCNTs are intriguing materials that exhibit intermediate properties between those of SWNTs and MWNTs for use as imaging and therapeutic agents in biological systems.

Recently, CNTs have been intensively studied as contrast agents in OAI systems due to their excellent characteristics. For example, the wide-optical absorption spectrum of CNTs in visible and NIR spectra is very useful for providing an efficient exogenous contrast of detected tumors from healthy tissues in the NIR region. Although CNTs can provide strong optical contrast when employed for biomedical

applications, their absorption coefficient in the NIR is relatively lower than gold-based nanoparticles, because the latter can be selectively tuned in the spectrum by changing their sizes.
However, due to the large surface area, the NIR optical absorption of CNTs can be improved significantly by conjugating the particles with small molecule dyes or coating with a gold layer. The enhancement of optoacoustic contrast by coating CNTs with a golden layer has been reported and demonstrated that CNT-gold hybrids offered a promising alternative for noninvasive detection of cancer [108, 109]. Besides, CNTs can be easily employed for photothermal therapy due to their strong optical absorption and extraordinary thermal conductivity. Furthermore, CNTs have also been used as contrast agents in optoacoustic mapping of the sentinel lymph node, lymphatic vessels, and optoacoustic molecular imaging of glioblastoma tumors and certain cancerous cells [110-113]. OAI can benefit of the high absorbance of CNTs, since they contain impurities in the form of metallic nanoparticles. Figure 3.2 shows the solution of DWCNTs dispersed in distilled water and used for our optoacoustic experiments (see section 4.2.1). Figure 3.3 shows a typical spectrum of absorbance of DWCNTs in the visible and NIR ranges.

Figure 3.2. Samples of DWCNTs used in our optoacoustic experiments (concentration of 0.1 mg/ml in distilled water).

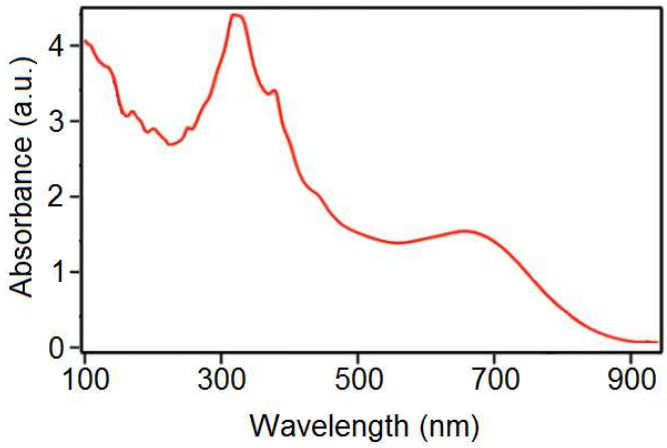

Figure 3.3. Typical absorbance spectrum of DWCNTs in visible and NIR ranges.

The physical properties of CNTs can be manipulated to be subjected to different methods of biomedical imaging in order to analyze and improve their functionalities and response to their environment.

3.3. Graphene oxide nanoparticles

Similarly to CNTs, graphene oxide (GO) is a derivative of graphene, composed of carbon, oxygen, and hydrogen in variable ratios, obtained by synthetizing sheets of graphite in a single-layer of 2-D nanostructure. Compared to CNTs, GO nanoparticles possess a larger surface area and lower aspect ratio. Graphene has many unusual properties, such as excellent thermal and electrical conductivity, flexibility, mechanical strength, and biocompatibility. Research studies on graphene oxide are mainly addressed to the fields of electronics, photonics, and biomedical imaging. In biomedical imaging techniques, GO nanoparticles are synthetized for drug delivery and cancer imaging and treatment [114-116]. One of the potential interesting field is OAI, where GO can be applied as exogenous contrast agents for cancer imaging. Reduced graphene oxide (rGO) is formed by residual oxygen and other heteroatoms and can be made as a thin film from an aqueous dispersion of GO in water with moderate conductivity. Normally, it is attractive for use in electronic devices. In addition, GO and rGO are used in nanocomposite materials, polymer composite materials, and biomedical applications. Figure 3.4 shows the molecular structure of GO and Figure 3.5 shows both the processes of synthetization of GO from graphite and rGO from GO. The addition of gold nanostructures with graphene produces the graphene–gold nanorods hybrid (rGO@Au) nanocomposite which provides additional properties, such as higher effective surface area, catalytic activity, electrical conductivity, water solubility, and biocompatibility (Fig. 3.6).

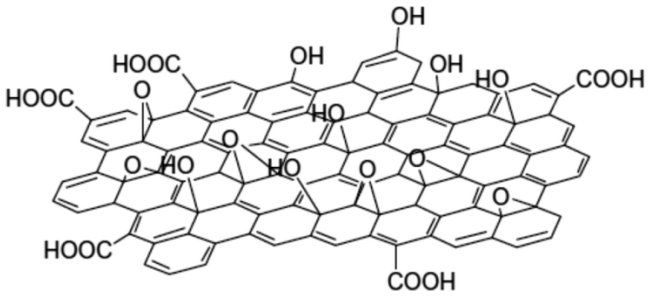

Figure 3.4. Molecular structure of GO composed of carbon, oxygen, and hydrogen in variable ratios [117].

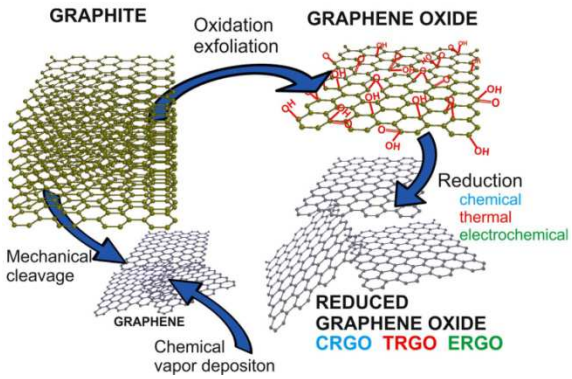

Figure 3.5. A scheme showing the various steps of preparation of GO and rGO. GO is prepared by oxidation/exfoliation of graphite layers, while rGO by either chemical (CRGO: chemically reduced graphene oxide) or thermal (TRGO: thermally reduced graphene oxide) or electromechanical reduction (ERGO: electrochemically reduced graphene oxide) [118].

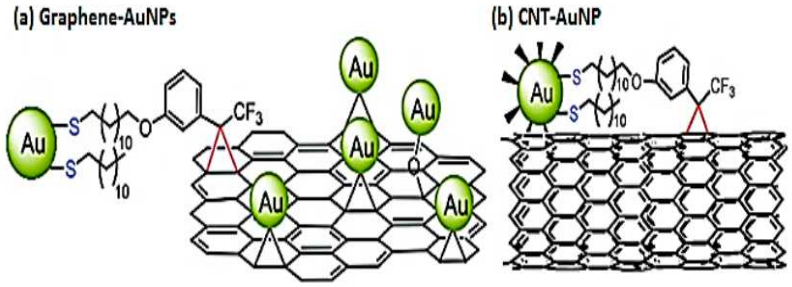

Figure 3.6. Chemical synthetization of rGO@Au with deposition of gold nanorods nanoparticles to GO [119].

Figure 3.7 shows three solutions of GO, rGO, and rGO@Au dispersed in propanol and used for our optoacoustic experiments (see section 4.2.3). The dispersion of all the solutions is not optimal, especially of rGO@Au, due to the precipitation of the heavy gold nanoparticles deposited on GO nanostructures. The solutions have been shaken immediately before the measurements by using an ultrasonic cleaner to avoid that the precipitation of nanoparticles altered the measurements of absorption coefficient and optoacoustic signals. Figure 3.8 shows the absorbance spectrum of both GO and rGO in the visible and NIR ranges, considering a nanoparticles concentration of 50 µg/ml. In the experiments presented in section 4.2.3, these nanoparticles will be used in concentrations of 25 mg/ml (500 times more) to generate optoacoustic signals at 870 and 905 nm. As we can see in Figure 3.8, the absorbance is very low to generate sufficiently high optoacoustic signals. Despite their low toxicity, the drawback of these nanoparticles is that they do not show absorption peaks in the NIR range. Conversely, the gold nanorods, as we will see in the next section, present the possibility of being tuned at the desired wavelength by changing both their aspect ratio and size. In their case, it would not be necessary to use such high concentration (i.e. 25 mg/ml) to achieve appreciable optoacoustic signals, but values of ~ 25-30 times less. In fact, it would be advantageous to use low quantity of nanoparticles for biomedical imaging applications requiring minimally invasive in-body injection of contrast agents.

Figure 3.7. Samples of GO, rGO, and rGO@Au used in our optoacoustic experiments (concentration of 50 µg/ml).

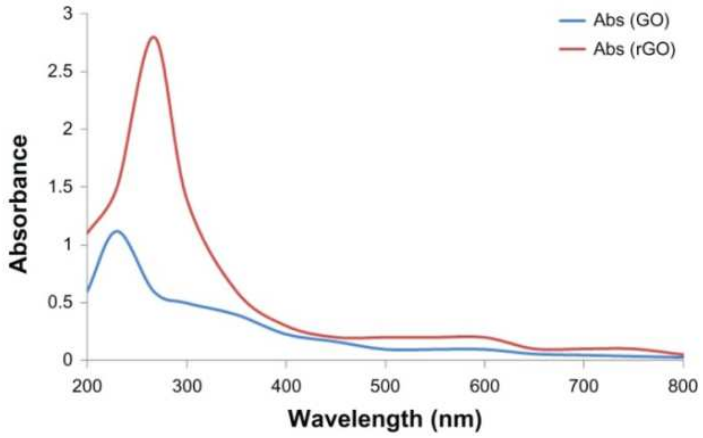

Figure 3.8. Absorbance spectra of GO and rGO in visible and NIR ranges (concentrations: 50 μg/ml) [120]. The higher absorbance of rGO is due to the presence of gold nanoparticles conjugated to the graphene structure.

The safety of carbon nanoparticles is a critical consideration in their development for biological uses. The biocompatibility of carbon nanoparticles is determined by the surface physical and chemical properties, including surface chemistry and particle size. The tolerable dose is ultimately limited by their accumulation and elimination from the body, as no known biological process can degrade carbon nanomaterials. Thus, the safety of carbon nanoparticles still needs extensive investigation before their use in humans [107].

3.4. Gold nanorods

Gold nanorods are a kind of rod-shaped plasmonic nanoparticles with dimensions ranging between 1 and 100 nm and aspect ratios between 1.5 and 25. They are produced by direct chemical synthesis, in which the different sizes of the nanorods are growth at different rates, producing an elongated object (Fig. 3.9).
They are considered as attractive new nanomaterials which have found a wide range of applications in the biomedical field.
Their physical and geometrical properties provide them high tunable absorption peaks in the NIR spectrum, due to their tunable surface plasma resonance. In addition, they generate heat transients when are excited with NIR radiation. All these special properties of gold nanorods make them potential optical contrast agents for cancer diagnosis and therapy in biomedical imaging and drug delivery [121, 122].
Gold nanorods are synthetized as colloidal solutions of nanoparticles suspended in another liquid substance, which is typically water, to form a homogeneous mixture. In this way, the gold nanorods mixture does not settle or take a very long time to settle appreciably (typically more than six months), keeping their characteristics for a sufficient time for their use in a biomedical environment. The most important feature of the colloidal solutions of gold nanorods is based on their optical properties which during synthesis can be tuned to specific wavelengths within the therapeutic window.
In cancer diagnostics, when a patient is exposed to NIR radiation, the high plasmonic resonance of gold nanorods selectively taken up by tumor cells allow a high imaging differentiation from the surrounding healthy tissues. Similarly, in cancer therapeutics the gold nanorods are locally heated, destroying only the cancerous tissue while leaving healthy cells intact (i.e. hyperthermia treatment [123]). When the cancer

treatment is more complicated, the drug delivery is a more preferred solution than hyperthermia. In this case, the gold nanorods can be conjugated with an anti-tumorigenic drug to provide tracking of the labeled cells and release their drug to the targeted cancer cells.
Undoubtedly, one potential application of gold nanorods is OAI, in which the high absorbance of these nanoparticles can be useful to target and differentiate the tumoral cells from other tissues. In sections 4.2.4 and 4.2.5 some interesting applications of gold nanorods applied for optoacoustic signal generation will be shown. To gain more insight into the behavior of gold nanorods, a theoretical analysis based on an extension of Mie's Theory presented by Gans for randomly orientated elongated cylinders is presented.

3.4.1. Optical properties of gold nanorods

The gold nanorods structure is especially appealing due to its unique optical properties and wavelength tunability within the optical therapeutic window. By controlling the shape and dimensions of the nanoparticles during their synthesis, the optical scattering and absorption can be tuned to specific wavelengths. This is particularly beneficial when they are used as optical contrast agents in biomedical applications. To understand this process, a numerical analysis based on the light/nanoparticle interaction has been developed to identify both the absorption and scattering properties in function of the nanoparticles dimensions. This procedure provides key information required during the synthesis of gold nanorods to control their wavelength tunability.
Gold nanostructures have unique surface plasmon resonance (SPR) which results from a collective coherent resonant oscillation with the external oscillating electromagnetic field. The wavelength of SPR is dependent on particle size, shape, structure, the dielectric properties of the metal, and the surrounding medium, as these factors affect the electron charge density on the particle surface [124].
Spherical gold nanoparticles have only one SPR peak in the visible region around 520 nm depending on size and dielectric environment which can be explained by Mie's theory [125].
Instead, the SPR properties of gold nanorods split into two distinct SPR bands which correspond to the oscillation of the free electrons along the transverse axis (the width or short axis) and the longitudinal axis (the length or long axis) of the rod. The *transverse surface plasmon* (TSP) in gold nanorods typically shows a resonance peak at ~ 530 nm, while the resonance of the *longitudinal surface plasmon* (LSP) is commonly found from visible to NIR region of the electromagnetic spectrum with increasing aspect ratio. The position of the LSP is dependent on the aspect ratio of the gold nanorod, which is given by $R = L/W$, where L is the length and R the width (Fig. 3.9).

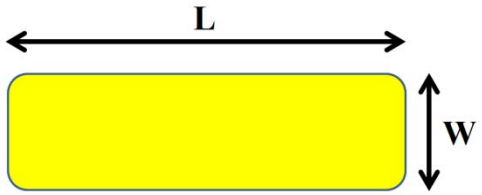

Figure 3.9. Geometrical structure of the gold nanorod. The aspect ratio (*R*) of a nanorod is given by *R = L/W*.

Figure 3.10 shows two solutions of gold nanorods dispersed in distilled water with absorption peak at ~ 860 nm and ~ 900 nm and used for our optoacoustic experiments (see sections 4.2.4 and 4.2.5). In Figure 3.11 the absorbance spectra of several solutions of gold nanorods with different diameters are presented

over the wavelength range from 450 nm to 1500 nm. The TSPs can be noticed in the lower part of the spectrum, while the LSPs occur more ahead in the NIR range. It can be noticed that the absorbance peaks of the LSPs equal 100 with relatively low concentrations of gold nanorods (between 3.5 and 5 mg/ml). Due to minimal NIR light absorption by most human tissues and water in the NIR (700–1300 nm), gold nanorods exhibiting strong NIR absorption and scattering are very attractive for in vivo biomedical imaging and drug delivery and therapy applications [126].

Figure 3.10. Samples of gold nanorods used in our optoacoustic experiments (concentration of 0.8 and 0.9 mg/ml, respectively).

Gold nanorods with high optical density (O.D.) are considered as a potential contrast agent for discrimination and targeting of cancer and other diseases in OAI, since their absorption peaks can be adjusted to the emission wavelength of the laser source by varying their dimensions at nanoscale.

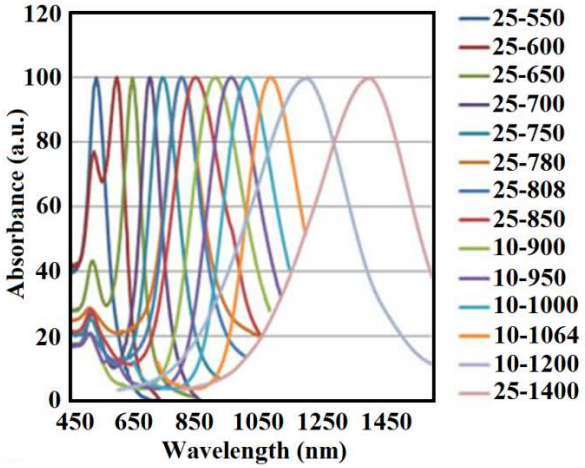

Figure 3.11. Absorbance spectra of gold nanorods with different diameters *W* (i.e. 10 nm and 25 nm) in the visible/NIR range. The concentrations are 3.5 mg/ml (10-nm diameter gold nanorods) and 5 mg/ml (25-nm diameter gold nanorods) (reprinted from [127]). The absorbance peaks are associated with plasmon oscillations in the longitudinal and transverse directions.

Both Rayleigh's and Mie's theories, which are both based on Maxwell's equations, can be used to model the scattering of a plane monochromatic optical wave by a single spherical particle [125, 128]. The main assumption of both theories is that the particle and its surrounding medium are both homogenous and can be described by their bulk optical refractive index (i.e. by a single refractive index at a given wavelength). Rayleigh's theory describes the light scattering by particles which have dimensions much smaller than the wavelength of the incident radiation. This theory is only valid when the size of a scatterer, defined as $x = 2\pi r/\lambda$ (where r is the characteristic dimension of the particle and λ is the operating wavelength) is much smaller than 1. Normally, the gold nanorods have size comparable with the NIR peak wavelength (normally no more than 10 %). Instead, Mie's theory was developed for particles of a spherical nature only. In order to model the optical properties of nanorod structures, an extension of Mie's theory has been developed by Gans [129, 130], which is based on a dipole approximation. This theory determines the relation between gold nanorods structures and both the LSP and TSP peaks. Another technique used to model the optical properties of gold nanorods is the discrete dipole approximation (DDA) developed by Purcell and Pennypacker [131], which is a method for calculating the optical properties of particles of arbitrary shapes [132, 133].

According to Gans' theory, the extinction coefficient of randomly oriented ellipsoidal- or rod-shaped particles can be modeled by introducing a geometrical factor P_j which corresponds to each axis A or B of the particle (see Fig. 3.12). The formulas for the absorption and scattering cross sections, σ_{abs} and σ_{sca}, respectively, are given by the following equations [80]:

$$\sigma_{abs} = \frac{2\pi V \varepsilon_{med}^{3/2}}{3\lambda_0} \sum_{j=A}^{B} \frac{\left(\frac{1}{P_j^2}\right)\varepsilon_{imag}}{\left[\varepsilon_{real} + \left(\frac{1-P_j}{P_j}\right)\varepsilon_{med}\right]^2 + \varepsilon_{imag}^2}, \tag{3.1}$$

$$\sigma_{sca} = \frac{8\pi^3 \varepsilon_{med}^2 V^2}{9\lambda_0^4} \sum_{j=A}^{B} \frac{\left(\varepsilon_{real} - \varepsilon_{med}\right)^2 + \frac{\varepsilon_{imag}^2}{P_j^2}}{\left[\varepsilon_{real} + \left(\frac{1-P_j}{P_j}\right)\varepsilon_{med}\right]^2 + \varepsilon_{imag}^2}, \tag{3.2}$$

where V is the volume of the particle calculated as a cylinder, i.e. $V = \pi A\left(B/2\right)^2$ (see Fig. 3.12), ε_{med} represents the dielectric constant of the surrounding medium, ε_{real} and ε_{imag} represent the real and imaginary part of the complex electric permittivity of gold, respectively, which can be found by the following equations:

$$\varepsilon_{real} = n_{real}^2 - n_{imag}^2, \tag{3.3}$$

$$\varepsilon_{imag} = 2n_{real}n_{imag}, \tag{3.4}$$

The geometrical factors P_j along the A and B axes are defined as [80], where R is the aspect ratio:

$$P_A = \frac{2}{R^2-1}\left[\frac{R}{2\sqrt{R^2-1}}\ln\left(\frac{R+\sqrt{R^2-1}}{R-\sqrt{R^2-1}}\right)-1\right], \tag{3.5}$$

$$P_B = \frac{1-P_A}{2}. \tag{3.6}$$

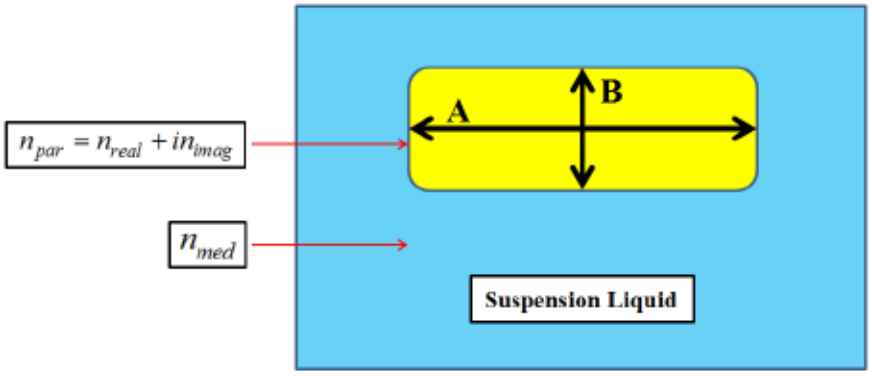

Figure 3.12. Gold nanorods of refractive index $n_{par} = n_{real} + in_{imag}$ within a suspension liquid with refractive index n_{med}.

In [80], the dependence of the aspect ratio on the position of the LSP peak of gold nanorods has been investigated and a linear relation between these terms has been observed. It has been assessed that the aspect ratio of the nanorod increases with the shift of the LSP peak position to longer wavelengths and increases in amplitude, while the TSP peak moves to shorter wavelengths and decreases in amplitude. Experiments demonstrated that the relation between the wavelength LSP peak λ_{peak} and the aspect ratio R of gold nanorods is constant, considering the numerical analysis of Weaver and Frederikse (Eq. 3.7) [134] or Johnson and Christy (Eq. 3.8) [135]:

$$\lambda_{peak} = 110.04R + 357.71, \tag{3.7}$$

$$\lambda_{peak} = 107.14R + 350.78. \tag{3.8}$$

Similarly, it has been demonstrated a linear relation between the position of the LSP peak and the dielectric constant ε_{med} of the surrounding medium. In this case, the experiments give the following equations, considering the numerical analysis of Weaver and Frederikse (Eq. 3.9) or Johnson and Christy (Eq. 3.10):

$$\lambda_{peak} = 60.52\varepsilon_{med} + 477.92, \tag{3.9}$$

$$\lambda_{peak} = 58.4\varepsilon_{med} + 470.01, \tag{3.10}$$

The synthesis of gold nanorods used as optical contrast agents requires a careful selection of the nanorod properties, such as the wavelength tuning of the optical absorbance peaks.

3.4.2. Synthesis and bio-conjugation of gold nanorods

A variety of approaches has been developed for the synthesis of gold nanorods, mainly including electrochemical, photochemical, and seed-mediated growth methods. Among these, the seed-mediated growth method is the most widely used, due to its simplicity, high quality, and particle size controlling.

In the seed-mediated approach, gold nanorods with different aspect ratios are produced by growing colloidal gold seeds (~1.5–4 nm) in a bulk $HAuCl_2$ solution using cetyltrimethylammonium bromide (CTAB) surfactant. The size and aspect ratio of gold nanorods can be influenced by many parameters, such as seed concentration, seed size, reductant concentration, temperature, gold concentration and surfactant concentration.
Gold nanorods synthesized by seed-mediated growth method have a strong coating of CTAB surfactant, which provides the surface of nanorods with a positive surface charge, and thus ensure their stability in aqueous solution via electrostatic repulsion. Moreover, CTAB-coated gold nanorods exhibit cytotoxicity to most cells, due to the CTAB surfactant itself and the residual CTAB. In this way, it would be necessary to remove or replace CTAB for the advanced utilization of gold nanorods in various biomedical applications. Several methods have been developed for conjugation of biomolecules to gold nanorods, including direct ligand exchange, covalent coupling, electrostatic adsorption and surface coating [124].
Figure 3.13 shows a colloidal solution of CTAB-coated gold nanorods that are randomly oriented in a fluid (i.e. distilled water).

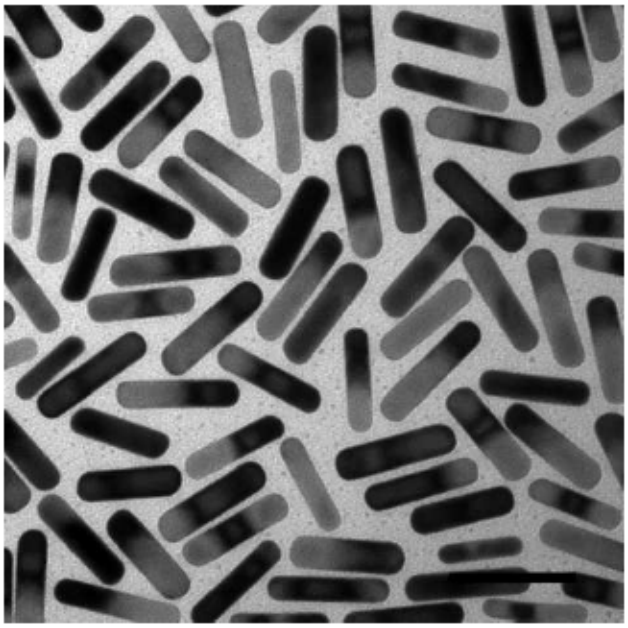

Figure 3.13. Colloidal solution of CTAB-coated gold nanorods [127].

3.4.3. Biomedical applications of gold nanorods

Gold nanorods have several remarkable properties, such as strong plasmon absorption band tunable from visible to NIR, enhanced scattering cross section and long term photostability. All these features make gold nanorods very useful for biomedical imaging. The biomedical imaging modes for gold nanorods include two-photon enhanced luminescence (TPL), dark-field mode microscopy, transmission electron microscopy (TEM), optical coherence tomography (OCT), and OAT. Among the optical imaging technologies, fluorescence imaging is a desirable modality for early cancer detection due to its low cost, high sensitivity and high spatial resolution. Gold nanorods are considered as ideal contrast agents for OAI due to their strong surface plasmon absorption in the NIR region, where tissue absorption in this region is rather low. Gold nanorods have great potential for both *in vitro* and *in vivo* OAI [136] and have been studied by a few researchers.
Experimental studies carried out OAI in mice found that gold nanorods can significantly enhance differences in signal intensity with low concentration gradients [137]. Further studies used antibody-conjugated gold nanorods for *in vivo* breast cancer in OAI [138]. In addition, the ability of silica coatings on gold nanorods to increase the signal-to-noise ratio of OAI has been compared with uncoated gold nanorods [139].

3.5. Conclusions

In this chapter an overview of the optical properties of different kinds of nanoparticles for applications as contrast agents for *in-vivo* optical-based diagnostic techniques has been presented. Generally, the characteristics of nanoparticles allow a preferential accumulation within cancerous tissues instead of healthy tissues, with the aim of providing enhanced image contrast.

The optical properties of the CNTs depend on the different angles and curvatures of their structure and on their number of rolls. The absorbance profile of the nanoparticles has been identified as the key tool to identify the resonance peaks in the electromagnetic spectrum. In particular, the optical absorbance of the DWCNTs in the visible and NIR spectra has been shown. The absorption peak of DWCNTs occurs at ~ 300 nm, which is far away from the wavelengths applied in this thesis.

Similarly, the molecular structure of graphene-oxide nanoparticles improves their absorption in the same range of wavelengths. Since both these nanoparticle structures do not exhibit absorption peaks in the NIR range, they need to be used in larger concentrations if compared to the gold nanorods structures, which are more selective and tunable in the NIR range.

In this regard, the growing interest in the use of nanostructures for biomedical applications has stimulated the development of new techniques for the synthesis of gold nanorods, allowing them to be manipulated in both size and geometry with the aim to achieve certain optical properties. The gold nanorods have been shows as versatile nanostructures with rod-like shape for optoacoustic applications, due to their selective high absorption peaks in the visible and NIR ranges. The other presented advantage of gold nanorods nanoparticles when compared with other nanostructures is that they can be applied as localized absorbers for improved phototherapy based on hyperthermia treatment.

The concepts of transverse and longitudinal surface plasmon (i.e. their absorption peaks) have been shown, remarking how they are dependent on the aspect ratio of gold nanorods. According to Gans'

theory, the extinction coefficient of randomly oriented ellipsoidal- or rod-shaped particles has been modelled. The constant relations of the wavelength LSP peak with both the aspect ratio of gold nanorods and the dielectric constant of the surrounding medium have been discussed.

The nanoparticles presented will be applied in the next chapter to generate optoacoustic signals using high power diode laser sources operating at 870 nm, 905 nm, and finally 972 nm.

Chapter 4

Development of a multi-wavelength system based on high-power diode laser sources for optoacoustic signal generation with nanoparticles

4.1. Introduction

In Chapter 1 it has been asserted that pulsed HPDLs are a potential and cheaper alternative to solid state lasers for the generation of optoacoustic signals, due to their low cost, small size and high repetition rates. In addition, it has been discussed that their limitations in optical power can affect the strength of the optoacoustic signals. In this regard, the amount of optical power can be increased by arranging several HPDLs in side-by-side arrays. Diode lasers are available in the market in a wide range of wavelengths but there are a few pulsed HPDLs. Multi-wavelength laser sources are important in some optoacoustic applications that require the spectroscopic characterization of the tissue chromophores. The principles of optoacoustic signal generation have been introduced in Chapter 2 and will be applied in this chapter to the experiments. In the previous chapter, some different kinds of nanostructures and nanoparticles have been introduced with their physical characteristics and optical properties, discussing their applicability to OAI. The work presented in this chapter is dedicated to the design of a multi-wavelength optoacoustic system based on pulsed HPDL sources. The progress of our optoacoustic setup will be described step-by-step, showing some experimental results achieved by using nanoparticles (see Chapter 3) as absorbers to generate optoacoustic signals. As it has been shown in the previous chapter, the DWCNTs and graphene oxide nanoparticles do not show absorption peaks in the NIR range, but they are useful to achieve valuable results. The crucial point of this chapter will be reached with the experiments on gold nanorods, whose advantage is due to a tunable absorption peak in the NIR range.

The layout of this chapter is organized as follows: first of all, it will be shown our early setup consisting of small arrays of HPDLs sources with respective emission at 870 nm and 905 nm, illuminating a solution of DWCNTs hosted in a tissue-like cylindrical phantom to generate optoacoustic signals. Then, the principles of light coupling of HPDLs into optical fibers, which are joined all together forming a fiber bundle built in-house, will be shown for a successive improvement of the optoacoustic setup. With this setup, optoacoustic signals will be generated with graphene-based (at 905 nm only) and gold nanoparticles solutions (at both wavelengths) hosted in phantoms. The optoacoustic signals generated with DWCNTs will be compared to those generated with an ink solution. The results will show low optoacoustic signals with DWCNTs (~5 mV), which is mainly due to their low concentration (0.1 mg/ml). In the case of graphene, the amplitude of the optoacoustic signals is significantly improved (~25 mV), due to a much higher nanoparticles concentration (i.e. 25 mg/ml). However, in the case of gold nanorods the optoacoustic signal amplitude is much higher (~50/60 mV), even though the concentration is low (i.e. 0.8 mg/ml), due to their high absorption peaks at the wavelengths of our interest. Subsequently, the optoacoustic system will be further improved including a microcontroller to electronically alternate

the pulses between the two wavelengths in order to determine the absolute concentrations of some gold nanorods solutions hosted in quartz cuvette. This experiment would be useful in real OAI applications to detect and quantify the presence of chromophores with the help of contrast agents (i.e. gold nanorods). Results will show a maximum observational error of 2.76 % from the expected values. Finally, it will be discussed that this value can be further reduced by adding a third wavelength to the optoacoustic system. In this regard, a 972-nm DLB will be added to the system to reduce the margin of error to 1.34 %. In Appendix A, more details about the physical principles of the diode laser devices and their functional characteristics for optoacoustic applications will be presented.

4.2. Optoacoustic setup

In this section, the different steps related to the development of the optoacoustic system based on HPDLs are described. The initial excitation system was composed of two synchronized pairs of pulsed HPDLs operating at 870 nm (L11348-330-04, Hamamatsu Photonics K.K.) and 905 nm (SPL PL90_3, OSRAM Opto Semiconductors GmbH), respectively. Each HPDL was pulsed by a diode laser driver (PCO-7120, IXYS Colorado). The emitting area is 300 μm x 10 μm in 870-nm HPDLs and 200 μm x 10 μm in 905-nm HPDLs. The HPDLs have been combined to increase the total power delivered to the absorber, but also to enhance the signal-to noise ratio (SNR) of the optoacoustic signals. Table 4.1 summarizes the characteristics of HPDLs used in our experiments.

Table 4.1. Characteristics of the 870-nm and 905-nm HPDLs.

Characteristics	870-nm HPDL	905-nm HPDL
Peak power (max)	90 W	90 W
Forward current (max)	35 A	40 A
Pulse width (max)	100 ns	100 ns
Duty cycle (max)	0.075%	0.1%
Wavelength (typ.)	870 nm	905 nm
Aperture size	300 μm × 10 μm	200 μm × 10 μm
Divergence angles	10°, 24°	9°, 25°

4.2.1. Light coupling with lens tubes

In order to focus the laser light into the target (i.e. an optical phantom) in which the absorbing inclusions (i.e. ink and DWCNTs) have been located, a lens system composed of a collimating lens (effective focal distance f_{EFL1} = 6.24 mm) and a focusing lens (effective focal distance f_{EFL2} = 40 mm) with anti-reflection coating (600-1050 nm) has been used. Thus, in accordance with the optical magnification law ($M = f_{EFL2}/f_{EFL1} \approx 6.4$), the light spots incoming on the phantom surface had an area of 1920 μm × 64 μm and 1280 μm × 64 μm, respectively at 870 nm and 905 nm. A simple schematic of the measurement setup used for the measurements with DWCNTs embedded in a tissue-like phantom is illustrated in Figure 4.1. Figure 4.2 shows the HPDLs combined in a semi-circular arrangement to illuminate the absorbing sample in the middle of the phantom. The characteristics of the lens system used in the optoacoustic setup are summarized in Table 4.2.

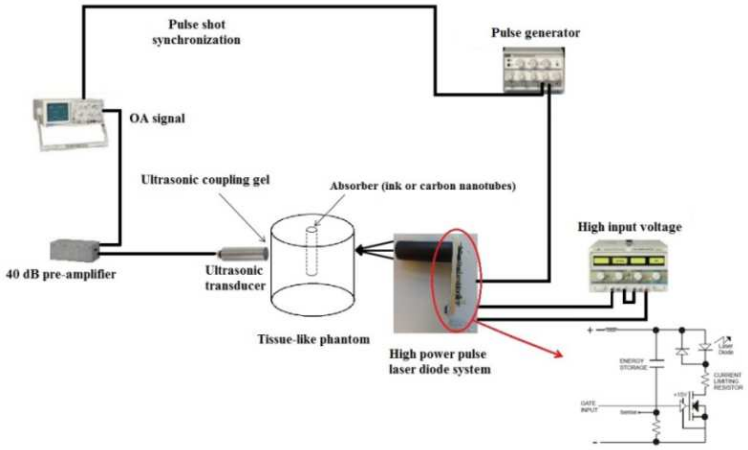

Figure 4.1. Schematic of the optoacoustic setup used.

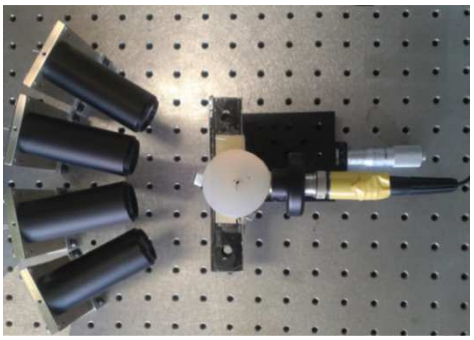

Figure 4.2. Block of four HPDLs in a semicircular configuration.

Table 4.2. Characteristics of the lens system used in the optoacoustic setup with the corresponding magnification.

Component	Focal length	Magnification
Collimating lens	6.24 mm	6.4
Focusing lens	40 mm	

4.2.2. Light coupling into optical fibers and fiber bundle

The lens tubes of the previous section (Fig. 4.2) do not provide a stable alignment and need to be replaced with more stable optical fiber connections to be applicable in a realistic scenario. This optical configuration necessitates an improvement to ensure that the samples are uniformly illuminated with synchronized pulses. In addition, the beam coupling of HPDLs into optical fibers is necessary for both endoscopic and free space optoacoustic applications, due to their versatility and practicability. The new design presented in the following makes use of optical fibers collected in fiber bundles to couple the light of the HPDLs. A sketch of beam coupling of a HPDL into an optical fiber is illustrated in Figure 4.3.
Individual lens systems formed by a collimating lens (effective focal length f_{EFL1} = 6.24 mm) and a focusing lens (f_{EFL2} = 3.1 mm) with anti-reflecting coatings (600-1050 nm) have been used to couple the light emitted by each HPDL into the optical fibers (Fig. 4.3) using a three-axis translation mount

(CXYZ05, Thorlabs Inc.) to ensure optimum alignment (Fig. 4.4). With this coupling arrangement, a magnification $M_1 = f_{EFL2}/f_{EFL1} \approx 0.5$ in both axes was achieved. The lenses have an aspheric surface to correct the aberrations of focusing. With this new scheme, the output of each HPDLs has been combined side-by-side using a fiber bundle produced in-house, composed of seven multimode optical fibers (FT200EMT, Thorlabs Inc.), each with a 200-µm-core diameter and the numerical aperture (NA) of 0.39.

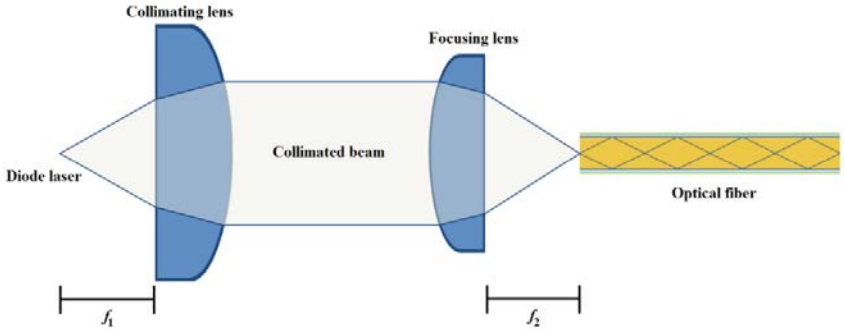

Figure 4.3. Scheme of light coupling of diode laser light into an optical fiber.

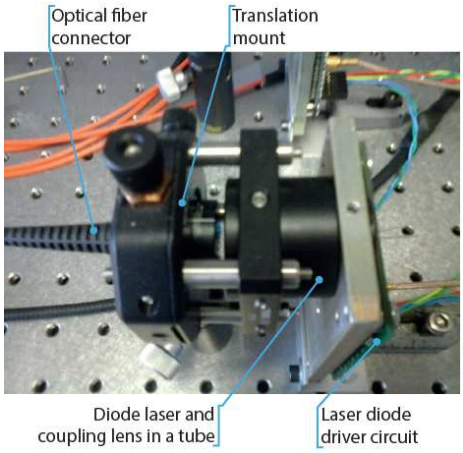

Figure 4.4. Coupling system consisting of two lenses and a three-axial translator used to optimize the beam coupling of each HPDL into the optical fiber. Light coming out from the lens system, located in the tube, is focused on the optical fiber after position adjustment.

Figure 4.5 shows a fiber bundle composed of seven optical fibers, from the top view and seen under a microscope. During the fabrication process of the fiber bundles, the fibers have been first connectorized using epoxy and afterwards cleaved using ruby scriber and polished. Two fiber bundles have been fabricated with output diameter of 675-µm and 1.2-mm, composed of 200-µm and 400-µm optical fibers (N.A. = 0.39), respectively. Figure 4.6 shows a front view of an array of HPDLs coupled to optical fibers by means of xyz translation mounts.

The single optical pulses emitted by the HPDLs have been previously synchronized at both wavelengths before measurements (Fig. 4.7). The optical pulses of the HPDLs have been measured individually at the output of the optical fiber bundle. Successively, the optical pulses have been measured for all three HPDLs operating all together. The amplitudes of the optical pulses have been normalized to their maximum values in order to simplify the comparison. The combined optical pulses in Figure 4.7 have the same shape, the same rise and fall times of the individual HPDLs. The output signal from each HPDL has

been perfectly overlapped in time and the output power was the addition of the power of the individual diode lasers. In Appendix B the coupling efficiencies of 870-nm and 905-nm HPDLs into a 600-µm endoscopic fiber will be shown.

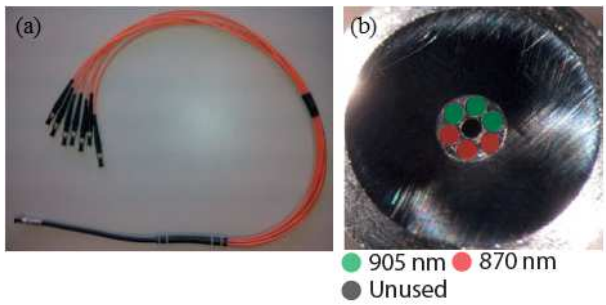

Figure 4.5. Fiber bundle with 675-µm diameter composed of seven 200-µm optical fibers: (a) before being mounted, (b) output end of the fiber bundle seen under a microscope (the positions of the optical fibers are symmetrical between the two wavelengths to ensure uniform illumination of the sample).

Figure 4.6. The beam emitted by the HPDLs is coupled side-by-side into optical fibers with variable core diameter by collimating and focusing lenses in a xyz translator mount.

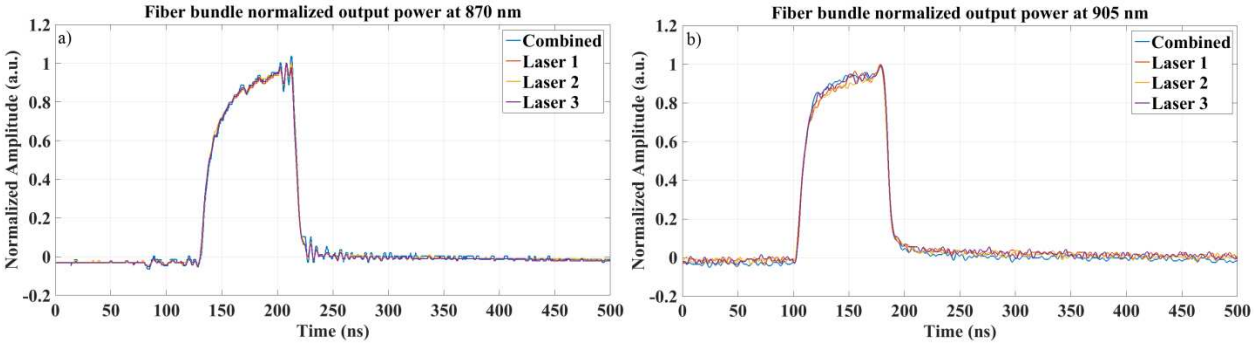

Figure 4.7. Synchronization between pulses of a) three 870-nm HPDLs and b) three 905-nm HPDLs.

At the output of the fiber bundle, the light beam had a circular shape but still diverged; hence, a secondary lens system has been used to properly focus the light beam into a spot (Fig. 4.8). This lens system has been properly chosen to minimize the power losses (collimating lens f_{EFL3} = 2 mm, focusing lens f_{EFL4} = 25.4 mm) with anti-reflection coating (600-1050 nm). Consequently, the circular light spot

emerging from the fiber bundle has been magnified, with $M_2 = f_4/f_3 \approx 12.7$. The characteristics of the lens systems used in the optoacoustic setup are summarized in Table 4.3.

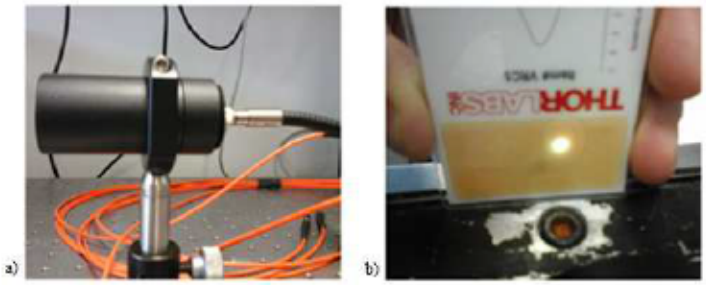

Figure 4.8. (a) A secondary lens system used to properly focus the light beam into a spot; (b) Image of the light spot (~ 3 mm^2) in the focal plane. The calculated spot area is ~ 1.2 mm^2, but it is actually larger due to the distance between the optical fibers in the bundle.

Table 4.3. Characteristics of the lens systems used in the optoacoustic setup with the corresponding magnifications.

Component	Focal length	Magnification
Collimating lens 1	6.24 mm	0.5
Focusing lens 1	3.1 mm	
Collimating lens 2	2 mm	12.7
Focusing lens 2	25.4 mm	

Figure 4.9 shows the optoacoustic setup used for the measurements with graphene-based nanoparticles embedded in an optical phantom. In a successive step, the same setup will be used for experiments with gold nanorods nanoparticles.

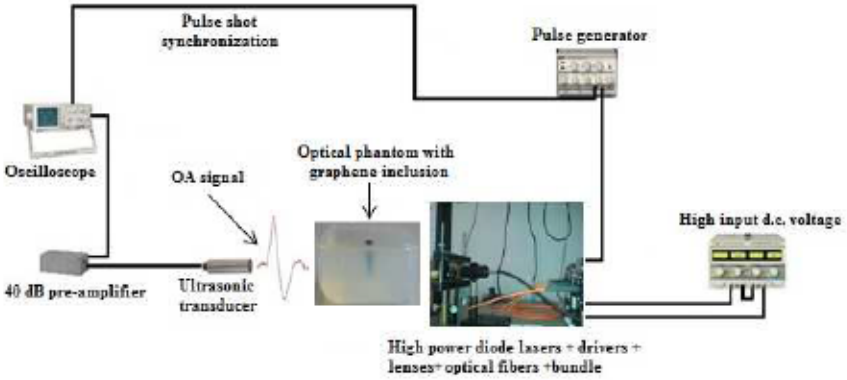

Figure 4.9. Schematic of the optoacoustic setup used for graphene-based inclusions.

4.3. Optoacoustic experiments

In this section, some experimental results with different kinds of nanoparticles (see Chapter 3) are evaluated. As first approach, a solution of DWCNTs with low concentration is used as optical absorber. Afterwards, graphene-oxide nanoparticles and gold nanorods are used in successive measurements steps.

4.3.1. Optoacoustic signals generated with double-walled carbon nanotubes

In this section, following the setup description of section 4.2.1, simple lens tubes are used to focus the light of 870-nm and 905-nm HPDLs into solutions of ink and double-walled carbon nanotubes (DWCNTs) hosted in optical phantoms for the generation of optoacoustic signals.
An optoacoustic system based on HPDLs at 870 nm and 905 nm is assembled to generate ultrasound signals from a DWCNTs solution (0.1 mg/ml in distilled water) arranged inside a tissue-like phantom, mimicking the scattering of a biological soft tissue (i.e. breast). Optoacoustic signals obtained with DWCNTs inclusions are compared with the case of ink-filled inclusions (0.7 % in distilled water) with the aim to assess their absorption. These measurements are done at 870 nm and 905 nm by using HPDLs as light sources. The results show that, depending on the absorption coefficients of the substances, the optoacoustic signal is relatively high when the inclusion is filled with ink and appreciable with DWCNTs.

4.3.1.1. Phantom preparation

Ultrasound phantoms typically mimic the acoustic properties of tissues, in terms of the speed of sound, absorption, and scattering [140, 141]. Normally, a tissue-like phantom is a composition of distilled water and gelatin, mixed with a scattering material. For our experiments, a 5.4-cm diameter cylindrical phantom made with a composition of 90% of neutral gelatin (translucent at optical frequencies) and 10% of agar (as a scattering material) diluted with distilled water (Fig. 4.10) is used. In this way, the scatterers of the agar suspended inside the phantom mimic the biopsy targets, making the measurements closer to the reality. After preparation process, 1 g of food preservative has been added to prevent the phantom from being attacked by bacteria and fungus within a short time. Table 4.4 summarizes the characteristics of the tissue phantoms.

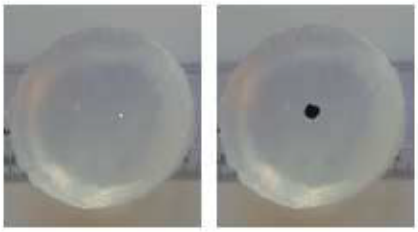

Figure 4.10. A tissue-like cylindrical phantom composed of 10% of agar and 90% of neutral gelatin, diluted with distilled water: a) directly after preparation, and b) with a 2 mm × 30 mm (diameter × height) ink-filled inclusion.

Table 4.4. Characteristics of the tissue phantoms.

Characteristics	Value
Composition	10% agar-agar
	90% gelatin
Size (Area x height)	22.9 × 4.0 cm^3
Volume of the hole filled with sample solution	60 mm^3
Hole diameter	2 mm

4.3.1.2. Determination of the absorption coefficients

The absorption coefficients μ_{abs} of the absorbers have been calculated using the following equation:

$$\mu_{abs} = \frac{-1}{d} \ln\left(P_{abs} / P_{\max}\right), \tag{4.1}$$

where d is the absorber thickness, P_{abs} is the average power transmitted through the absorber, and $P_{\max}$ is the maximum average power detected without the absorber. Eq. (4.1) neglects the contribution of optical scattering within the sample. Table 4.5 shows the estimated values of the absorption coefficients of black ink (0.7 %) and DWCNTs (0.1 mg/ml) using Eq. (4.1) at both 870 nm and 905 nm. As shown in Table 4.5, the absorption coefficient of black ink is significantly higher than DWCNTs at both wavelengths. The estimated absorption coefficients of DWCNTs (0.1 mg/ml) are approximately 5.6% and 5.7% of black ink at 870 nm and 905 nm, respectively. Nevertheless, these values demonstrate that DWCNTs have an appreciable absorption when they are embedded in a soft phantom, although the contribution from scattering is not resolved here.

Table 4.5. Estimated absorption coefficients of black ink and DWCNTs.

	Absorption coefficient	
Inclusion substance	**870 nm**	**905 nm**
Black ink (0.7 %)	6.59 cm^{-1}	6.82 cm^{-1}
DWCNTs (0.1 mg/ml)	0.37 cm^{-1}	0.39 cm^{-1}

4.3.1.3. Results and discussion

Pulse widths between 50 ns and 100 ns are used by steps of 10 ns and with a repetition rate of 1 kHz. The total energy per pulse delivered on the phantom by each couple of HPDLs was 8 μJ and 16 μJ for a pulse width of 50 ns and 100 ns, respectively. Consequently, the total energy density per pulse (with two HPDLs combined) at 870 nm was ~ 65.10 μJ/mm^2 and 130.20 μJ/mm^2 for a pulse width of 50 ns and 100 ns, respectively. Similarly, the total energy density per pulse at 905 nm was ~ 97.66 μJ/mm^2 and 195.31 μJ/mm^2 for a pulse width of 50 ns and 100 ns, respectively. Table 4.6 summarizes all the characteristics of the optical pulses applied at 870 nm and 905 nm. A 2-mm-diameter absorber inclusion embedded in the middle of the phantom has been used to generate the optoacoustic signals. A 1-MHz acoustic transducer (V303, Olympus Corp.) has been used to detect the optoacoustic signals generated. The output from the transducer was amplified 40 dB and subsequently visualized on the oscilloscope.

The optoacoustic signals generated by the absorbers have been excited with pulse widths varying from 50 to 100 ns, with the aim to evaluate the increase of the optoacustic signal. The repetition rate was 1 kHz in each case and the duty cycle varied between 0.005% and 0.01%. In Figure 4.11, the optoacoustic signal generated by 870-nm excitation using a 2-mm black ink inclusion ($\mu_{ink} = 6.59\ cm^{-1}$) is depicted. The amplitude varies from 6.0 mV (at 50 ns) to 11.2 mV (at 100 ns). In Figure 4.12, the optoacoustic signal generated by 905-nm excitation using a 2-mm black ink inclusion ($\mu_{ink} = 6.82\ cm^{-1}$) is considerably higher than the previous case, varying from 8.6 mV (at 50 ns) to 17 mV (at 100 ns). We can attribute this

increase primarily to a considerably higher energy density at 905 nm, compared to 870-nm excitation (see Table 4.6), and in addition to a slightly higher absorption coefficient of ink at 905 nm.

Table 4.6. Characteristics of the optical pulses used for excitation of optoacoustic signals at 870 nm and 905 nm, respectively.

Parameter	870-nm HPDLs	905-nm HPDLs
Pulse width	50 ÷ 100 ns	50 ÷ 100 ns
Repetition frequency	1 kHz	1 kHz
Duty cycle	0.005 ÷ 0.01%	0.005 ÷ 0.01%
Total pulse energy	8 ÷ 16 μJ	8 ÷ 16 μJ
Total average power	8 ÷ 16 mW	8 ÷ 16 mW
Light spot area	1920 μm × 64 μm	1280 μm × 64 μm
Total pulse energy density	65.1 ÷ 130.2 $\mu J/mm^2$	97.66 ÷ 195.31 $\mu J/mm^2$
Total peak power delivered to sample	160 ÷ 320 W	160 ÷ 320 W

Figure 4.13 shows the optoacoustic signals detected by using a 2-mm inclusion of DWCNTs (0.1 mg/ml), when a couple of 870-nm HPDLs have been used as a pulsed light source. The optoacoustic signal varies from 2.8 mV (at 50 ns) to 4.4 mV (at 100 ns). Evidently, the DWCNTs produce an optoacoustic signal with a much lower energy (which is directly proportional to the optoacoustic signal voltage) than ink does. This is to be expected, because ink is a very strong absorber, but it is nonetheless a very encouraging result that an optoacoustic signal can be also detected using a turbid medium with a DWCNT inclusion. As in the previous measurements with ink, Figure 4.14 confirms that the optoacoustic signal exhibits higher peaks using the HPDLs emitting at 905 nm, which is not surprising as these lasers produce pulses with significantly higher energy density. The optoacoustic signal varies from 3.4 mV (at 50 ns) to 5.4 mV (at 100 ns). As shown in Table 4.5, DWCNTs have an absorption coefficient of $\mu_{DWCNTs} = 0.37\ cm^{-1}$ at 870 nm and of $\mu_{DWCNTs} = 0.39\ cm^{-1}$ at 905 nm, hence, it is possible that the slightly enhanced absorption at 905 nm also contributes to a stronger optoacoustic signal.

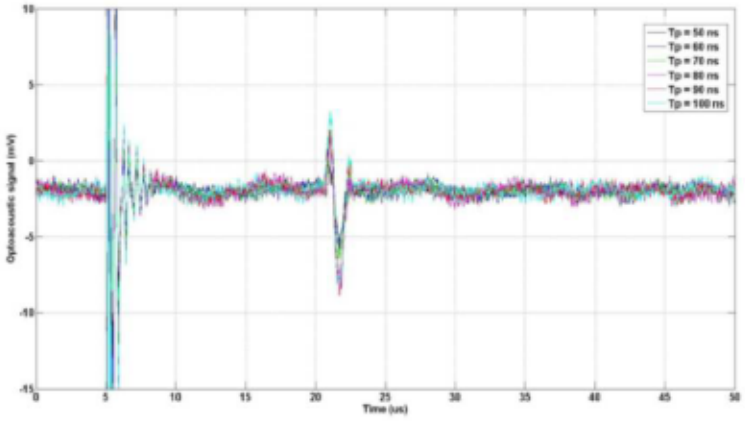

Figure 4.11. Optoacoustic signals from an ink-filled phantom generated by a couple of 870-nm HPDLs. The signal amplitude becomes appreciably stronger increasing the pulse width from 50 ns to 100 ns [142].

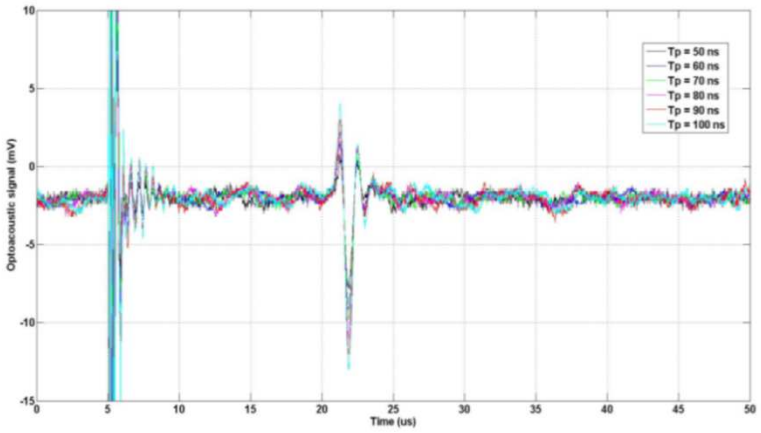

Figure 4.12. Optoacoustic signals from an ink-filled phantom generated by a couple of 905-nm HPDLs. The signal amplitudes are appreciably higher than those achieved by using 870-nm HPDLs [142].

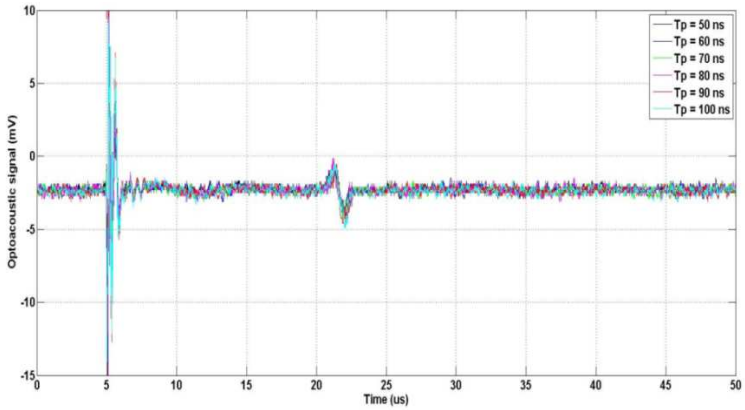

Figure 4.13. Optoacoustic signals from a DWCNT-filled phantom generated by a couple of 870-nm HPDLs. The signal amplitude becomes slightly stronger increasing the pulse width from 50 ns to 100 ns [142].

Comparing Figures 4.11-4.14, it can be asserted that the optoacoustic signals are stronger at 905 nm, primarily due to the higher energy density of the excitation pulses. The maximum peak-to-peak voltage observed using the black ink is 17 mV for 905-nm excitation and 11.2 mV for 870-nm excitation. The time of flight (TOF) in all the experiments is around 16 μs. The TOF corresponds to the time taken by the optoacoustic signal to travel from the absorber inclusion to the transducer surface. In Figures 4.11-4.14 it corresponds to the time gap between the trigger signal, which is an electromagnetic noise synchronized with the pulse shot, and the peak of the first optoacoustic signal. Table 4.7 summarizes the optoacoustic signals detected at 870 nm and 905 nm using ink and DWCNTs inclusions with a pulse width of 100 ns.
Table 4.7 shows that the optoacoustic signals achieved with DWCNTs represent ~ 39% and ~ 32% of those achieved with black ink at 870 nm and 905 nm, respectively. Figures 4.15 and 4.16 illustrate the rise in amplitude of optoacoustic signals by increasing the pulse width (and consequently the energy per pulse). It can be noticed how the ink-filled inclusions generate much higher optoacoustic signals than DWCNTs. The weak response of DWCNTs can be enhanced by combining more HPDLs.

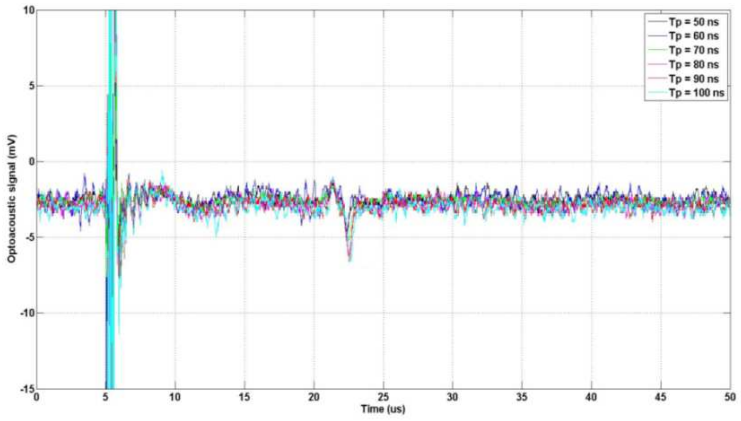

Figure 4.14. Optoacoustic signals from a DWCNT-filled phantom generated by a couple of 905-nm HPDLs. The signal amplitude becomes slightly stronger increasing the pulse width from 50 ns to 100 ns [142].

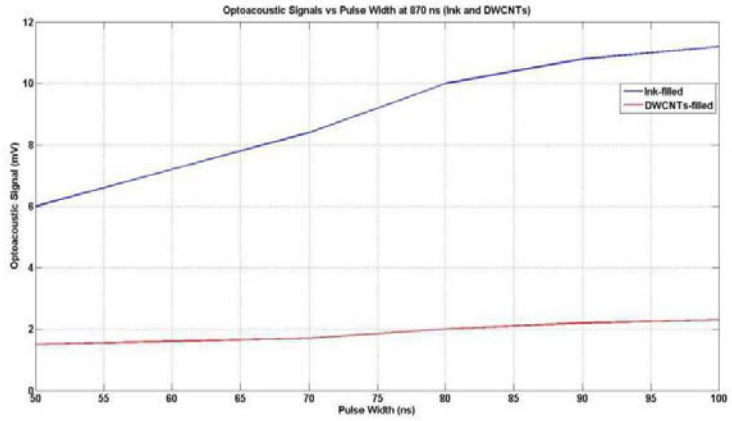

Figure 4.15. Variation of optoacoustic signal amplitude as a function of the pulse width applying 870-nm excitation to: ink-filled (blue) and DWCNT-filled (red) inclusions [142].

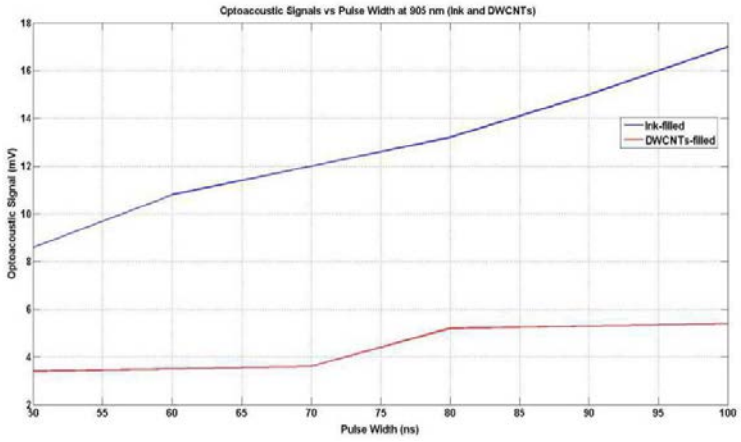

Figure 4.16. Variation of optoacoustic signal amplitude as a function of the pulse width applying 905-nm excitation to: ink-filled (blue) and DWCNT-filled (red) inclusions [142].

Table 4.7. Maximum optoacoustic signals achieved at 870 nm and 905 nm with a pulse width of 100 ns.

	Maximum optoacoustic signal achieved with 100-ns pulses	
Inclusion substance	**870 nm**	**905 nm**
Black ink (0.7%)	11.2 mV	17 mV
DWCNTs (0.1 mg/ml)	4.4 mV	5.4 mV

4.3.2. Optoacoustic signals generated with graphene-based solutions

In this section, the light beam of three 905-nm HPDLs has been coupled to optical fibers that were assembled in a fiber bundle, following the steps reported in section 4.2.2. For the moment, only three HPDLs operating at 905 nm are used for fiber coupling into optical fibers, but in the successive works three more HPDLs of 870 nm will also be used. The coupled light of each HPDL was focused on an absorber consisting of graphene-based nanomaterials (graphene oxide, reduced graphene oxide, and reduced graphene-oxide/gold-nanoparticle hybrid, respectively) diluted in ethanol and hosted in slightly scattering optical phantoms [64]. The optoacoustic signals generated from each solution are compared and it is shown that graphene-based nanomaterials are good candidates as contrast agents in biomedical applications. The excitation system was composed of three pulsed HPDLs operating at 905 nm, whose beams have been synchronized and coupled into a 675-µm fiber bundle composed of seven 200-µm optical fibers (Fig. 4.17).

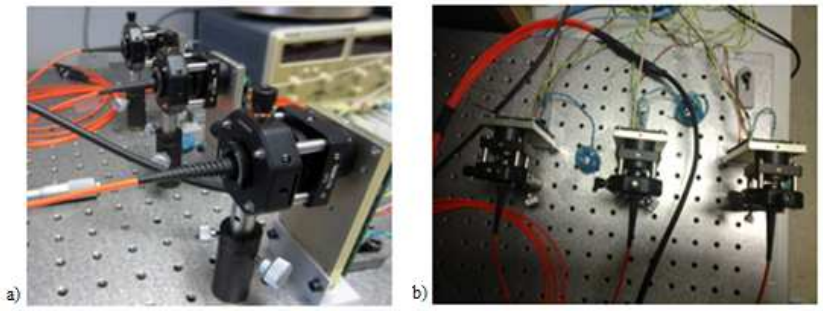

Figure 4.17. Light emitted by each HPDL is coupled to a 200-µm-core optical fiber by collimating and focusing lenses in a xyz translator mount: (a) Side view; (b) Top view.

4.3.2.1. Phantom preparation

Figure 4.18 shows a sample of a tissue phantom used in our experiments, which is composed of 10% of agar-agar (as a scattering medium) and 90% of neutral gelatin. The compound of these two materials gives a semi-transparent medium that can mimic an ideal soft tissue. The size of the phantoms is ~ 5.2 x 5.2 x 3.3 cm^3 with blunt edges, and the size of the central hole is ~250 mm^3. Table 4.8 summarizes the characteristics of the tissue phantoms.

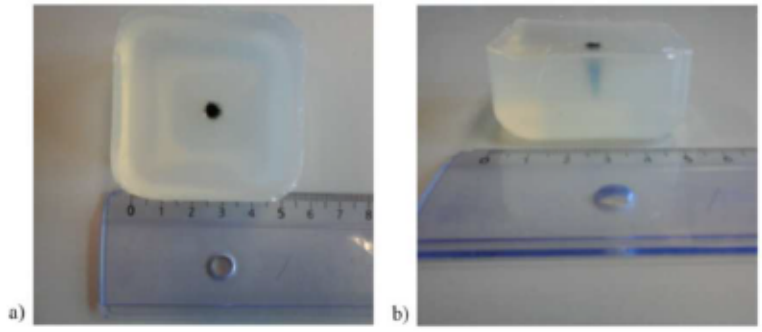

Figure 4.18. Optical phantom used in the experiments: a) Top view; b) Side view.

Table 4.8. Characteristics of the tissue phantoms.

Characteristics	Value
Composition	10% agar-agar
	90% gelatin
Size (Side x side x height)	$5.2 \times 5.2 \times 3.3$ cm^3
Volume of the hole filled with sample solution	250 mm^3
Hole diameter	4 mm

4.3.2.2. Determination of the attenuation coefficients

In this section, the characterization of the attenuation of the optical phantoms and graphene-based solutions used for our optoacoustic measurements is reported. Graphene-based nanomaterials are generating high interest for various biomedical applications [143-146], including their use as contrast agents for OAI [147-151]. For our studies, three graphene-based products distributed in powder form (NanoInnova Technologies SL) have been chosen: monolayer graphene oxide (GO), reduced graphene oxide (rGO) with oxygen to carbon ration of ~0.14, and reduced graphene oxide-gold nanoparticle hybrid (rGO@Au), with the gold content of ~2 wt% and an average size of gold nanoparticles of ~27 nm. It should be emphasized that none of the prior studies used diode lasers for excitation of optoacoustic signals in graphene-based nanomaterials. The central hole in the phantom shown in Figure 4.18 is filled with GO, rGO, and rGO@Au, respectively, for three different measurements. Each graphene-based nanomaterial is dispersed in ethanol at the concentration of 25 mg/ml. The following parameters have been chosen for the experiments: pulse duration $T_p = 70$ ns, repetition rate $F_r = 1$ kHz, and peak current of 35 A. The absorption coefficient has been calculated by analyzing the measurements of optical power transmitted through: a) the tissue phantom alone, b) the tissue phantom filled with graphene-based solutions in a 4-mm-diameter hole, respectively, and applying the Beer-Lambert law. To measure the average incident and transmitted optical power, a power sensor (S120C from Thorlabs Inc.) has been used.

4.3.2.2.1. Characterization of phantom attenuation

A phantom is an attenuating medium mimicking a soft biological tissue in both absorption and scattering properties. The absorption and scattering coefficients μ_{abs} (cm^{-1}) and μ_{sca} (cm^{-1}) are important parameters of biological tissues that describe the light attenuation due to absorption and scattering effects,

respectively. In an optoacoustic experiment environment, the absorption coefficient depends on the combined characteristics of the chromophore and the biological tissue under study, while the scattering coefficient strongly depends on the turbidity of the biological tissue. In our case, since the total light power emitted from the three diode lasers is relatively low, a low scattering phantom with only 10% of agar-agar as scattering component has been chosen. The total attenuation coefficient of the phantom μ_{att_pha} (cm^{-1}) contains contributions from both the absorption μ_{abs_pha} and scattering μ_{sca_pha} coefficients, as follows:

$$\mu_{att\_pha} = \mu_{abs\_pha} + \mu_{sca\_pha} . \tag{4.2}$$

The attenuation coefficient of the phantom μ_{att_pha} has been calculated using the following equation:

$$\mu_{att\_pha} = \frac{-1}{d_{pha}} \ln\left(\frac{P_{pha}}{P_{direct}}\right), \tag{4.3}$$

where d_{pha} is the lateral size of the phantom (d_{pha} = 5.2 cm), P_{pha} is the average optical power transmitted through the phantom ($P_{pha} \approx 1.77 \pm 0.04$ mW), and P_{direct} is the direct power from the fiber bundle to the power sensor ($P_{direct} \approx 11.6$ mW). Assuming that the absorption coefficient of the phantom at 905 nm is $\mu_{abs\_pha} \approx 0$, since it is not an absorbing medium, $\mu_{att\_pha} \approx \mu_{sca\_pha} \approx 0.362 \pm 0.004$ cm^{-1}.

4.3.2.2.2. Characterization of graphene attenuation

The evaluation of the absorption coefficient $\mu_{abs\_graphene}$ of graphene-based solutions is a preliminary step before proceeding with the optoacoustic signal analysis. By illuminating the graphene-based solutions inside the phantom we can estimate the attenuation coefficient of the graphene/phantom compound, and consequently the absorption of graphene-based solutions. Similarly to Eq. (4.2), the total attenuation coefficient of the graphene/phantom compound $\mu_{att\_graphene/pha}$ is given by the following equation:

$$\mu_{att\_graphene/pha} = \mu_{abs\_graphene/pha} + \mu_{sca\_graphene/pha} , \tag{4.4}$$

where $\mu_{abs\_graphene/pha}$ and $\mu_{sca\_graphene/pha}$ are the absorption and scattering coefficients, respectively. Since the graphene-based solutions are poor scatterers ($\mu_{sca\_graphene} \approx 0$), we will obtain that $\mu_{sca\_graphene/pha} \approx \mu_{sca\_pha}$. In addition, since the phantom is a poor absorber ($\mu_{abs\_pha} \approx 0$), we get $\mu_{abs\_graphene/pha} \approx \mu_{abs\_graphene}$. Consequently, the total attenuation coefficient is given by the following equation:

$$\mu_{att\_graphene/pha} \approx \mu_{abs\_graphene} + \mu_{sca\_pha} , \tag{4.5}$$

Eq. 4.5 can be rewritten as:

$$\mu_{att\_graphene/pha} \approx -\ln\left(\frac{P_{graphene/pha}}{P_{direct}}\right)\left(\frac{1}{d_{graphene}} + \frac{1}{d_{pha}}\right), \tag{4.6}$$

where $P_{graphene/pha}$ is the average optical power transmitted through the phantom when the hole is filled with GO, rGO, or rGO@Au solutions, while $d_{graphene}$ = 4 mm and d_{pha}' = 4.8 cm are the diameter of the hole filled with graphene-based solution and the lateral size of the phantom material without counting the hole, respectively. Hence, we can easily calculate the absorption coefficients of the graphene-based solutions from Eq. (4.5), considering that $\mu_{sca\_pha} \approx 0.362 \pm 0.004$ cm^{-1}, as previously calculated.

Table 4.9. Average optical power transmitted through the optical phantom with the graphene-based solutions inside and the corresponding absorption coefficients at 905 nm.

Solution in phantom	Average transmitted power (μW)	Absorption coefficient (cm^{-1})
rGO@Au	22.85 ± 2.54	16.53 ± 0.31
GO	16.72 ± 2.70	17.40 ± 0.46
rGO	12.39 ± 1.18	18.18 ± 0.26

The measured average optical power transmitted through the phantom when it is filled with the graphene-based solutions and the corresponding absorption coefficients at 905 nm are shown in Table 4.9 (mean value and standard deviation). As expected, the absorption coefficient has the highest value for rGO, and the lowest value for rGO@Au. The latter result is associated with the fact that at a fixed concentration of 25 mg/ml, the rGO@Au sample contains the smallest amount of the graphene-based nanomaterial.

4.3.2.3. Results and discussion

For all the optoacoustic measurements, a pulse width of 70 ns and a repetition rate of 1 kHz (duty cycle of 0.007%) have been used. Assuming rectangular 70 ns pulses, the triplet of HPDLs provided a total pulse energy of ~11.6 μJ to the sample (average power measured at the output from the fiber bundle P_{avg} ~11.6 mW). Accordingly, the total pulse energy density was ~ 3.9 μJ/mm^2 and the total peak power delivered to the sample was ~166 W. The light beam incident on the absorbing sample generated optoacustic signals that have been detected by a 1-MHz acoustic transducer and then amplified by a 40-dB amplifier to be visualized on the oscilloscope. The calculated light spot at the focal plane had a circular area of ~1.2 mm^2, but the real spot focused on the sample was ~ 3 mm^2. Table 4.10 summarizes the characteristics of the optical pulses used for excitation of optoacoustic signals.

Table 4.10. Characteristics of optical pulses used for excitation of optoacoustic signals.

Parameter	Value
Pulse width	70 ns
Repetition frequency	1 kHz
Duty cycle	0.007%
Total pulse energy	11.6 μJ
Total average power	11.6 mW
Light spot area	3 mm^2
Total pulse energy density	3.9 μJ/mm^2
Total peak power delivered to sample	166 W (efficiency 63%)

The optoacoustic signals detected from the graphene-based solutions hosted in tissue phantoms are discussed. As specified in section 4.3.2.1, the phantoms are composed of 10% of agar-agar (as a scattering material) and 90% of neutral gelatin when a triplet of HPDLs emitting at 905 nm is applied as a light source. Figure 4.19 shows the optoacoustic signals measured for rGO@Au, GO, and rGO, respectively. Each graphene-based nanomaterial has been diluted in ethanol at the concentration of 25 mg/ml. The optoacoustic signals have been low-pass filtered using a boxcar filter. It is introduced a new parameter, i.e. the optoacoustic sensitivity (V/W), which is the ratio between the minimum optoacoustic signal over the floor noise level (referenced as 3 mV) and the minimum average optical power required to get an optoacoustic signal. In Table 4.11, the optoacoustic signal amplitude and the optoacoustic sensitivity for each graphene-based solution (mean value and standard deviation) are shown. As expected, the optoacoustic sensitivity increases in step with the absorption of the graphene-based solutions given in Table 4.9. The relatively high absorption achieved with these graphene-based solutions demonstrates that they can serve as optoacoustic contrast agents. Another interesting aspect of our study is that the HPDL system implemented in this work is capable of achieving reasonably high optoacoustic signals with relatively small light spot sizes (~ 1.2 mm^2). Therefore, it will be possible to select very small areas of biological tissues for a high-resolution OAI.

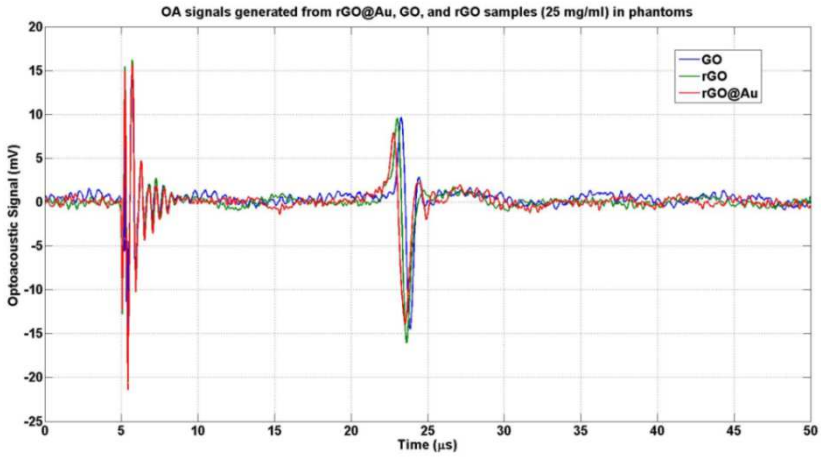

Figure 4.19. Optoacoustic signals generated respectively from rGO@Au, GO, and rGO solutions diluted in ethanol (25 mg/ml) and hosted in the hole of optical phantoms composed of 10% of agar-agar and 90% of gelatin.

Table 4.11. Optoacoustic signals (peak-to-peak) measured from the graphene-based solutions.

Solution in phantom	Optoacoustic signal (mV)	Optoacoustic sensitivity (V/W)
rGO@Au	21.8	2.49 ± 0.03
GO	24.1	2.56 ± 0.04
rGO	25.6	2.66 ± 0.05

4.3.3. Optoacoustic signals generated with gold nanorods in soft phantoms

In this section it is shown the optoacoustic response of two solutions of gold nanorods dispersed in distilled water (0.8 mg/ml) and hosted in tissue-like phantoms. Similarly to the previous sections, small arrays of HPDLs at 870 nm and 905 nm have been used as excitation sources coupled to a 7-to-1 optical

fiber bundle with core diameter of 675 μm, following the steps reported in section 4.2.2. Each solution of gold nanorods exhibits an absorption peak close to the operating wavelength, i.e. ~860 nm and ~900 nm, respectively, to optimize the generation of optoacoustic signals. The phantoms were made of agar, intralipid and hemoglobin to simulate a soft biological tissue with reduced properties of scattering. Three holes with different diameter (i.e. 1 mm, 2 mm, and 4 mm) have been done in the phantoms at different depths (i.e. 0.9 cm, 1.8 cm, and 2.7 cm) to be filled with gold nanorods. In this way, optoacoustic signals with appreciable signal-to-noise ratio (SNR) have been generated at different depths in the phantoms. The high optoacoustic response exhibited by gold nanorods suggests their application in OAS as exogenous contrast agents to detect and monitor emerging diseases like metastasis and arteriosclerotic plaques.

4.3.3.1. Absorbance characterization of gold nanorods

The absorbance spectrum of two pure solutions of gold nanorods with respective absorbance peak (O.D.=20) at ~ 860 nm and ~ 900 nm is characterized over the spectral range between 410 and 1100 nm (Fig. 4.20) by using a spectrophotometer (Lambda 14P, Perkin Elmer Inc.) and considering a path length of 1 cm in a fused quartz cuvette. The main characteristics of the gold nanorods are reported in Table 4.12. We call NP1 the gold nanorods with absorbance peak at ~ 860 nm, and NP2 the gold nanorods with absorbance peak at ~ 900 nm. The absorbance at 870 nm and 905 nm, calculated from the measured spectra (Fig. 4.20), is ~19.89 and ~19.97, respectively.

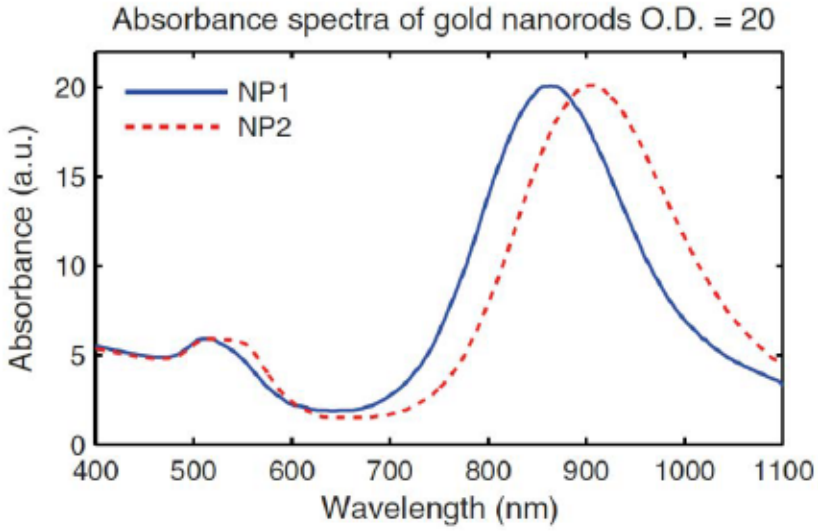

Figure 4.20. Absorbance spectra of two colloidal solutions of gold nanorods (O.D. = 20) with peak at: ~ 860 nm (blue line) and ~ 900 nm (red dots). The solutions have been diluted with a factor of 20 before measurements.

The corresponding absorption coefficients can be calculated by the following equation [152], considering that O.D. corresponds to the absorbance using a path length of 1 cm:

$$\mu_{abs}\left[\mathrm{cm}^{-1}\right] = 2.303 \times \mathrm{O.D.}, \tag{4.7}$$

which in our case are ~ 45.81 cm-1 and ~ 45.99 cm-1 at 870 nm and 905 nm, respectively.

Table 4.12. Main characteristics of the gold nanorods.

Characteristics	NP1	NP2
Width	10.8 ± 0.9 nm	11.7 ± 0.8 nm
Length	49.6 ± 3.2 nm	56.3 ± 4.2 nm
Aspect ratio	4.6	4.8
Longitudinal peak	858 nm	900 nm
Transverse peak	513 nm	516 nm
Particle concentration	1.3 x 10^{13} per ml	9.9 x 10^{13} per ml
Mass concentration (Au)	0.9 mg/mL	0.8 mg/mL

4.3.3.2. Results and discussion

For all the measurements, a pulse width of 95 ns and a repetition rate of 1 kHz (duty cycle of 0.0095 %) have been used. Assuming rectangular 95 ns pulses, the two triplets of HPDLs provided total pulse energies of ~ 12.45 μJ and ~ 12.17 μJ at 870 nm and 905 nm, respectively, to the gold nanorods solutions chosen as samples. Wide optical pulses in proximity of the maximum ratings of the HPDLs (i.e. 95 ns) have been used to optimize the energy per pulse delivered to the sample, since it is proportional to the pulse width. A higher energy per pulse contribution would mean a better optoacoustic signal generation. Table 4.13 summarizes the characteristics of the optical pulses used for excitation of optoacoustic signals.

Table 4.13. Characteristics of optical pulses used for excitation of optoacoustic signals at 870 nm and 905 nm, respectively.

Parameter	870-nm HPDLs	905-nm HPDLs
Pulse width	95 ns	95 ns
Repetition frequency	1 kHz	1 kHz
Duty cycle	0.0095%	0.0095%
Total pulse energy	12.45 μJ	12.17 μJ
Total average power	12.45 mW	12.17 mW
Light spot area	3 mm^2	3 mm^2
Total pulse energy density	4.15 μJ/mm^2	4.06 μJ/mm^2
Total peak power delivered to sample	131 W	128 W

The lens systems of Table 4.3 have been used for the measurements. The average power measured at the output of the second lens system was ~ 12.45 mW and ~ 12.17 mW at 870 nm at 905 nm, respectively. The light spot area was 3 mm^2 in both cases. Accordingly, the respective total pulse energy densities were ~ 4.15 μJ/mm^2 and ~ 4.06 μJ/mm^2, and the total peak power delivered to the sample was ~ 131 W at 870 nm and ~ 128 W at 905 nm. The alignment between the light output, the phantom, and the piezoelectric transducer is necessary to efficiently generate optoacoustic signals from the gold nanorods inclusions (Fig. 4.21). One important aspect to consider prior to optoacoustic measurements is the characterization of the optical scattering of the phantom. Table 4.14 shows the physical characteristics of the phantoms and Table 4.15 reports their scattering coefficients at 870 nm and 905 nm, calculated with Eq. (4.3).

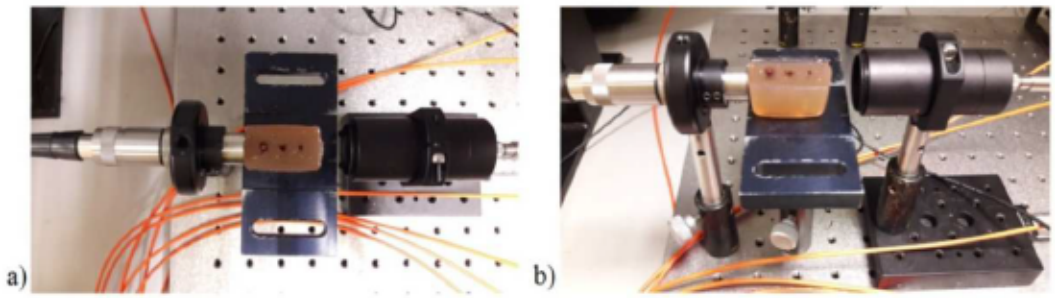

Figure 4.21. Alignment between the light output, the phantom, and the piezoelectric transducer.

In principle, the combination of multiple HPDLs improves the optoacoustic signal-to-noise ratio (SNR), following the formula:

$$SNR_T = SNR_S \times N\,, \tag{4.8}$$

where SNR_T is the total signal-to-noise ratio, SNR_S is the signal-to-noise ratio of a single HPDL, and N is the number of devices. In our case $N=3$ for each of the two wavelengths. To calculate the SNR of the optoacoustic signals detected, the following equation is used:

$$SNR_{T(dB)} = 20\log_{10}(SNR_T) = 20\log_{10}\left(\frac{\text{optoacoustic signal (mV)}}{\text{floor noise (mV)}}\right). \tag{4.9}$$

Table 4.14. Geometrical characteristics of the phantoms used in the measurements.

Characteristics	Value
Material	60 % Agar, 10 % intralipid and 30 % hemoglobin
Size (Thickness x width x height)	$2.2 \times 3.6 \times 2.2$ cm^3
Volume of the holes filled with gold nanorods	15 / 60 / 240 mm^3
Hole diameter	1 mm, 2 mm and 4 mm

Table 4.15. Scattering coefficients of the phantoms at 870 nm and 905 nm. The values are 10-100 times less than in the biological tissues [153].

Wavelength	Scattering coefficient of phantoms
870 nm	1.03 cm^{-1}
905 nm	1.18 cm^{-1}

To demonstrate the possibility of generation of detectable optoacoustic signals, three holes with different diameters (i.e. 1 mm, 2 mm, and 4 mm) done in tissue-like phantoms at different depths (0.9 cm, 1.8 cm, and 2.7 cm) have been filled with gold nanorods with absorption peak at ~ 860 nm and ~ 900 nm, respectively (see section 4.3.3.1). The phantoms have been made of agar, intralipid and hemoglobin to

mimic a soft biological tissue. Two sets of three HPDLs operating at 870 nm and 905 nm have been used as excitation sources to detect optoacoustic signals from the gold nanorods NP1 and NP2, respectively. Figure 4.22 depicts the optoacoustic signals generated from NP1 at 870 nm and the optoacoustic signals generated from NP2 at 905 nm, considering the conditions reported in Table 4.13. The amplitudes of the optoacoustic signals generated at each wavelength are reported in Table 4.16 for each inclusion and exhibit the highest amplitude with the largest inclusion. Table 4.17 shows the maximum noise amplitude at each wavelength. The signals keep an appreciable SNR (Table 4.18).

Table 4.16. Optoacoustic signals from gold nanorods in each inclusion. The inclusions are labeled with letters A, B, and C.

			Optoacoustic signal	
Inclusion	**Size**	**Depth**	**870-nm**	**905-nm**
A	4 mm	2.7 cm	57.56 mV	65.15 mV
B	2 mm	1.8 cm	32.11 mV	35.91 mV
C	1 mm	0.9 cm	24.33 mV	26.55 mV

Table 4.17. Maximum noise amplitudes detected at 870 nm and 905 nm with gold nanorods hosted in phantoms.

Wavelength	**Maximum noise amplitude**
870 nm	6.9 mV
905 nm	4.8 mV

The proposed dual-wavelength optoacoustic system based on small arrays of HPDLs is demonstrated to produce detectable optoacoustic signals from gold nanorods hosted in small phantoms by applying relatively low optical power (see Table 4.16). Since the amplitude of the optoacoustic signal is almost linearly proportional to the amount of optical power applied, by increasing the number of the emitters we should be able to detect optoacoustic signals using phantoms with higher scattering coefficient and larger size. Additionally, Eq. (4.9) would return larger values that would consent an efficient OAI. Figure 4.23 plots the amplitude of the optoacoustic signals in function of the depth (see Table 4.16 as reference) at 870 nm and 905 nm. The amplitudes of the optoacoustic signals present two slopes: between 0.9 cm and 1.8 cm of depth they exhibit a slow increase, while between 1.8 cm and 2.7 cm their intensification is significantly higher.

Table 4.18. Signal-to-noise ratio calculated for each optoacoustic signal.

	Signal-to-noise ratio from gold nanorods inclusions		
Wavelength	**Inclusion A**	**Inclusion B**	**Inclusion C**
870 nm	18.4 dB	13.4 dB	10.9 dB
905 nm	22.7 dB	17.5 dB	14.9 dB

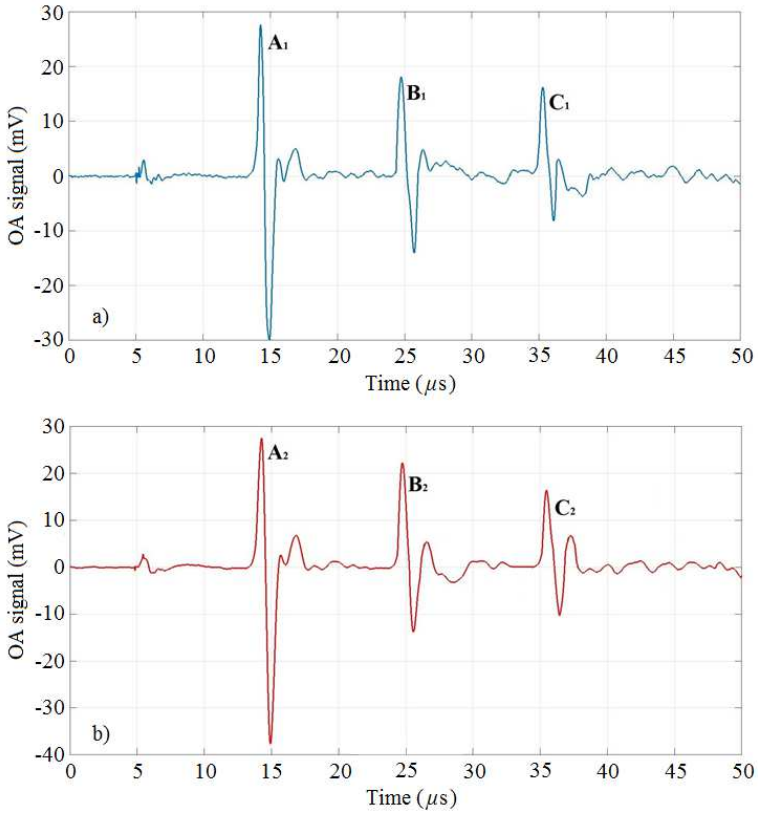

Figure 4.22. Optoacoustic signals from gold nanorods inclusions of 4-mm, 2-mm, and 1-mm diameter, respectively, hosted in the phantoms. The signals are labeled with the letters A, B, C for each case: a) NP1 at 870 nm, b) NP2 at 905 nm.

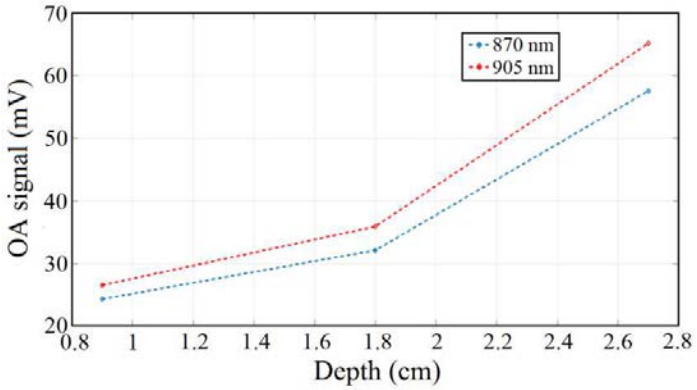

Figure 4.23. Amplitude of the optoacoustic signals at 870 nm and 905 nm in function of the depth in the phantom.

4.4. Determination of gold nanorods concentrations from optoacoustic signals detected at 870 nm, 905 nm and 972 nm with fast switching electronics

In this section is presented the final development step of our optoacoustic setup showing an application to the determination of the absolute concentrations of some mixtures of gold nanorods solutions hosted in quartz cuvette from the optoacoustic signals detected at 870 nm, 905 nm and 972 nm. Previous works

[154, 155] reported inversion algorithms to determine the single chromophores concentrations from multi-wavelength optoacoustic images acquired. Particularly, the variations in hemoglobin oxygen saturation (SO_2) in single subcutaneous vessels of rats in vivo have been investigated under three physiological states: hyperoxia, normoxia, and hypoxia. The determination of chromophore concentrations (i.e. deoxyhemoglobin and oxyhemoglobin) from skin is crucial to get information about some physiological parameters contained in the blood. Deviations from the standard values of the concentrations may indicate pathologies. Similarly, absorbing solutions of copper and nickel chloride have been submerged in a phantom at different ratios to determine their concentrations from the optoacoustic images acquired at wavelengths between 590 nm and 980 nm [154]. In the cited work, the concentrations of the single chromophores have been estimated from the imaged map of local optical energy deposition, which is roughly proportional to the amplitude of optoacoustic signals detected. In this work, optoacoustic signals are generated from mixed solutions of gold nanorods with absorption peaks at ~ 860 nm and ~ 900 nm by using in a first step two triplets of 870-nm and 905-nm HPDLs as light sources. Again, the HPDLs beams are coupled into multimode optical fibers with core diameter of 200 μm and collected in a 7-to-1 675-μm fiber bundle. A microcontroller circuit generates alternate pulses between the two wavelengths with fast switching of 0.5 ms. In a second step, a high-power DLB operating at 972 nm is added to the optoacoustic system to further validate our results. In this case, a fiber bundle with output diameter of 1.2 mm, composed of 400-μm multimode optical fibers, is used to ensure a better coupling efficiency. With the third wavelength the switching times are reduced to 0.33 ms.

4.4.1. Two-wavelengths optoacoustic system and fast switching electronics

For the experiments carried out and presented in this section, the same optoacoustic system and gold nanorods introduced in section 4.3.3 have been used, with the only difference of having a quartz cuvette as hosting medium. The measured optoacoustic signals are related to the nanoparticles concentrations by using a fluence model that is based on the approximation of the fluence distribution. It is assumed that the propagating media (i.e. the cuvette and the gold nanorods) are non-scattering media. Three mixtures of gold nanorods with different proportions have been considered: 40/60, 50/50, and 60/40. From the analysis of the optoacoustic signals detected we have been able to estimate the absolute concentrations of the gold nanorods solutions with good accuracy. In order to maximize the throughput of the system reducing the total amount of time required for a multispectral measurement, the emissions of pulses at different wavelengths have been time-division multiplexed whereas the emissions at the same wavelength have been combined. Each HPDL had its own pulse current laser driver that was activated following a sequence generated by a trigger generator. This was composed of a microcontroller (μC), a pulse generator, and a decoder (Fig. 4.24(a)). The microcontroller (pic32MX250F128B, Microchip Technology Inc., Fig. 4.25) triggered the pulse generator at some defined periods, T_{WL}, meanwhile it controlled the pulse width. Through the decoder the pulse was distributed to the laser drivers up to seven drivers following a flexible programmed sequence that can be adapted to different configurations (Fig. 4.24(b)). The HPDLs with the same emission wavelength were activated at the same time. The minimum period between wavelengths is limited by the extinction of the acoustic wave to avoid overlapping. The period of the cycle over all wavelengths, T_R, should be equal or larger than the number of wavelengths times, N, the repetition period T_{WL} ($T_R \geq N*T_{WL}$). Additionally, it cannot be lower than the minimum repetition period of the HPDLs that depends on the duty cycle (D) and the pulse width τ_p. In our implementation a repetition period of T_R = 1 ms and a pulse width τ_p of 75 ns (D = 0.0075 %) have been set with a T_{WL} of

0.5 ms, which corresponds to the switching time between the two wavelengths. The novelty of this design compared with the previous ones is represented by a fast acquisition of the optoacoustic signals by switching the two wavelengths with the microcontroller. In a real OAI environment, this switching time would facilitate the fast acquisition of high-resolution images. In our experiments, the switching times between the two wavelengths allow a fast estimation of the concentrations of the gold nanorods solutions.

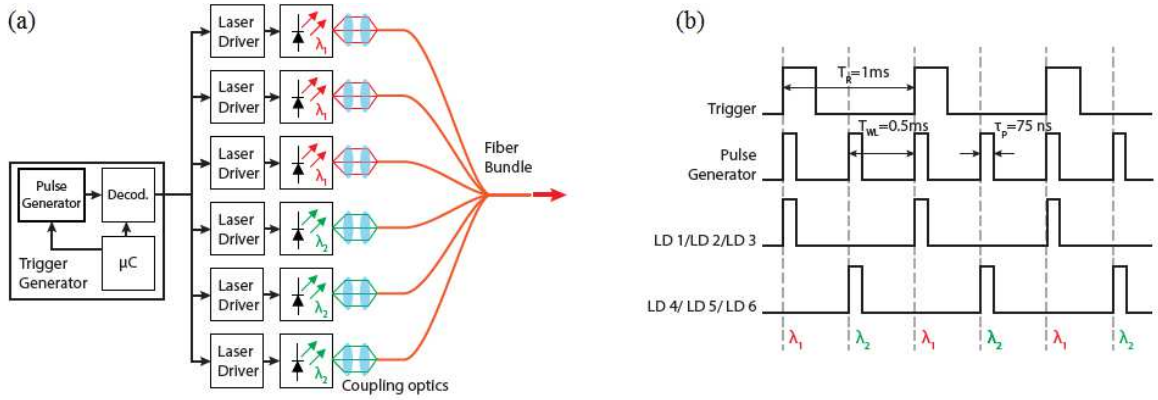

Figure 4.24. Each HPDL has its own pulse current laser driver that is activated following a sequence generated by a trigger generator: (a) block diagram of the optoacoustic system with light delivery in a fiber bundle, (b) time diagram of the trigger system that shows how the pulses are alternated between the two wavelengths λ_1 and λ_2.

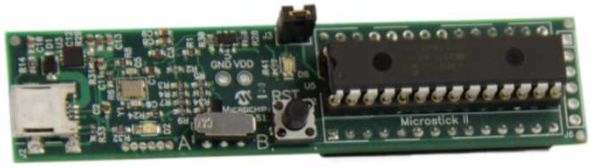

Figure 4.25. Microcontroller circuit used to control the pulse emission [156].

The beam coming out from the fiber bundle illuminated a 1-cm quartz cuvette (model Z600768-1EA, Hellma GmbH) with path length of 0.4 cm hosting the nanoparticles solutions, a 10-MHz acoustic transducer (V327-SU, Olympus Corp.), a 40-dB preamplifier, an oscilloscope, and a PC to record the optoacoustic signals (Fig. 4.26). The quartz cuvette was contained in a cuvette holder (CVH100/M, Thorlabs Inc.) with four ports, including a SMA-fiber-adapter with a collimating lens built-in and a modified port to accommodate the piezoelectric transducer. The optoacoustic signals generated have been detected by the piezoelectric transducer and then pre-amplified of 40 dB. Afterwards, they have been digitized on the oscilloscope which was synchronized with the pulse emission through the trigger generator. Finally, the optoacoustic signals have been sent to a PC for recording and filtering. Each triplet of HPDLs was triggered with the same signal obtaining a complete overlapping of the optical pulses after the output of the fiber bundle. The output of the fiber bundle has been collimated by an aspheric lens (effective focal length f_{EFL} =12 mm) with anti-reflection coating (600-1050 nm) to illuminate the sample uniformly. Distilled water has been used as a coupling agent between transducer and the wall of the cuvette. The average power measured at the output of the 12-mm lens, emitted by each triplet of HPDLs with a repetition frequency of 1 kHz and a pulse width of 75 ns, was ~ 13.56 ± 0.022 mW and ~ 13.09 ± 0.031 mW at 870 nm and 905 nm, respectively. The beam diameter was 7 mm (spot area of ~ 38.5 mm^2)

in both cases. For this reason, the 1-cm side of the cuvette has been located perpendicular to the propagation axis for the optoacoustic measurements. Accordingly, the respective total pulse energy densities are ~ 35.2 ± 0.022 μJ/cm^2 and ~ 34 ± 0.031 μJ/cm^2. Table 4.19 reports the characteristics of the optical pulses used for excitation of optoacoustic signals at 870 nm and 905 nm, respectively.

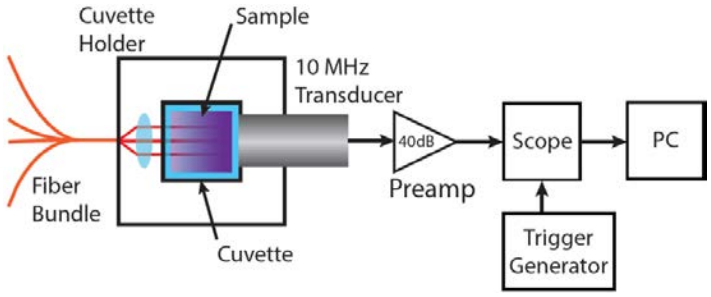

Figure 4.26. Measurement setup for the detection of optoacoustic signals.

Table 4.19. Characteristics of the optical pulses used for generating the optoacoustic signals.

Parameter	870-nm HPDLs	905-nm HPDLs
Pulse width	75 ns	75 ns
Repetition rate	1 kHz	1 kHz
Duty cycle	0.0075%	0.0075%
Total pulse energy	13.56 ± 0.022 μJ	13.09 ± 0.031 μJ
Total average power	13.56 ± 0.022 mW	13.09 ± 0.031 mW
Light spot area	38.5 mm^2	38.5 mm^2
Total pulse energy density	35.2 ± 0.06 μJ/cm^2	34 ± 0.08 μJ/cm^2
Peak power	~181 W	~175 W

The optical pulse-to-pulse stability has been checked at the output of the fiber bundle prior to experiments, showing unchanged characteristics at each wavelength in a period of 15 minutes (Fig. 4.27 (a) and (b)).

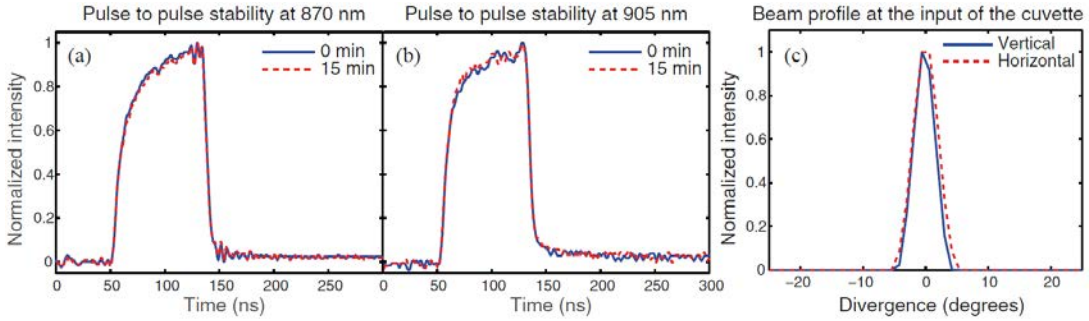

Figure 4.27. Optical pulse-to-pulse stability at: a) 870 nm, b) 905 nm. c) Beam profile at the input of the cuvette.

Figure 4.27 (c) shows the beam profile at the input of the cuvette. The uniform illumination of the sample has been achieved between vertical and horizontal axes. The absorption coefficients of the gold nanorods

(Table 4.12) at 870 nm and 905 nm, reported in Table 4.20 as well, have been calculated from the measured spectra (Fig. 4.20) using Eq. (4.7).

Table 4.20. Measured absorption coefficients at 870 nm and 905 nm.

	Absorption coefficient (cm^{-1})	
Wavelength	**NP1**	**NP2**
870 nm	~ 45.8	~ 41.7
905 nm	~ 39.6	~ 46.0

4.4.2. Determination of nanoparticles concentration optoacoustically

In [154, 155] an optical inverse problem has been proposed to estimate the concentrations C_m of M chromophores with known absorption coefficient spectra, from the 3D map of the energy absorbed in a tissue. Some parameters involved in the algorithm were considered dependent on both the wavelength λ and position vector $\boldsymbol{x}$ (i.e. total absorption coefficient, absorbed energy density, and light fluence), while the concentration was considered dependent only on the position vector $\boldsymbol{x}$, and the known absorption coefficient dependent on the wavelength λ. In our case we only consider an inverse algorithm for a 1D environment with no dependence on the position vector $\boldsymbol{x}$. Considering a homogeneous mixture of M solutions of nanoparticles with respective concentrations C_m and a set of N operating wavelengths, the total absorption coefficient $\mu_{TOT}(\lambda_n)$ (cm^{-1}) of the mixed solution is a function of the wavelength λ_n and can be expressed as:

$$\mu_{TOT}(\lambda_n) = \sum_{m=1}^{M} \mu_m(\lambda_n) C_m, \tag{4.10}$$

where $\mu_m(\lambda_n)$ is the known (from the spectra) absorption coefficient (cm^{-1}) of the reference solution of nanoparticles m at wavelength λ_n. Under thermal and stress confinement conditions and using a broadband ultrasonic transducer, the optoacoustic signal $V(\lambda_n)$ detected by the oscilloscope is proportional to the pressure $p(d, \lambda_n)$ that is related to the total absorption coefficient $\mu_{TOT}(\lambda_n)$ by the following equation:

$$V(\lambda_n) \mu\ p(d, \lambda_n) = \Gamma \mu_{TOT}(\lambda_n) \phi(d, \lambda_n), \tag{4.11}$$

where d is the depth in the sample, Γ is the Grüneisen parameter (Eq. 2.28), and the unknown fluence can be expressed as $\phi(d, \lambda_n) = A(\lambda_n) e^{-\mu_{att}(\lambda_n) d}$, where $A(\lambda_n)$ is the input pulse energy and $\mu_{att}(\lambda_n)$ is the total attenuation coefficient including both absorption and scattering effects. The exponential term will be analyzed more in details afterwards. In turn, the input energy $A(\lambda_n)$ can be related to the input average power $P(\lambda_n)$ by the relation $A(\lambda_n) = kP(\lambda_n)$, where k is a proportionality term (i.e. inverse of the pulse repetition rate). Additionally, we can define $k' = k\Gamma$. Hence, we can reformulate Eq. (4.11) as:

$$V(\lambda_n) = k' \mu_{TOT}(\lambda_n) P(\lambda_n) e^{-\mu_{att}(\lambda_n) d}. \tag{4.12}$$

Combining Equations (4.10) and (4.12) we obtain:

$$V(\lambda_n) = k' \sum_{m=1}^{M} \mu_m(\lambda_n) C_m P(\lambda_n) e^{-\mu_{att}(\lambda_n) d} \quad . \tag{4.13}$$

In Eq. (4.13) we can normalize the optoacoustic signals $V(\lambda_n)$ by the input power as $B(\lambda_n) = V(\lambda_n)/(P(\lambda_n)e^{-\mu_{att}(\lambda_n)d})$. Hence, Eq. (4.13) can be expressed in a $N\,x\,M$ matrix as follows:

$$\begin{vmatrix} B(\lambda_1) \\ B(\lambda_2) \\ \vdots \\ B(\lambda_N) \end{vmatrix} = k' \begin{bmatrix} \mu_1(\lambda_1) & \cdots & \mu_M(\lambda_1) \\ \vdots & \ddots & \vdots \\ \mu_1(\lambda_N) & \cdots & \mu_M(\lambda_N) \end{bmatrix} \begin{vmatrix} C_1 \\ C_2 \\ \vdots \\ C_M \end{vmatrix} . \tag{4.14}$$

The terms $B(\lambda_n)$ can be simplified considering just the signal amplitude that comes from the entrance of the cuvette, which means considering $\mu_{att}(\lambda_n)d \ll 1$. In this case $e^{-\mu_{att}(\lambda_n)d} \approx 1$, so the system (4.14) becomes linear. The concentrations C_m can be easily calculated inverting the matrix of absorption coefficients. This approximation presents two advantages. First, the values of $V(\lambda_n)$ can be easily found from the peak-to-peak amplitude of the first optoacoustic signal, whose redundancy occurs at some fixed delays, depending on the speed of sound in the sample. Second, it is not required an ultra-wideband ultrasonic transducer, contrary to what it is commonly used in conventional OAI. A resonant PZT transducer would behave as a band-pass filter, filtering out the lower frequencies and enhancing the optoacoustic signal that comes from the boundaries, like the first interface of the sample. In this way, the total noise present in the optoacoustic signal would be reduced, improving the sensitivity of detection.

4.4.3. Experimental validation and results at 870 nm and 905 nm

The objective of this work is to estimate the concentrations C_1 and C_2 of two solutions of gold nanorods (NP1 and NP2) mixed in a quartz cuvette from the evaluation of the optoacoustic signals detected at 870 nm and 905 nm. As anticipated in section 4.4.1, we consider three different mixtures of gold nanorods containing different percentages of the two solutions: I) 40 % NP1 and 60 % NP2, II) 50 % NP1 and 50 % NP2, III) 60 % NP1 and 40 % NP2. The optoacoustic signals are obtained from each mixture using the dual-wavelength diode laser-based system and following the experimental setup described in section 4.4.1. The optoacoustic signals detected for each mixture at 870 nm and 905 nm are depicted in Figure 4.28 after applying a boxcar filtering. In all the signals we can observe a noise around 0 µs that is generated by the coupling of the diode laser current pulse into the detector amplifier, but the optoacoustic signal is not affected because it arrives to the transducer after ~ 3 µs. For the case of two different absorbers and two wavelengths, Eq. (4.14) reduces to:

$$\begin{vmatrix} B(\lambda_1) \\ B(\lambda_2) \end{vmatrix} = \begin{bmatrix} \mu_1(\lambda_1) & \mu_2(\lambda_1) \\ \mu_1(\lambda_2) & \mu_2(\lambda_2) \end{bmatrix} \begin{vmatrix} S_1 \\ S_2 \end{vmatrix}, \tag{4.15}$$

where $S_m = k' C_m$, $\lambda_1 = 870\ nm$ and $\lambda_2 = 905\ nm$. By inverting Eq. (4.15) we find the parameters S_1 and S_2 that contain the unknown factor k'. Finally, the concentrations can be obtained as a volume

percent, knowing that the sample is a mixture exclusively of the two solutions of gold nanorods, as follows:

$$C_m(\%) = \frac{S_m}{S_1 + S_2} \times 100. \tag{4.16}$$

As it was mentioned before, the term $B(\lambda_n)$ corresponds to the peak-to-peak amplitude of the first optoacoustic pulse arriving to the ultrasonic transducer, normalized by the optical energy that reaches the cuvette at each wavelength. The quartz cuvette employed is transparent and its transmission coefficient does not vary significantly between the two wavelength considered. Thus, the optoacoustic signal is totally produced by the sample hosted inside the cuvette.

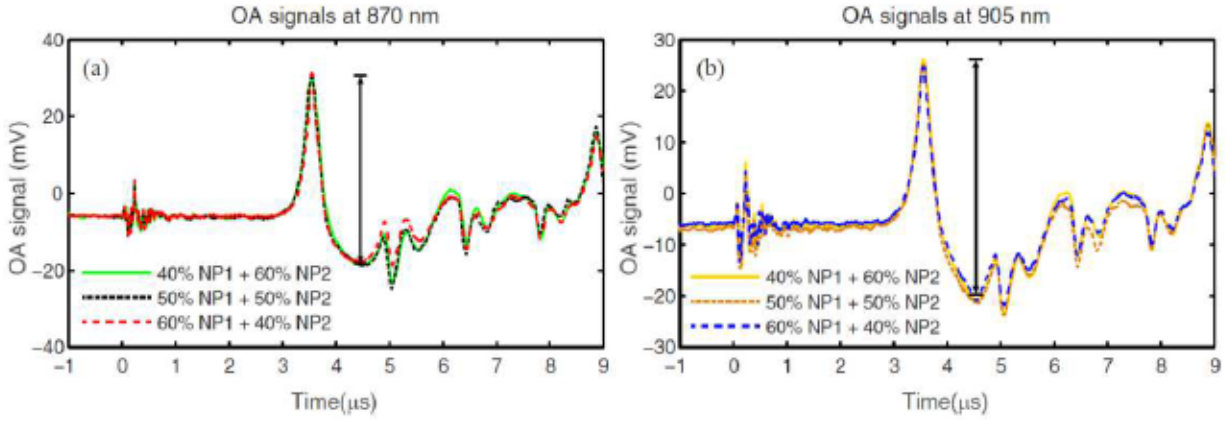

Figure 4.28. Optoacoustic signals detected from three different mixtures of gold nanorods at: a) 870 nm and b) 905 nm. For the calculation of the concentrations of gold nanorods we considered their peak-to-peak amplitudes as indicated between the first maximum and the first minimum.

The TOF required by the optoacoustic signal to reach the transducer from the cuvette-sample interface (Fig. 4.29) is given by the following equation:

$$TOF = d' v_C + d'' v_S, \tag{4.17}$$

where d' is the thickness of the cuvette wall, v_C is the speed of sound in the quartz cuvette, d'' is the thickness of the cuvette hole, and v_S is the speed of sound in the sample. Due to the acoustic impedance mismatch between the sample and the cuvette and between the cuvette and the surrounding air, a series of reverberations occurs after the arrival of the first maximum.

The detection of the optoacoustic signals mostly depends on the bandwidth of the piezoelectric transducer. To improve the accuracy of the measurements and properly detect the amplitude of the optoacoustic signals, the transducer should be wideband or at least have a central frequency high enough to avoid the overlapping of the reverberations of the optoacoustic signal in the walls of the cuvette. The quartz cuvette employed in our experiments has a wall thickness d' equal to 3 mm, so the reflections are expected every ~ 1.39 μs after the first optoacoustic signal peak, as it is shown in Figure 4.28. A transducer of 10 MHz is used to ensure that each reflection is individually resolved. Furthermore, if the transducer had a lower bandwidth (i.e. 1 MHz) the optoacoustic signal would be truncated and we would not get the correct amplitude when the absorber exhibits high absorption coefficient [155]. The peak-to-peak amplitude from the first maximum to the next minimum, measured as indicated in Figure 4.28, is

averaged over 10 measurements and is reported in Table 4.21. Taking into account the signal averaging, the total time required for the measurement of the amplitudes at both wavelengths was 10 ms. Finally, the single concentrations of the gold nanorods composing the mixtures, shown in Table 4.22, are estimated from the optoacoustic signal amplitudes reported in Table 4.21, after being normalized by the pulse energy at the corresponding wavelength (see Table 4.19), by using Eq. (4.15) and (4.16).

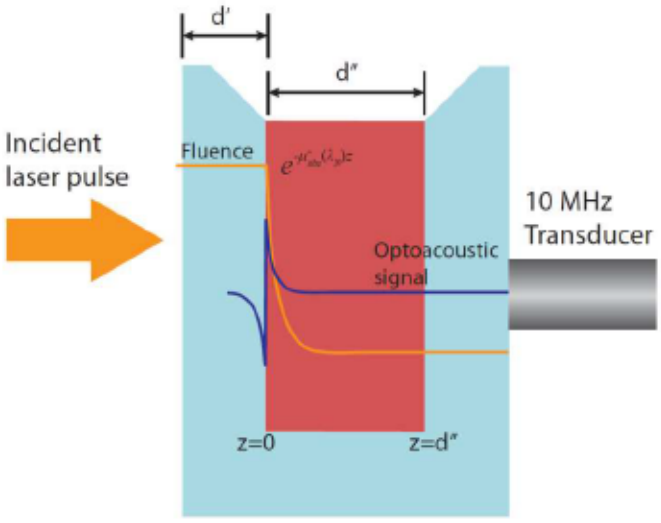

Figure 4.29. Light attenuation inside the gold nanorods hosted in a quartz cuvette and optoacoustic signal generated at the interface.

Table 4.21. Peak-to-peak optoacoustic signals at 870 nm and 905 nm after boxcar filtering in Matlab.

	Optoacoustic signal (mV)		
Wavelength	**40% NP1 60% NP2**	**50% NP1 50% NP2**	**60% NP1 40% NP2**
870 nm	48.6 ± 0.1	49.2 ± 0.1	49.9 ± 0.1
905 nm	46.8 ± 0.1	46.6 ± 0.1	46.3 ± 0.1

The error of these estimations σ_{C_n} is calculated from both the standard deviations of the normalized peak amplitudes σ_{B_n} and the inverse of the absorption coefficient matrix m_{ij}, by means of the following equation:

$$\sigma_{C_n} = \sqrt{\left(\frac{m_{21}S_1 - m_{11}S_2}{(S_1+S_2)^2}\right)^2 \sigma_{B1}^2 + \left(\frac{m_{22}S_1 - m_{12}S_2}{(S_1+S_2)^2}\right)^2 \sigma_{B2}^2}\,. \tag{4.18}$$

The calculated values of C_1 and C_2 are reported in mean value and standard deviation and present a maximum divergence of 2.76 % from the expected values. This observational error is compatible with the digitizing error of the 8-bit oscilloscope employed for measuring the signals. However, this error can be further reduced by adding more wavelengths to the optoacoustic system. In the next section it will be used a three-wavelength system that integrates a high-power DLB operating at 972 nm (central wavelength) to reduce the observational error of 2.76 %.

Table 4.22. Values of the gold nanorods concentrations estimated from the optoacoustic signals measured.

	Estimated concentrations (%)					
Nanoparticles	**40% NP1 60% NP2**		**50% NP1 50% NP2**		**60% NP1 40% NP2**	
C_1: NP1	41.97	± 1.06	48.79	± 1.05	57.24	± 1.04
C_2: NP2	58.03		51.21		42.76	

4.4.4. Three-wavelengths hybrid system and fast switching electronics

In the previous section, the absolute concentrations of two gold nanorods solutions have been estimated from the amplitudes of the optoacoustic signals detected at 870 nm and 905 nm. The results achieved showed that our dual-wavelength optoacoustic system is able to detect the absolute concentration of gold nanorods with low observational error (maximum 2.76 %) compared to the real values.

In this section, new measurements have been performed to evaluate the concentrations of the gold nanorods by adding a high-power DLB operating at 972 nm to the optoacoustic system. The spectrum of the DLB in question has been measured with a wavelength meter during the packaging process to assess the position of the maximum peak of emission. Even though the datasheet provided by the manufacturer (OSRAM Opto Semiconductors GmbH) declared a central wavelength of 980 nm (Table 5.1, section 5.5.1), the real value given by the wavelength meter was ~ 972 nm. The packaging process included the mounting of some optical elements, as shown in the simulations of section 5.5.2. The size spot measured at the output of the DLB was compatible with that reported in Figure 5.15 from simulations (~ 0.2 mm x 0.2 mm). In order to ensure an optimal beam coupling of each laser source (i.e. 870 nm, 905 nm, and 972 nm), a 1.2-mm fiber bundle composed of 400-µm multimode optical fibers has been used. Again, the combined beam illuminates different mixtures of two gold nanorods solutions with absorbance peak at ~ 860 nm and ~ 900 nm (Fig. 4.20), respectively, to generate optoacoustic signals.

The hybrid laser system was composed of two triplets of pulsed HPDLs at 870 nm and 905 nm (see section 4.2) and a 972-nm DLB (SPL BK98-20HOS, OSRAM Opto Semiconductors GmbH and packaged by DILAS Diodenlaser) combined side-by-side. The DLB was driven by a diode laser driver produced in-house. Table 4.23 summarizes the characteristics of the DLB used in the experiments.

Each laser output has been separately coupled into a 400-µm multimode optical fiber, as shown in Figure 4.30. The optical fibers are joined together forming a fiber bundle built in-house, composed of seven optical fibers disposed in hexagonal configuration and with an output diameter of 1.2-mm, as shown in Figure 4.31 (a) and (b), where each output is labeled with the corresponding wavelength. The output optical power will illuminate the solutions of gold nanorods hosted in a quartz cuvette. In order to couple the light emitted by each laser source into 400-µm multimode optical fibers, the optical lenses described in Table 4.3 have been used. Also the electronic system described in section 4.4.1 has been used. In our implementation a repetition period of T_R = 1.0 ms (repetition rate of 1 kHz) and a pulse width T_P of 75 ns (D = 0.0075%) are set for the HPDLs and 150 ns (D = 0.015%) for the DLB, and a T_{WL} of 0.33 ms, which corresponds to the switching time between the three wavelengths (Fig. 4.32).

Table 4.24 reports the characteristics of the optical pulses used for excitation of optoacoustic signals at 870 nm, 905 nm and 972 nm, respectively. The absorption coefficients of the gold nanorods NP1 and NP2 at 870 nm, 905 nm, and 972 nm, are reported in Table 4.25.

Table 4.23. Characteristics of the DLB used in the experiments. *operates in quasi-continuous wave

Characteristics	972-nm DLB*
Peak power (max)	215 W
Forward current (max)	200 A
Pulse width (max)	-
Duty cycle (max)	-
Wavelength (typ.)	972.3 nm
Aperture size	200 µm × 2 µm (25 emitters, pitch: 400 µm)
Divergence angles	61.5°, 9.5°

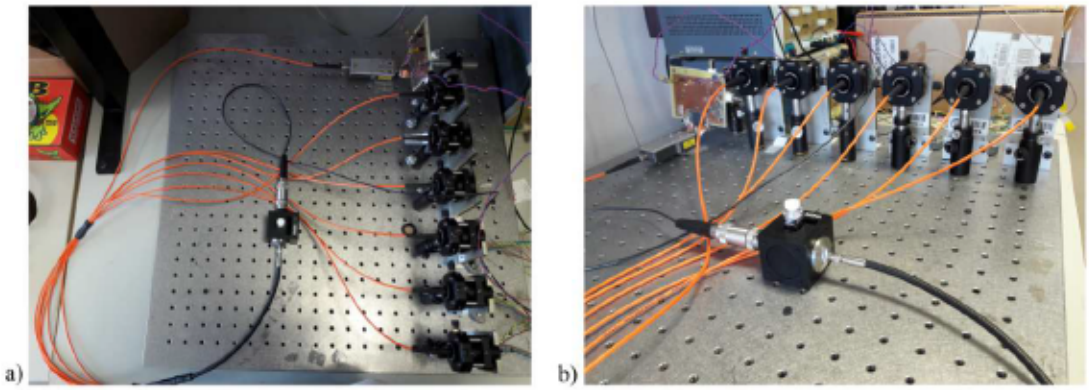

Figure 4.30. Side-by-side beam coupling of the laser sources into optical fibers. The output of the fiber bundle illuminates a quartz cuvette containing a gold nanorods solution to generate optoacoustic signals: a) top view, b) front view.

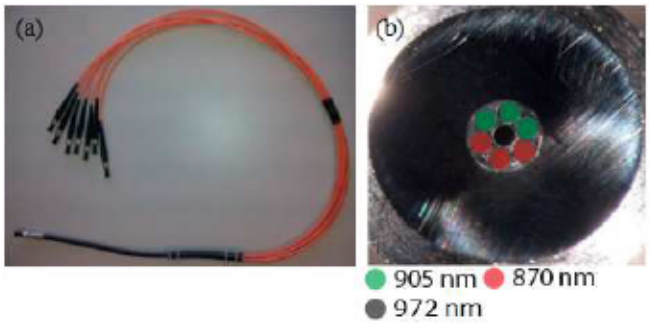

Figure 4.31. Fiber bundle with 1.2-mm diameter composed of seven 400-µm optical fibers: a) top view of the fiber bundle before being mounted, b) output of the fiber bundle seen under the microscope. The optical fibers are disposed symmetrically between 870 nm and 905 nm, with the 972 nm output at the center of the bundle to ensure uniform illumination of the sample.

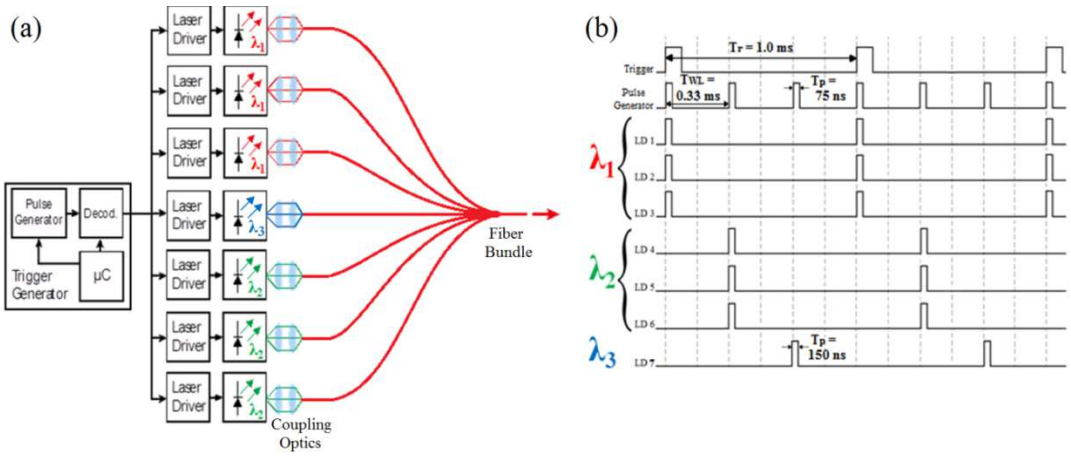

Figure 4.32. Each laser source is activated by a microcontroller: (a) block diagram of the optoacoustic system with light delivery in a fiber bundle, (b) time diagram of the trigger system that shows how the pulses are alternated between the three wavelengths λ_1, λ_2, and λ_3.

Table 4.24. Characteristics of the optical pulses used for generating the optoacoustic signals.

Parameter	870-nm HPDLs	905-nm HPDLs	972-nm DLB
Pulse width	75 ns	75 ns	150 ns
Repetition rate	1 kHz	1 kHz	1 kHz
Duty cycle	0.0075%	0.0075%	0.015%
Total pulse energy	~ 16 µJ	~ 16 µJ	~ 16 µJ
Total average power	~ 16 mW	~ 16 mW	~ 16 mW

Table 4.25. Absorption coefficients of the gold nanorods at 870 nm, 905 nm, and 972 nm.

	Absorption coefficient (cm^{-1})	
Wavelength	**NP1**	**NP2**
870 nm	~ 45.8	~ 41.7
905 nm	~ 39.6	~ 46.0
972 nm	~ 20.8	~ 33.7

The solutions of gold nanorods have been diluted in water in order to be able to measure their spectrum, since the power sensor of the spectrophotometer (Lambda 14P, Perkin Elmer Inc.) cannot detect the low optical power transmitted through the sample when its absorbance is higher than 1.

4.4.5. Experimental validation and results at 870 nm, 905 nm and 972 nm

Following section 4.4.2, an inverse algorithm is implemented to estimate the concentrations of the nanoparticles solutions from the amplitude of the optoacoustic signals. In this case, we want to estimate the concentrations C_1 and C_2 of two solutions of gold nanorods (NP1 and NP2) mixed in a quartz cuvette from the evaluation of the optoacoustic signals detected at 870 nm, 905 nm, and 972 nm.

Again, we consider three different mixtures of gold nanorods containing different percentages of the two solutions: I) 40 % NP1 and 60 % NP2, II) 50 % NP1 and 50 % NP2, III) 60 % NP1 and 40 % NP2. For the case of two different absorbers and three wavelengths, Eq. (4.14) reduces to:

$$\begin{cases} B(\lambda_1) = \left(\mu_1(\lambda_1) \times S_1 + \mu_2(\lambda_1) \times S_2\right) \\ B(\lambda_2) = \left(\mu_1(\lambda_2) \times S_1 + \mu_2(\lambda_2) \times S_2\right) \\ B(\lambda_3) = \left(\mu_1(\lambda_3) \times S_1 + \mu_2(\lambda_3) \times S_2\right) \end{cases}, \tag{4.19}$$

where $S_n = k' C_n$, λ_1 = 870 nm, λ_2 = 905 nm and λ_3 = 972 nm. Solving the linear system of Eq. (4.19), we find the parameters S_1 and S_2 dependent on the unknown factor k′. We can express the values of S_1 and S_2 by using the following equations:

$$S_1 = A_1 + A_2, \qquad S_2 = A_3 + A_4, \tag{4.20}$$

where the values of A_1, A_2, A_3, and A_4 are expressed by the following equations, respectively:

$$A_1 = \frac{B(\lambda_3)}{k' \mu_1(\lambda_3)}, \qquad A_2 = \frac{\mu_2(\lambda_3)\left(B(\lambda_2)\mu_1(\lambda_1) - B(\lambda_1)\mu_1(\lambda_2)\right)}{k' \mu_1(\lambda_3)\left(\mu_1(\lambda_2)\mu_2(\lambda_1) - \mu_1(\lambda_1)\mu_2(\lambda_2)\right)}, \tag{4.21}$$

$$A_3 = \frac{B(\lambda_3)}{k' \mu_2(\lambda_3)}, \quad A_4 = \frac{\mu_1(\lambda_3)\left(B(\lambda_2)\mu_2(\lambda_1) - B(\lambda_1)\mu_2(\lambda_2)\right)}{k' \mu_2(\lambda_3)\left(\mu_1(\lambda_1)\mu_2(\lambda_2) - \mu_1(\lambda_2)\mu_2(\lambda_1)\right)}. \tag{4.22}$$

Finally, the absolute concentrations of gold nanorods C_1 and C_2 are obtained from Eq. (4.16). The optoacoustic signals detected at 870 nm, 905 nm and 972 nm corresponding to each of the three mixtures are depicted in Fig. 4.33 (one capture) and their peak-to-peak amplitudes (mean values and standard deviations) are reported in Table 4.26 after averaging on 10 measurements and boxcar filtering in Matlab. The single concentrations C_1 and C_2 of the gold nanorods estimated from the optoacoustic signals (Table 4.27) are shown to be in good agreement with the expected values. The maximum divergence from the expected value is 1.34 %, which represents an improvement if compared to the results obtained with two wavelengths (see section 4.4.3). In a real OAS scenario, the real-time monitoring of the concentrations of gold nanoparticles at different wavelengths can be useful to know the quantity that should be administered to the patient in order to have appreciable contrast between the interested chromophores.

Table 4.26. Optoacoustic signals at 870 nm, 905 nm and 972 nm after boxcar filtering in Matlab.

	Optoacoustic signal (mV)		
Wavelength	**40% NP1 60% NP2**	**50% NP1 50% NP2**	**60% NP1 40% NP2**
870 nm	56.3 ± 0.1	56.5 ± 0.1	57.1 ± 0.1
905 nm	56.2 ± 0.1	55.4 ± 0.1	54.6 ± 0.1
972 nm	35.8 ± 0.1	39.0 ± 0.1	42.3 ± 0.1

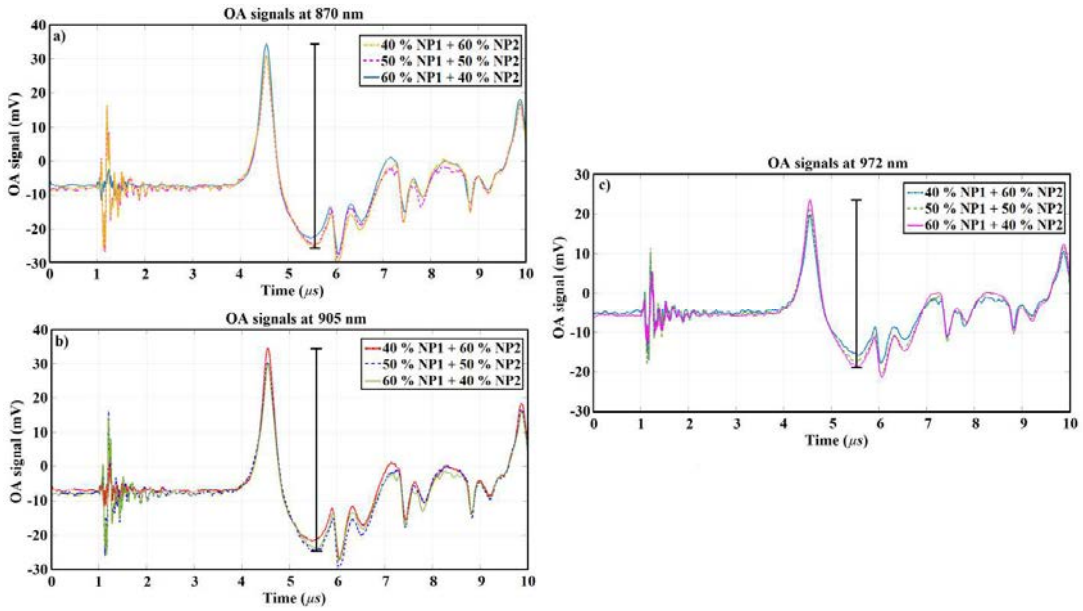

Figure 4.33. Optoacoustic signals detected from three different mixtures of gold nanorods at: a) 870 nm, b) 905 nm, and c) 972 nm. For the calculation of the concentrations of gold nanorods, the peak-to-peak amplitudes of the optoacoustic signals have been considered.

Table 4.27. Values of the gold nanorods concentrations estimated from the optoacoustic signals measured.

	Estimated concentrations (%)					
Nanoparticles	**40% NP1 60% NP2**		**50% NP1 50% NP2**		**60% NP1 40% NP2**	
C_1: NP1	40.48	± 1.11	51.34	± 0.78	60.20	± 0.58
C_2: NP2	59.52		48.66		39.80	

The gold nanorods tuned to specific wavelengths could be bio-conjugated to target some kind of cells or molecules for intravenous biomedical applications directed to the detection of diseases, such as cancer and arteriosclerotic plaques [157-160]. The gold nanorods proposed in this chapter belong to a class of nontoxic and biocompatible nanoparticles. Future research on this field would be addressed to add new NIR wavelengths to the optoacoustic systems for a more functional OAS (such as 808 nm, 880 nm, 910 nm and 940 nm). Next chapter will show a simulated multi-wavelength system based on the beam focusing and combination of high-power DLBs.

4.5. Conclusions

In this chapter, the development of an optoacoustic system based on HPDLs has been presented with some experimental results performed with several kinds of nanostructures.

Firstly, two pairs of HPDLs sources with respective emission at 870 nm and 905 nm illuminated different solutions of DWCNTs and ink hosted in tissue-like cylindrical phantoms. The optical beam emitted by the HPDLs has been collimated and focused by means of optical lenses disposed in lens tubes before illuminating the samples. It has been discussed that this optical configuration necessitates an improvement

to ensure that the samples are uniformly illuminated with synchronized pulses. For this reason, in the successive measurement stages it has been proposed and applied the beam coupling of HPDLs into optical fibers, which is also applicable for endoscopic optoacoustic applications. It has been shown and described a new light coupling scheme making use of optical fibers joined together in a custom-made fiber bundle.

In the second measurement step, the abovementioned scheme has been used to couple 905-nm pulsed HPDLs to 200-µm-core optical fibers forming a 675-µm fiber bundle. Some experimental results demonstrating an efficient optoacoustic signal generation from three graphene-based solutions (GO, rGO, and rGO@Au with respective absorption coefficients of 17.40 ± 0.46 cm^{-1}, 18.18 ± 0.26 cm^{-1}, and 16.53 ± 0.31 cm^{-1} at the concentration of 25 mg/ml) hosted in optical phantoms with small illumination areas have been shown.

Afterwards, it has been presented the optoacoustic response of different gold nanorods inclusions (size of 1 mm, 2 mm, and 4 mm, respectively) hosted at different depths (i.e. 0.9 cm, 1.8 cm, and 2.7 cm) in tissue-like phantoms exposed to laser light. These gold nanorods have been shown to exhibit absorbance peaks at different wavelengths (i.e. at ~860 nm and ~900 nm), after spectrum characterization. A dual-wavelength laser system based on small arrays of HPDLs at 870 and 905 nm has been used to generate optoacoustic signals. Results have showed that the gold nanorods inclusion with biggest size generated the highest optoacoustic signal (i.e. 57.56 mV and 65.15 mV at 870 nm and 905 nm, respectively) with significant SNR (i.e. 18.4 dB and 22.7 dB) compared to the noise level. It has been discussed that the high optoacoustic response exhibited by gold nanorods suggests their application as exogenous contrast agents in real OAS applications aimed to the detection of diseases, due to their high absorbance and biocompatibility.

Finally, the same dual-wavelength system controlled by a microcontroller circuit to alternate the pulses between the two wavelengths has been applied to generate optoacoustic signals from three different mixtures of gold nanorods containing different percentages of the two solutions: I) 40 % NP1 and 60 % NP2, II) 50 % NP1 and 50 % NP2, III) 60 % NP1 and 40 % NP2. The concentrations of these solutions have been estimated from the amplitudes of the optoacoustic signals detected. The results achieved showed that our system is able to detect the absolute concentrations of gold nanorods with low observational error (maximum 2.76 %) compared to the real values. Successively, a 972-nm DLB has been added to the system to reduce more the error to 1.34 %. It has been discussed that the real-time monitoring of the concentrations of gold nanoparticles can be useful in a real OAI scenario to know the quantity that should be administered to have appreciable contrast between the interested chromophores.

However, the optoacoustic applications necessitate a much higher amount of optical energy to penetrate in-depth in the biological tissues. Since the HPDLs can only provide a few tens of µJ, they are only suitable for OAI of small surfaces of tissue. In this way, their low optical energy can be compensated by a high fluence if the imaged surface is small. In OAI applications requiring much higher levels of optical energy, more powerful devices such as DLBs and DLSs are required. In this regard, the next chapter will present the design of a multi-wavelength optoacoustic system based on DLBs. Experiments with nanoparticles will not take part in the next chapter, because the work will be focused on the beam shaping of DLBs with optical elements. The final objective of the work presented in next chapter will be the combination and coupling of the multi-wavelength beam to a multimode 400-µm optical fiber.

Chapter 5

Design of a multi-wavelength diode laser bar system for optoacoustic applications

5.1. Introduction

The requirements of high power to penetrate deeply into biological tissues can be fulfilled using micro-fabricated arrays of diode laser cavities emitting several hundreds of peak power.
The arrays of HPDLs treated in the previous section can be reduced in size and cost by using diode laser bars (DLBs) or stacks (DLSs) that can provide the amount of optical peak power (and consequently energy per pulse) desired for biomedical optoacoustic applications.
DLBs are high-power semiconductor lasers arranged as a one-dimensional array of broad-area emitters. They typically contain between 20 and 60 emitters with variable width (100-200 μm). A typical DLB device has a resonator length of the order of ~1 mm, an overall width of ~10 mm and generates tens of Watts, or even up to several hundreds (possibly with a reduced lifetime), of optical power, but with poor beam quality due to the waveguide properties of the active regions of the emitters.
In fact, a potentially disturbing property of DLBs is the "smile", namely the horizontal line connecting the emitters. DLB modules are widely used in many fields such as sensing, ranging, direct material processing, high-power solid-state and fiber laser pumping, and biomedical applications. In these applications, one of the requirements is to deliver the smallest beam spot to a certain distance with high power density. A non-ideal property of DLBs is the asymmetric emission pattern (Fig. 5.1), which is responsible for poor beam quality. In the "fast axis" direction, the emission comes from a very narrow region, so that the beam quality is not far from diffraction limit, i.e. M^2 factor not far above 1 [161], despite the strong beam divergence angle of typically 40–70° at $1/e^2$ of the maximum amplitude. On the other hand, the "slow axis" direction has a very wide emitting region, so that despite the much smaller divergence angle (in the order of 8–15° at $1/e^2$), the beam quality is very poor with a M^2 factor > 1000. Beam shaping and optical design are therefore essential for conditioning the output of a DLB. The large NA of typically $\sim 0.6 \div 0.9$ in the fast axis requires high-NA aspherical cylindrical lenses for beam collimation while preserving the beam quality. Aspherical cylindrical micro-lenses like fast axis collimating (FAC) and arrays of slow axis collimating (SAC) lenses, or other equivalent elements, are often used for this purpose. When beams with approximately circular beam spot and reasonable beam quality are required, a special beam shaper for symmetrization of the beam quality should be applied. In this regard, an optical element that in the successive section will reveal its great potential in beam shaping is the beam twister, consisting of a 45°-tilted array of cylindrical lenses. The additional use of focusing lenses can be employed to focus the combined beam into an optical fiber for optoacoustic applications (see Chapter 4). The mean reason of using diode laser arrays instead of simply making a very broad emitting area is that the latter would suffer from amplified spontaneous emission or parasitic

lasing in the transverse direction. Additionally, the resulting broader emission area would be responsible for a much larger spectrum of propagating modes. The most important design parameters of DLBs are the number of emitters, their width and spacing. With respect to beam quality and brightness, it would be ideal to get the output power from a small number of closely spaced emitters, increasing the so-called "fill-factor", namely the ratio between the single emitter width and the pitch between two adjacent emitters. However, the optical intensity at the output facets is limited by the risk of catastrophic optical damage of the mirror coatings. In addition, closely spaced emitters may be too difficult to cool.

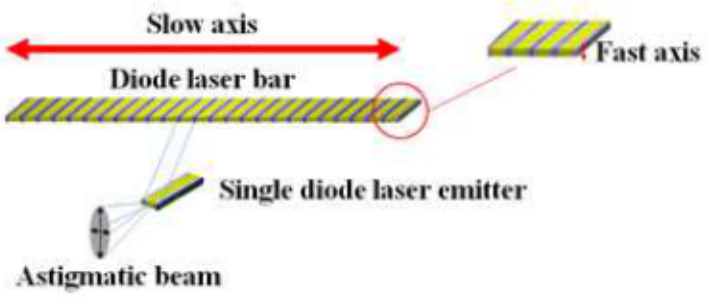

Figure 5.1. DLB emitting an astigmatic beam from each single emitter [162].

Most DLBs operate in the wavelength region from 780 nm to 980 nm, with the wavelengths of 808 nm (for pumping neodymium lasers), 940 nm (for pumping Yb:YAG) and 980 nm (for pumping erbium-doped or ytterbium-doped amplifiers) being most prominent. Our purpose is to design a multi-wavelength optoacoustic system based on DLBs, whose beam are combined and focused into a multi-mode optical fiber. Prior to the design, we should take into account several parameters that describe the beam quality.

5.2. Beam quality of diode laser bars

Beam quality is a measure of how tightly a beam can be focused. The higher is the beam quality, the smaller is the spot size and the higher is the light intensity. According to the ISO-standard [163], this property can be characterized by the beam-parameter product (Q or BPP), multiplying the waist radius (w_0) by the half-angle divergence (θ_{0half}) of the beam [164, 165]. In the best case (i.e. without any aberrations), this beam-parameter product remains constant if the beam is transformed by passive optical components such as lenses or mirrors (Eq. 5.1). The minimum value for the BPP is the so-called diffraction limit and is given by λ/π, where λ is the beam wavelength. The BPP normalized to this minimum value is called the "diffraction limited factor" (M^2) (Eq. 5.2), as it directly indicates how far away the quality of a beam is from diffraction limit. The BPP and the M^2 factor can be calculated by the following equations [165]:

$$Q = BPP = w_0 \times \theta_{0half}, \tag{5.1}$$

$$M^2 = \frac{BPP}{\lambda/\pi} = \frac{w_0 \times \theta_{0half}}{\lambda/\pi}. \tag{5.2}$$

For a given NA of the focusing system (NA_f) and a rotationally symmetric beam with a total power of P,

the average light intensity in the focal plane (I_f) is given by [165]:

$$I_f = \frac{P \times NA_f^2}{\pi} \times \frac{1}{BPP^2} = \pi \times NA_f^2 \times B\,, \tag{5.3}$$

where $B = P/(\pi^2 \times BPP^2)$. Besides the *BPP* and the M^2 factor, the parameter *B* describes the brightness of a beam and is introduced into Eq. (5.3) as an abbreviation. Equation (5.3) is widely used in many applications of conventional lasers with a single coherent and circular symmetric beam. Considering a beam consisting of *k* individual beams, the beam-parameter product (or beam quality) BPP_{tot} of the total beam is then *k* times the beam-parameter-product of the individual beam *BPP* [165]:

$$BPP_{tot} = w_{tot} \times \theta_{tot} \cong k \times w_0 \times \theta_{0half} = k \times BPP\,. \tag{5.4}$$

For a general case of two-dimensional array of $N_x \times N_y$ emitters (i.e. a diode laser stack (DLS)), the total beam quality can be easily calculated separately for each dimension (Fig. 5.2) using Eq. (5.4).

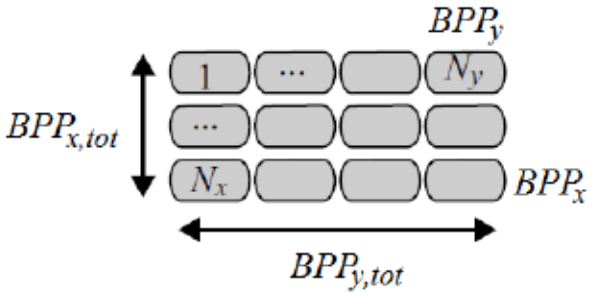

Figure 5.2. *BPPs* in a two-dimensional array of emitters [165].

In the case of one-dimensional array of N_y emitters (a DLB), $BPP_{x,tot} = BPP_x$, and the sketch of Figure 5.2 can be rearranged as shown in Figure 5.3.

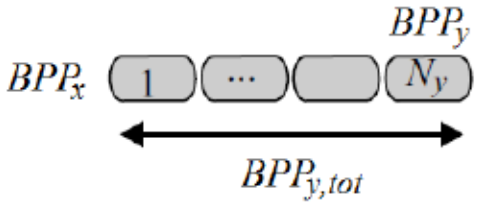

Figure 5.3. *BPP* in a two-dimensional array of emitters (reprinted from [165]).

Equation (5.4) is very useful for the calculation of beam rearrangement, as shown in Figure 5.4. A line-shaped beam with different *BPPs* in the two orthogonal directions $\left(BPP_x, BPP_y\right)$, as in DLBs, can be transformed into a beam with quadratic cross-section by cutting the line-shaped beam into separate segments and subsequent optical rearrangement of the individual beam segments.

The resulting *BPP* of the equivalent rectangular-symmetric beam BPP_{xy} is given by [165]:

$$BPP_{xy} = BPP_x \times N = BPP_y / N \,, \tag{5.5}$$

where the optimum number N of beam divisions can be expressed as the square root of the initial *BPP* ratio [165]:

$$N = \sqrt{BPP_y / BPP_x} \,. \tag{5.6}$$

Consequently, the resulting *BPP* of the equivalent rectangular-symmetric beam BPP_{xy} is given by the following equation [165]:

$$BPP_{xy} = BPP_x \times \sqrt{BPP_y / BPP_x} = \sqrt{BPP_x \times BPP_y} \,. \tag{5.7}$$

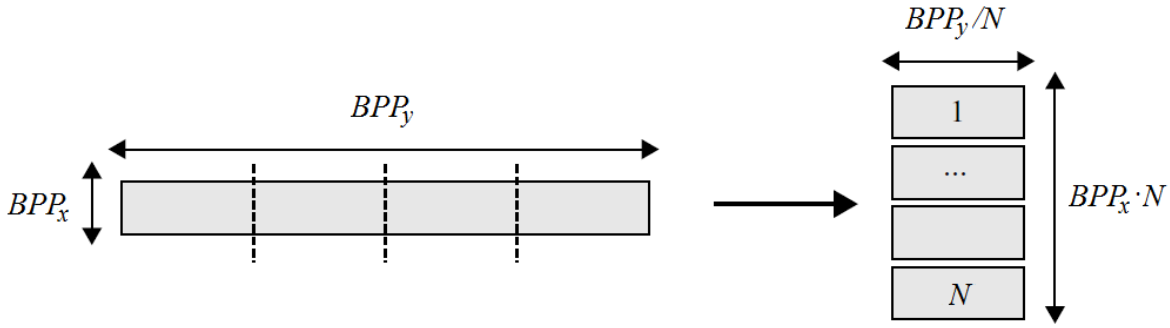

Figure 5.4. Rearrangement of the beam [165].

The total brightness of a system is not influenced by beam division and rearrangement [165].

5.3. Theory of symmetrization

As described in the previous section, the beam profile of a single diode laser bar (DLB) is highly asymmetric between slow and fast axes. However, for many applications it is required a symmetric beam in terms of adapted beam-parameter products (*BPPs*) between the two axes. A symmetric spot is also required for many applications, such as material processing and optoacoustics. Furthermore, a symmetric *BPP* is necessary for efficient fiber coupling. The basic idea of beam symmetrization by means of a beam rearrangement process has already been described in the previous section.

In this section, the concept of beam symmetrization will be explained in more details, especially in the context of fiber coupling efficiency. The basic principle is illustrated in Figure 5.5. The left part of Figure 5.5 schematically shows the asymmetry of a diode laser system in terms of beam parameter product Q or *BPP*. For a single DLB, the ratio BPP_y / BPP_x is normally about 500:1, or even more, as we will see in section 5.4. The beam quality of the whole system before beam symmetrization can be described by an overall *BPP* referred to as $BPP_{tot,rms}$, which is defined by both the root mean square value and the geometric mean of BPP_x and BPP_y, in according to the following equations [165]:

$$BPP_{tot,rms} = \sqrt{BPP_x^2 + BPP_y^2} \,, \qquad BPP_{tot,geom} = \sqrt{BPP_x \times BPP_y} \,. \tag{5.8}$$

After beam symmetrization, the *BPP* in the slow axis (BPP_y) is divided into N subsections, while the *BPP* in the fast axis (BPP_x) is multiplied by N, as expressed by the following equations [165]:

$$BPP_y^{'} = \frac{BPP_y}{N}, \tag{5.9}$$

$$BPP_x^{'} = BPP_x \times N. \tag{5.10}$$

Then, the beam quality of the whole system after beam symmetrization $BPP_{tot,rms}^{'}$ can be defined by the following equations [165]:

$$BPP_{tot,rms}^{'} = \sqrt{BPP_x^{'2} + BPP_y^{'2}}, \qquad BPP_{tot,geom}^{'} = \sqrt{BPP_x^{'} \times BPP_y^{'}}. \tag{5.11}$$

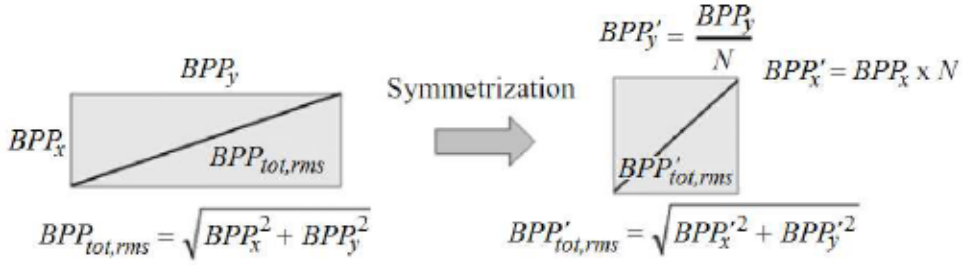

$$\text{Min}\,(BPP'_{tot,rms}) \Leftrightarrow N = \sqrt{\frac{BPP_y'}{BPP_x'}} = 1 \;\Rightarrow\; BPP_y' = BPP_x' \;\Rightarrow\; BPP'_{tot,rms} = \sqrt{2} \cdot BPP_x' = \sqrt{2} \cdot BPP'_{tot,geom}$$

Figure 5.5. Basic principle of beam symmetrization of a diode laser system. The different *BPPs* are adapted by shifting the beam quality from one axis to the other axis [165].

The beam symmetrization is realized by shifting the beam quality from the axis with higher *BPP* to the axis with lower *BPP*, so that the *BPPs* in the two axes are finally equal. The beam symmetrization is equivalent to a minimization of the overall *BPP* (i.e. of the parameter $BPP_{tot,rms}^{'}$) that is achieved if $BPP_y^{'} = BPP_x^{'}$, as described by the following equation [165], considering Eq. (5.11):

$$\text{Min}\left(BPP_{tot,rms}^{'}\right) = \sqrt{2} \times BPP_x^{'} = \sqrt{2} \times BPP_{tot,geom}^{'}. \tag{5.12}$$

Efficient fiber coupling requires a beam with an appropriate symmetrized beam quality between fast and slow axes. The upper limit for the necessary *BPP* can be defined by the diameter d and the NA of the optical fiber ($BPP_{fiber} \approx d/2$). A simple geometrical consideration shows that the value $BPP_{tot,rms}^{'}$ of the total *BPP* should not exceed the value BPP_{fiber}, as expressed by the following equation [165]:

$$BPP_{tot,rms}^{'} \le BPP_{fiber} \approx \frac{d}{2} \times NA. \tag{5.13}$$

The concept of Eq. (5.13) is clarified in Figure 5.6.

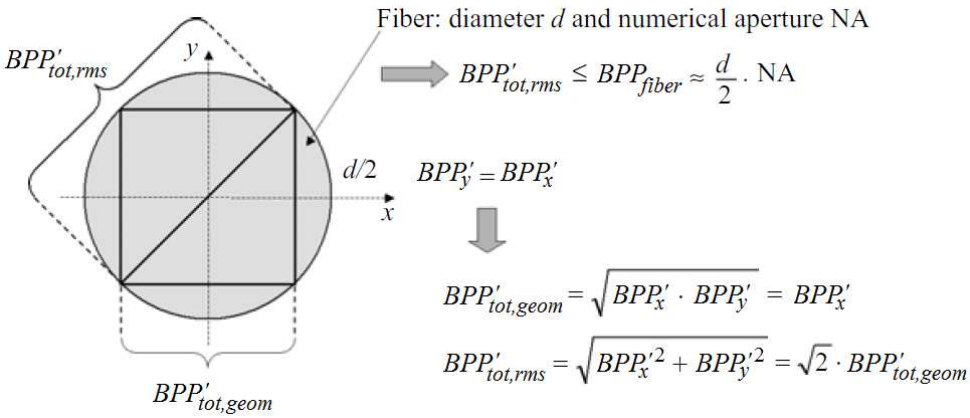

Figure 5.6. The value of $BPP'_{tot,rms}$ should be lower or equal than the value of BPP_{fiber} acceptable by the optical fiber (reprinted from [165]).

5.4. Key elements for beam symmetrization

The highly asymmetric beam profile of a DLB between slow and fast axes needs a proper shaping for an efficient fiber coupling. The most important optical elements for the beam shaping of DLBs are the FAC lens and the beam twister (BTS). The FAC lens is used to reduce the large beam divergence in the fast axis, while the BTS rotates the beam by 90°. When the beam is emitted from a DLB, it appears in a line shape that is synonymous of poor beam quality. After passing through a BTS, the rotation by 90° transforms the beam into a nearly-square shape. This new shape is more advantageous than a line because it allows the beam to be focused in a spot for fiber coupling. More specifically, after the fast axis collimation, the beam propagates into the BTS that consists of an array of biconvex cylindrical lenses that are twisted by 45° around the optical axis. The beam collimated by the FAC lens and incident on the BTS forms an angle of - 45° with the input facet of the BTS and after the internal focusing the beam is rotated + 45° from the output facet. This means that the BTS rotates the beam by 90° around the optical axis. In this way, the horizontal and vertical components (beam size and divergence angle) are interchanged and the beams of the single emitters look like stacked on each other [166]. The beam projected by the BTS is still slightly divergent in both axes (~ 2° and ~ 10°, respectively), but this time the divergence can be easily corrected by using an additional collimation lens. Figure 5.7 shows the ray tracing inside the FAC lens and the BTS, following the abovementioned description.

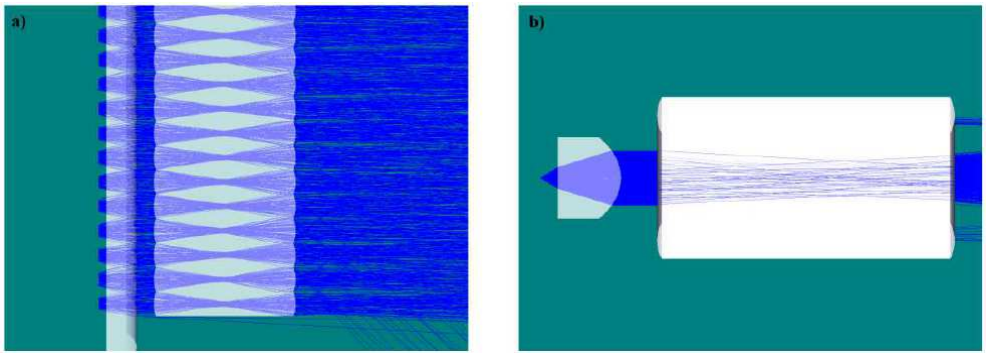

Figure 5.7. Ray tracing simulated in a FAC lens and a BTS: a) top view, b) side view. First, the FAC lens collimates the large beam divergence in the fast axis, and then the BTS rotates the beam by 90° after an internal focusing. In this way, the effect will be a superposition of beams in a nearly-square shape.

The schematic diagram of a single lens element of a BTS with refractive index n is depicted in Figure 5.8. The radii of curvature and the lens thickness maintain the relationships $r_1 = -r_2$ and $d = 2f$, respectively, where f is the focal length of the lens. The focal point F is located in the middle of the lens.

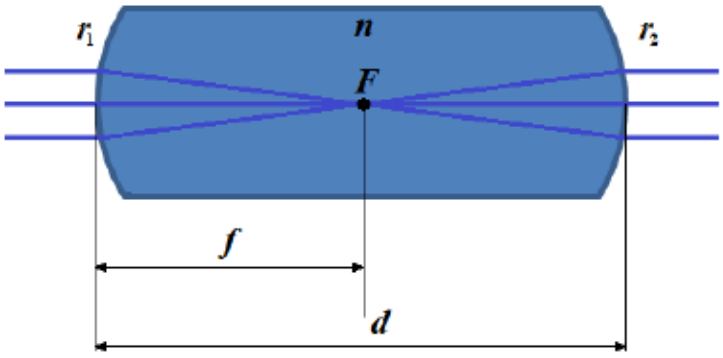

Figure 5.8. Schematic diagram of a single lens element of a BTS.

The beam profiles projected by a BTS after two different distances are depicted in Figure 5.9. Moving away from the BTS, the beam assumes more and more a rectangular or nearly-square shape with a reduced *BPP* ratio between fast and slow axes. In this way, the beam can be more easily collimated and then focused by using additional cylindrical lenses.

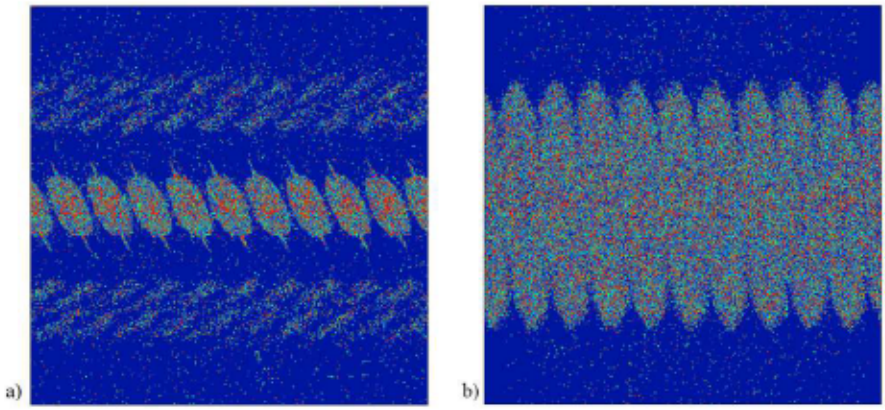

Figure 5.9. Beam profiles projected by a BTS: a) immediately after the BTS, b) after some distance before being collimated by additional cylindrical lenses.

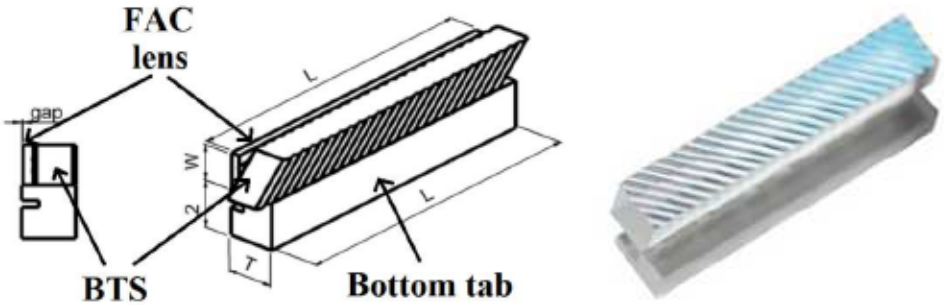

Figure 5.10. a) Sketch of FAC-BTS block [167], b) real piece [168].

Normally, the FAC lens and the BTS available in the market are preassembled in a single block, as illustrated in Figure 5.10. The overall optical losses introduced by these lenses normally not exceed 5 % of the power emitted. As previously mentioned, one essential parameter to estimate the beam quality is the *BPP* in both fast and slow axes. In fast axis, it is defined as the product of the waist radius w_{0x} (i.e. the half of the vertical size in fast axis; in DLBs it is normally $w_{0x} = 1$ μm) with the half angle divergence $\theta_{\perp half}$ of the beam along the fast axis. Instead, in the slow axis it corresponds to the product of the waist radius w_{0y} (i.e. the half of the emitter width of the DLB in slow axis (see Table 5.1, section 5.5)) with the half angle divergence $\theta_{//half}$ of the beam along the slow axis and the number of emitters, normalized to the bar fill factor. Hence, the *BPPs* in fast axis and slow axis (BPP_x and BPP_y) are respectively expressed by:

$$BPP_x = w_{0x} \times \theta_{\perp half}, \tag{5.14}$$

$$BPP_y = \frac{w_{0y} \times \theta_{//half} \times \text{number of emitters}}{\text{bar fill factor}}, \tag{5.15}$$

where the bar fill factor is normally expressed in % and is the ratio between the emitter width and the emitter pitch (Table 5.1, section 5.5). Eq. (5.14) and (5.15) correspond to Eq. (5.1) and (5.4), respectively. In order to achieve the necessary beam quality for an efficient fiber coupling, the *BPP* ratio (BPP_y/BPP_x) should be made as close as possible to 1 by means of beam shaping lenses. The BTS approaches this situation by cutting the line shape of the beam into individual segments that are optically rearranged, so that BPP_x is increased many times as the BPP_y is decreased. In this way, the *BPPs* are adapted by shifting the beam quality from one axis to the other one. In an ideal situation, the *BPPs* in the two axes would be equal, but actually there is still a small difference. However, the total light intensity is not affected by the beam rearrangement performed by the BTS, except from some spurious diffraction effects from the lenslets that are responsible only of low power losses. After the BTS, the *BPPs* are inverted and can be described by the following expressions:

$$BPP_x^{'} = \frac{w_{0x} \times \theta_{\perp half} \times \text{number of emitters}}{\text{bar fill factor}}, \tag{5.16}$$

$$BPP_y^{'} = w_{0y} \times \theta_{//half}. \tag{5.17}$$

For instance, considering a 910-nm DLB (Table 5.1, section 5.5), the BPP ratios before and after the BTS are $BPP_y / BPP_x \approx 772$ and $BPP_x^{'} / BPP_y^{'} \approx 3.2$, respectively. This value is greater than 1, but is sufficient to reach the beam coupling with high efficiency (> 60 %) into an optical fiber by using additional lenses. Normally, the BTS cannot reduce the *BPP* ratio to 1, being an ideal situation.
The optimum number *N* of beam divisions is thus equivalent to the following expression:

$$N = \sqrt{BPP_y / BPP_x}. \tag{5.18}$$

In addition, Eq. (5.9) and (5.10) can be rearranged as follows to find the real number of beam divisions, called N_{real}:

$$BPP_x^{'} = \frac{BPP_y}{N_{real}}, \tag{5.19}$$

$$BPP_y^{'} = BPP_x \times N_{real}. \tag{5.20}$$

In the case of a 910-nm DLB, the optimum value of *N* to get a *BPP* ratio of 1 should be ~ 27.8 (Eq. (5.18)), while the value of N_{real} is ~ 15.45 (Eq. (5.19) and (5.20)).

5.5. Multi-wavelength optoacoustic system based on high-power DLBs

Multi-wavelength laser sources are necessary for a functional OAS. The use of HPDLs has aroused great interest for their relatively low costs and small sizes if compared to solid state lasers. However, HPDLs are only available at few wavelengths and can deliver low optical energy (normally in the order of μJ), while DLBs offer more wavelengths in the market and can deliver more optical energy.
In this section, the simulations of optical systems for beam coupling of single high-power DLBs into 400-μm optical fibers will be shown. These systems operating at different wavelengths in the near-infrared spectrum (i.e. 808 nm, 880 nm, 910 nm, 940 nm, and 980 nm) have been simulated by the software Zemax. Then, in a separate design, the beams of the DLBs are combined in a compact system making use of dichroic mirrors and focusing lenses for beam coupling into a 400-μm optical fiber.
Commercially available DLBs with low (< 50 %) and high fill factor (> 50 %) are simulated. The beam of low fill-factor DLBs has been straightforwardly collimated, 90º-rotated and focused by means of FAC lenses, BTSs with pitch of 400 μm, and additional cylindrical lenses that are also commercially available [169]. However, the market does not offer BTSs with suitable pitch for the high-fill factor bars. Typically, we can find BTSs with 400-μm or 500-μm pitch. High fill-factor bars are particularly interesting for their high optical peak power (≥ 300 W). For the low fill-factor DLBs, the achieved spots have square shape with size of ~ 0.2 mm x 0.2 mm and are coupled into 400-μm optical fibers. For the case of high fill-factor DLBs it is firstly shown an alternative design for beam focusing in ~ 2.8 mm x 2.7 mm spot. This relatively large size would not permit good coupling into optical fibers with small diameter (< 1 mm), but it can be suitable for potential optoacoustic applications in free space. In a second step, for high fill-factor DLBs the same scheme used for low fill-factor DLBs by means of BTSs with pitch of 400 μm is simulated, and also in this case it is demonstrated an effective beam focusing into 400-μm optical fibers. The coupling efficiencies achieved are between ~ 76.3 % and ~ 78.8 %. Finally, in a separate design all the DLBs sources are joined in a compact design making use of dichroic mirrors, a polarizing beamsplitter cube (PBS) and focusing lenses for beam coupling into a 400-μm optical fiber. In this case, the coupling efficiency achieved is ~ 67.9 %.

5.5.1. Theory and method

Some optoacoustic applications like OAE require laser light coupling into optical fibers at different wavelengths. The aim of the following work is to develop a multi-spectral optoacoustic system based on the beam coupling of several near-infrared high power DLBs into 400-μm optical fibers with N.A. of

0.22. In a real implementation, the optical fibers would be collected in a fiber bundle for multi-spectral OAI. Figure 5.11 reports a sketch of this design for a real optoacoustic implementation. The beams are first collimated and then coupled into optical fibers, which are assembled in a fiber bundle.

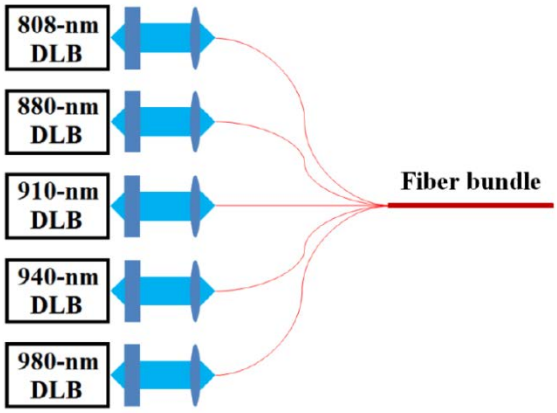

Figure 5.11. Sketch of a multi-wavelength DLBs-based assembly coupled into a fiber bundle.

The DLBs are classified by their fill factor. DLBs of 808 nm, 880 nm, and 940 nm (*Jenoptik*) have high fill-factor, while the DLBs of 910 nm and 980 nm (*Osram*) have low fill-factor. The main characteristics of the DLBs are summarized in Table 5.1.

Table 5.1. Main characteristics of high-power DLBs emitting at 808 nm, 880 nm, 940 nm (*Jenoptik**), 910 nm, and 980 nm (*Osram***). *Quasi-continuous wave**

Characteristic	Value				
Central wavelength (nm)	808***	880***	910**	940***	980**
Regime	QCW*	QCW*	QCW*	QCW*	QCW*
Output peak power (typical) (W)	300	500	120	300	120
Fast axis beam divergence ($1/e^2$) (degrees)	66.5 ± 1.5	49 ± 1	61.5 ± 2.5	47.5 ± 1.5	61.5 ± 2.5
Slow axis beam divergence ($1/e^2$) (degrees)	10.5 ± 0.5	13 ± 2	9.5 ± 1.5	10 ± 1	9.5 ± 1.5
Single emitter contact width (μm)	100	190	200	190	200
Emitter pitch (μm)	150	250	400	250	400
Number of emitters	62	37	25	37	25
Fill factor (%)	67	76	50	76	50

5.5.2. Simulations and results

The beam shaping of low fill-factor DLBs and then of high fill-factor DLBs are investigated. All the sources are modeled in Zemax with their real sizes (Table 5.1), considering an emitter height of 2 μm. Also the lenses are taken from catalogues and are modelled with their real characteristics. Figure 5.12

shows the implementation in Zemax of a DLB with the lenses and the optical fiber, as it appears in the "Non-Sequential Component Editor" in Zemax. This design required a simulation in non-sequential mode, where all the objects are modelled in a 3D space. Object 1 represents the array of emitters constituting the DLB; object 2 the FAC lens; objects 3 and 4 the array of bi-convex cylindrical lenses constituting the BTS; objects 5-7 the collimation and focusing lenses; objects 8 and 9 the optical fiber core and cladding; finally, objects 10 and 11 represent the light detectors placed before and after the optical fiber, respectively.

	Object Type	Comment	Y Position	Z Position		Tilt About Z	Material	Radial Height	X Half-Width	Thickness	Radius1	Radius2	
1	Source Tw..		-4.800	0.000		90.000	-	30	10000	4.800	1.000E-003		
2	Toroidal ..	FAC	0.000	0.094	V	90.000	S-TIH53	0.225	5.500	0.354	0.000	-0.235	
3	Toroidal ..	BT	-4.800	0.648		45.000	S-TIH53	0.141	0.490	1.659	0.380	-0.380	P
4	Array		-4.800	0.648	P	90.000	-	3	25	1	1.000	0.000	
5	Toroidal ..		0.000	14.675		90.000	S-TIH53	3.000	7.000	2.000	0.000	-11.360	
6	Toroidal ..		0.000	23.475	P	0.000	S-TIH53	7.000	3.500	2.000	22.190	0.000	
7	Toroidal ..		0.000	37.325	P	90.000	S-TIH53	3.000	7.000	2.000	11.488	0.000	
8	Cylinder ..		0.000	52.248		0.000	1.46,0.0	0.200	10.000	0.200			
9	Cylinder ..		0.000	52.248	P	0.000	1.44,0.0	0.220	10.000	0.220			
10	Detector ..	D1	0.000	52.238	P	0.000		2.000	2.000	512	0	0	
11	Detector ..	D2	0.000	62.348	P	0.000		2.000	2.000	512	0	0	

Figure 5.12. Screenshot of the Non-Sequential Component Editor in Zemax showing the implementation of a DLB with the optical elements.

5.5.2.1. Low fill-factor DLBs

Two additional cylindrical lenses with back focal length of 25.15 mm and 12.50 mm, respectively, are used for beam focusing in each axis and positioned so that their focal points coincide. Figure 5.13 shows the Zemax design in both top and side views.

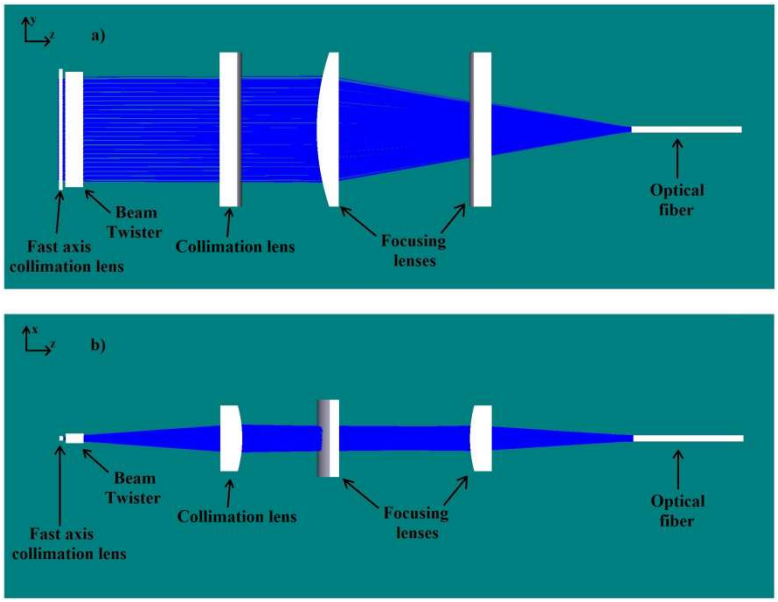

Figure 5.13. Design for beam focusing of low fill-factor DLBs (910 nm and 980 nm): a) top view, b) side view.

Their beam is first collimated by means of a FAC lens, and then is 90º-rotated with a BTS. An additional collimation lens corrects the residual divergence and a pair of lenses focuses the beam in a 400-µm optical fiber.

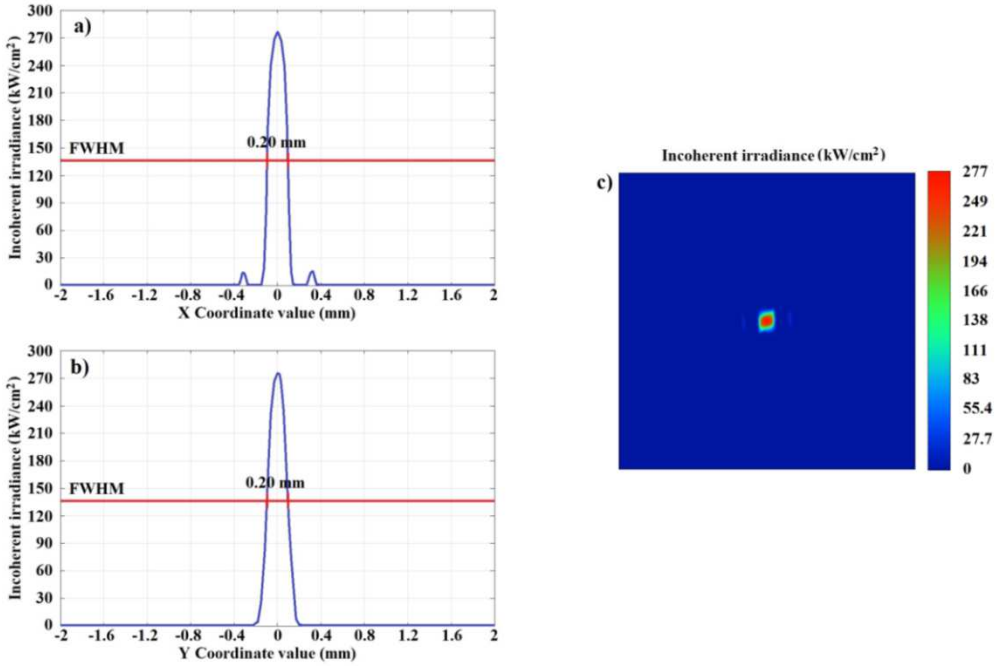

Figure 5.14. Beam profile of the focused spot at 910 nm expressed in incoherent irradiance: a) fast axis, b) slow axis, c) spot focused at the input of the optical fiber.

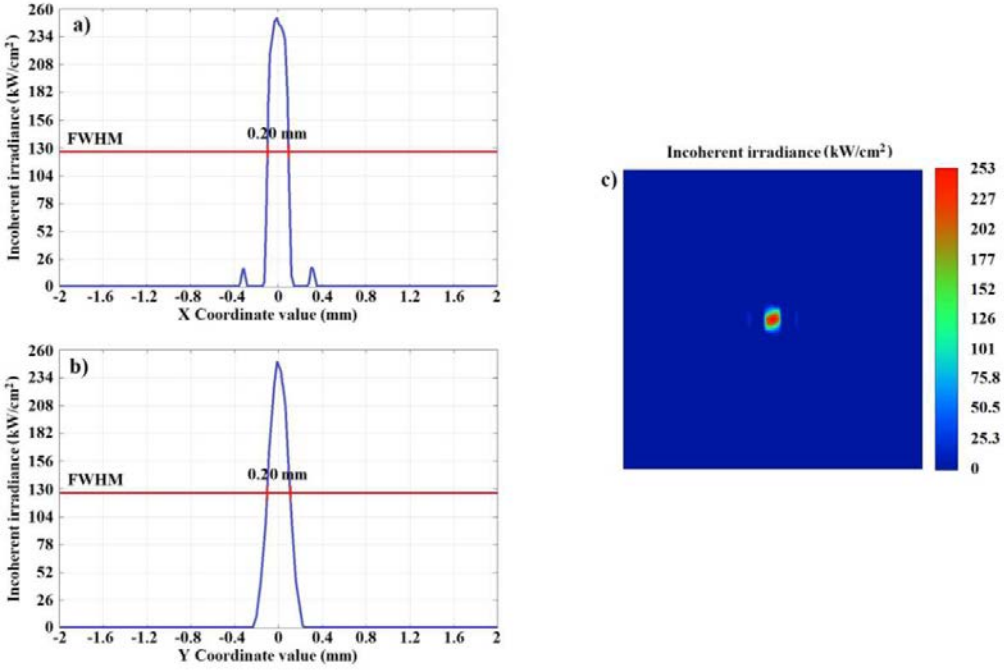

Figure 5.15. Beam profile of the focused spot at 980 nm expressed in incoherent irradiance: a) fast axis, b) slow axis, c) spot focused at the input of the optical fiber.

The beam profiles of the spots focused at the input of the optical fiber are calculated in Zemax in terms of incoherent irradiance in function of the position on x- and y-coordinates, corresponding to fast and slow axis, respectively. In addition, for each DLB the shape of the focused spot is depicted. Figures 5.14 and

5.15 depict the beam spot focused at 910 nm and 980 nm, respectively. In both cases, the focused spot has a size of ~ 0.2 mm x 0.2 mm, which is compatible for focusing into a 400-μm optical fiber. The ideal situation is achieved, since the focused beam has a symmetrical shape.

5.5.2.2. High fill-factor DLBs

As previously specified, the market does not offer BTSs and SAC lenses suitable for high-fill factor DLBs whose pitch is smaller than those used for low fill-factor DLBs. This aspect makes hard the coupling into any optical fiber. In such a way, customized elements are required and their cost would be much higher if compared to the commercial ones. For this reason, it has first been decided to apply a cheaper alternative based on free space propagation by using catalogued lenses. A 940-nm DLB has been considered a as an example for free space optoacoustics (Fig. 5.16). The 940-nm DLB is formed by 37 emitters (Table 5.1) disposed in a horizontal array and the optical peak power emitted can reach 300 W. Essentially, this design consists of a FAC lens close to the source, a beam expander (i.e. a pair of concave and convex lenses) to expand the beam in x-axis, and a focusing lens. The focused spot has a size of ~ 2.8 mm x 2.7 mm (Fig. 5.17). Such a spot cannot be coupled into an optical fiber, but it can be suitable for potential optoacoustic applications in free space. The spot size is ~ 7.6 mm^2 at a focal distance of 16.48 mm from the focusing lens. The spot size keeps a waist of 3 mm ($\pm$ 400 μm) in each axis for a distance of 4 mm. In a second step, it is simulated the same scheme used for low fill-factor DLBs by means of BTSs with pitch of 400 μm, and it is demonstrated an effective beam focusing into 400-μm optical fibers. Figures 5.18, 5.19, and 4.20 depict the beam spot focused at 808 nm, 880 nm, and 940 nm, respectively. In all the cases, the beam spots focused have not a perfect circular shape, but they can be coupled into a 400-μm optical fiber. At 808 nm the focused spot size is ~ 0.25 mm x 0.20 mm, at 880 nm is ~ 0.29 mm x 0.20 mm, and at 940 nm is ~ 0.31 mm x 0.18 mm.

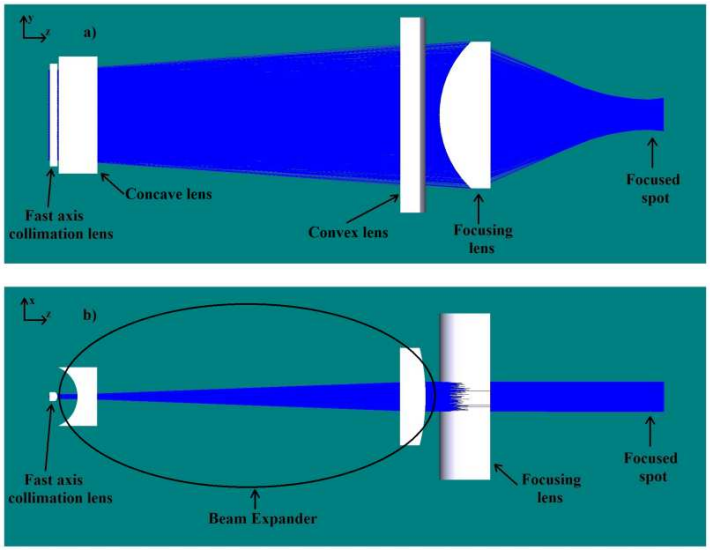

Figure 5.16. Alternative lens system simulated in Zemax for beam focusing of high fill-factor DLBs: a) top view, b) side view.

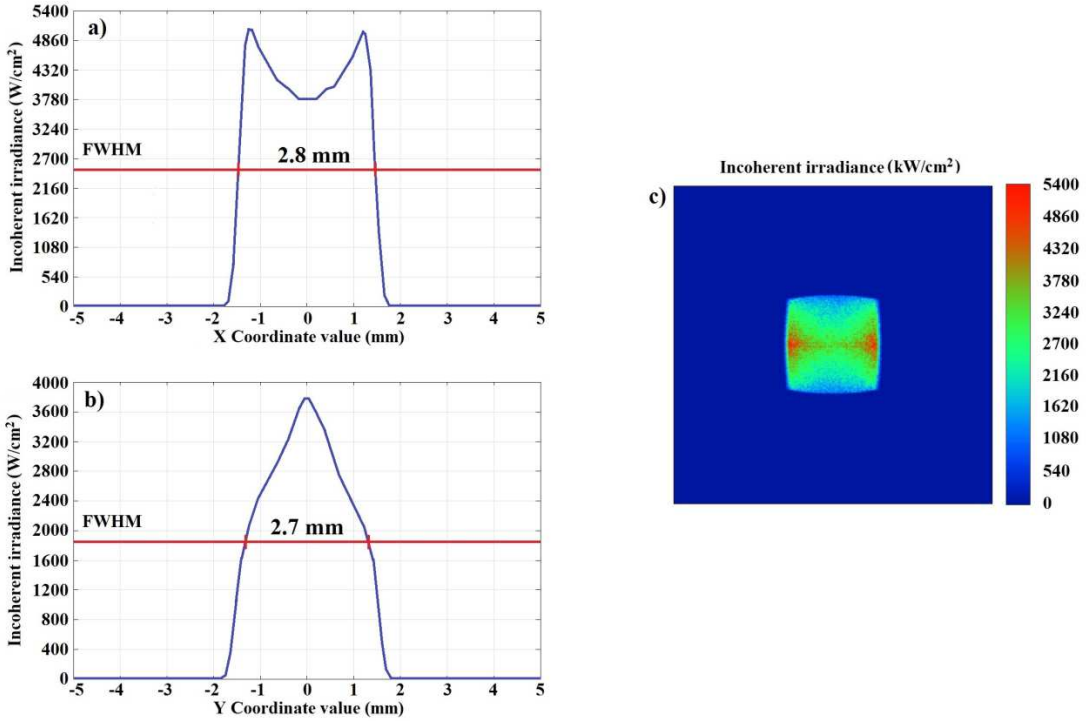

Figure 5.17. Beam profile of the focused spot at 940 nm: a) fast axis, b) slow axis, c) focused spot.

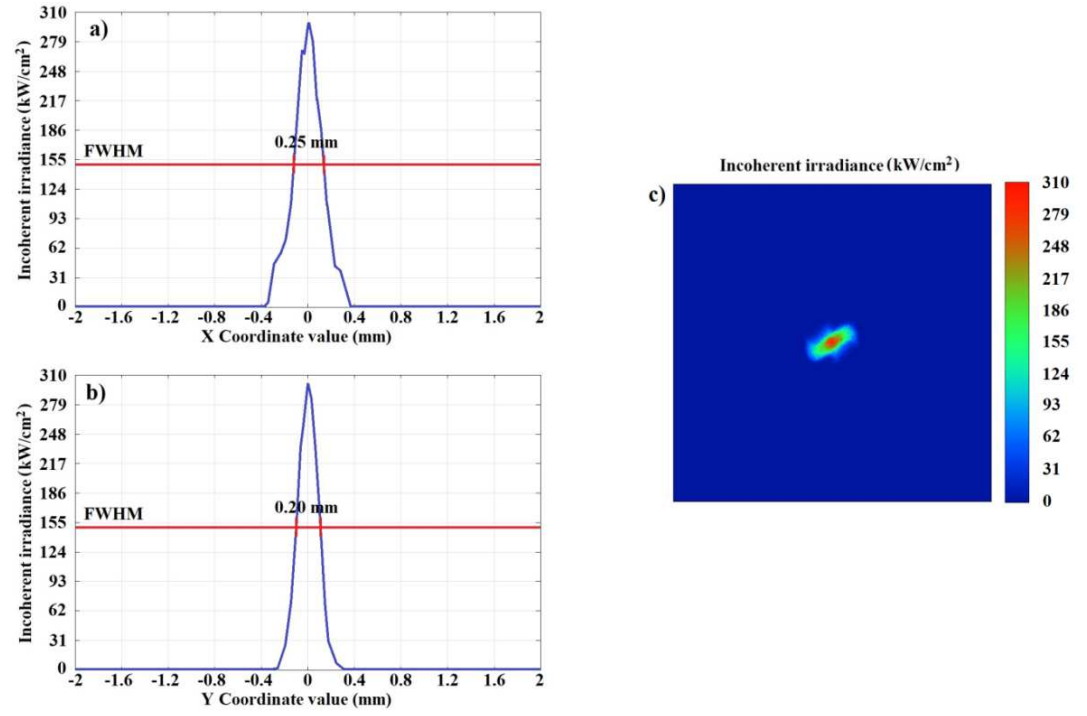

Figure 5.18. Beam profile of the focused spot at 808 nm expressed in incoherent irradiance: a) fast axis, b) slow axis, c) spot focused at the input of the optical fiber.

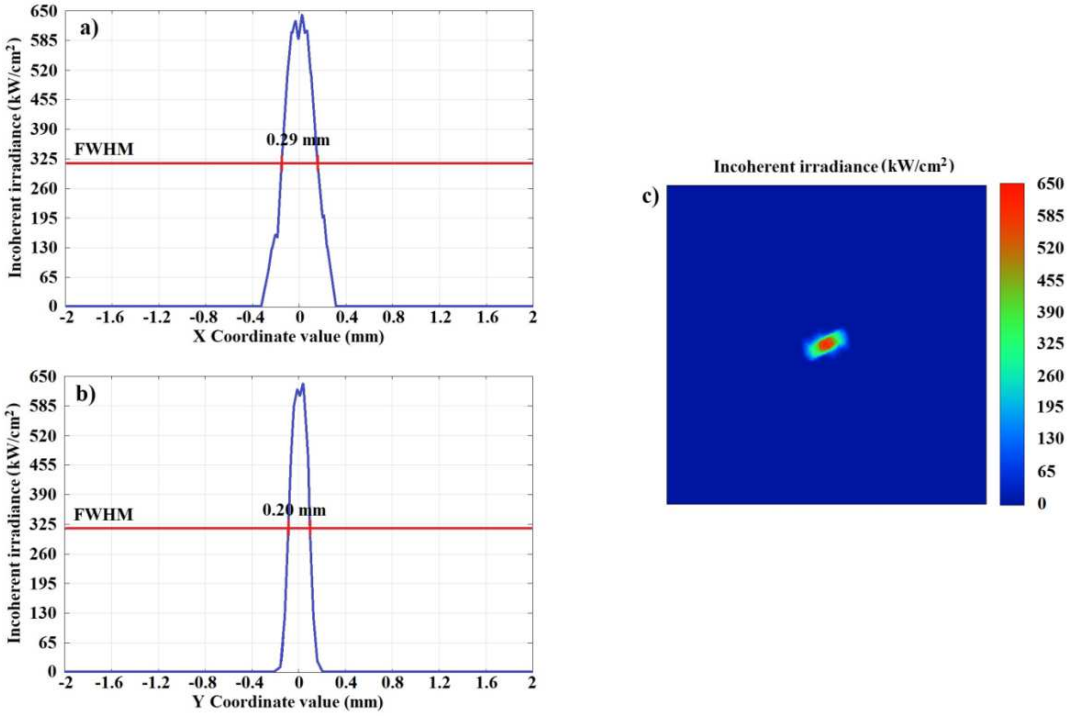

Figure 5.19. Beam profile of the focused spot at 880 nm expressed in incoherent irradiance: a) fast axis, b) slow axis, c) spot focused at the input of the optical fiber.

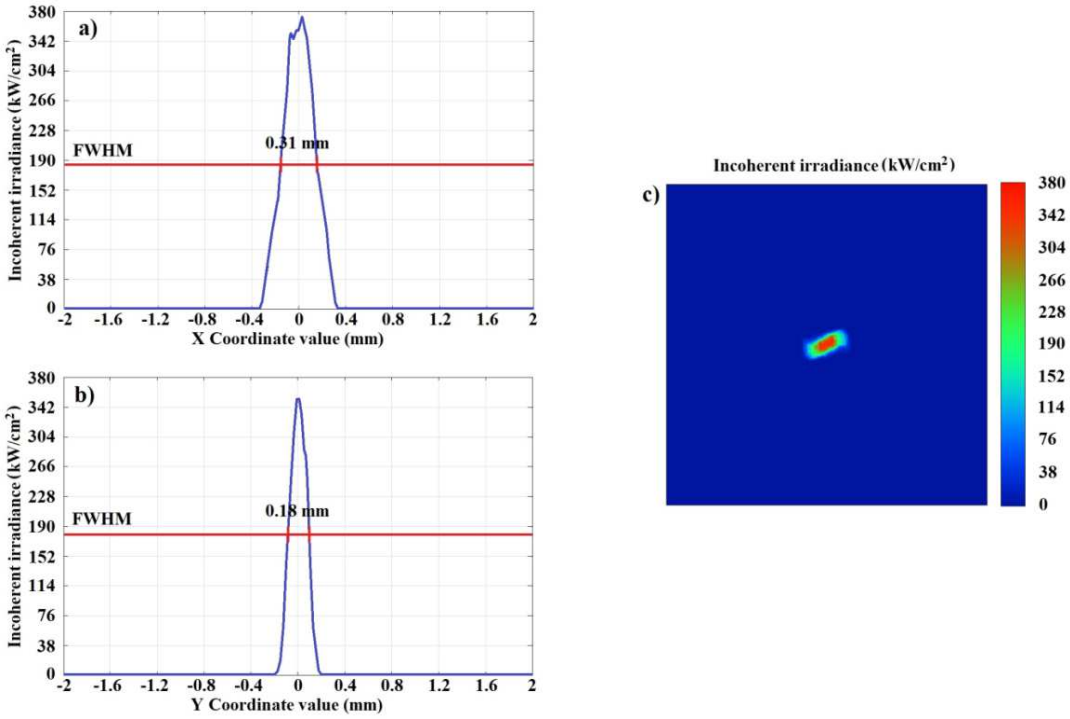

Figure 5.20. Beam profile of the focused spot at 940 nm expressed in incoherent irradiance: a) fast axis, b) slow axis, c) spot focused at the input of the optical fiber.

5.5.2.3. Performances

Table 5.2 summarizes the performances achieved with the proposed designs: the values of the spot sizes achieved for each source and the power percentages before and after the 400-μm optical fiber (N.A. = 0.22) with respect to the power emitted by the sources. The results demonstrate low power losses introduced by the lenses (between 16 % and 18.3 %) for diffraction effects and high coupling efficiencies with the optical fiber. Experimental measurements will be necessary to assess the agreement with the simulated results.

Table 5.2. Performances achieved with the optical designs. *compared to the power of the source

Characteristic	**Value**				
Central wavelength (nm)	808	880	910	940	980
Spot size (fast axis) (mm)	0.25	0.29	0.20	0.31	0.20
Spot size (slow axis) (mm)	0.20	0.20	0.20	0.18	0.20
Optical power before optical fiber* (%)	81.7	81.0	84.0	83.0	84.0
Optical power after optical fiber* (%)	76.3	76.8	78.8	78.3	78.8

The performances of the beam focusing are quantified from the reduction factor of the *BPP* ratio (BPP_y/BPP_x) from the source to the focused spot, located at the input of the optical fiber (Table 5.3). All the emitters have been considered with a vertical size of 2 μm and variable emitter width (Table 5.1), which correspond to the double of the parameters w_{0x} and w_{0y} in Eq. (5.14) and (5.15), respectively. Additionally, the half angle divergences in fast and slow axes have been considered as the half of the mean values reported in Table 5.1. The reduction factor of the *BPP* ratio is quite significant in each case, as it can be seen from Table 5.3.

Table 5.3. *BPP* ratios and corresponding reduction factors from the source to the focused spot calculated for each DLB.

Characteristic	**Value**				
Central wavelength (nm)	808	880	910	940	980
A = BPP_y/BPP_x (source)	~ 731	~ 1227	~ 772	~ 974	~ 772
B = BPP_y/BPP_x (foc. spot)	~ 1.885	~ 1.511	~ 2	~ 1.486	~ 2
Reduction factor (A/B)	~ 388	~ 812	~ 386	~ 655	~ 386

5.5.3. Discussion

A multi-wavelength scheme of DLBs emitting at 808 nm, 880 nm, 910 nm, 940 nm, and 980 nm, respectively, is proposed in a single package based on wavelength-beam combining (WBC) technique. The implementation of this scheme in Zemax is illustrated in Figure 5.21, where the DLBs are disposed in ascending order of wavelength from the left to the right. The beams of the DLBs are collimated in the fast axis by means of a FAC lens and then are 90º-rotated by a BTS and combined by 45º-tilted dichroic mirrors with ideal transmission coefficient spectra (Fig. 5.22). The combined beam is then coupled into an optical fiber (400-µm core diameter, N.A. = 0.22) by using a pair of focusing lenses. Such a design would lead to unsustainable costs for the customization of dichroic mirrors (i.e. ~ 18,000 euros in total), since they are not available in the market with these specifications. In this regard, an alternative design making use of dichroic mirrors and a PBS available in the market (Fig. 5.23) is proposed. In this case, the design is divided into two blocks: on the left there are two DLBs emitting at 940 nm and 880 nm, and on the right there are three DLBs emitting at 808 nm, 910 nm, and 980 nm. On the left, the beam of 940-nm DLB is reflected by a 45º-tilted unprotected gold mirror (model PFSQ05-03-M03, Thorlabs) with reflection coefficient of ~ 0.98 at 940 nm and is transmitted by a 45º-tilted dichroic beam splitter (model DMLP900R, Thorlabs) with transmission coefficient of ~ 0.90 at 940 nm and reflection coefficient of ~ 0.78 at 880 nm. The beam is combined with the radiation reflected at 880 nm. On the right, the beam of 980-nm DLB is reflected by a 45º-tilted unprotected gold mirror (model PFSQ05-03-M03, Thorlabs) with reflection coefficient of ~ 0.98 at 980 nm and is transmitted by a 45º-tilted dichroic beam splitter (model DMLP950R, Thorlabs) with transmission coefficient of ~ 0.99 at 980 nm and reflection coefficient of ~ 0.90 at 910 nm. The beam is first combined with the radiation reflected at 910 nm and then with the beam of 808-nm DLB reflected by a 45º-tilted dichroic beam splitter (model FF875-Di01-25x36, Semrock).

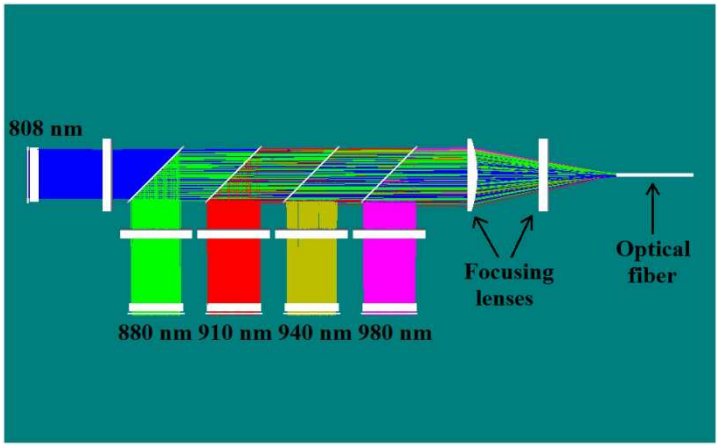

Figure 5.21. Implementation of a multi-wavelength system in Zemax based on the beam combining of five DLBs emitting at 808, 880, 910, 940, and 980 nm, respectively, by using ideal dichroic mirrors.

This device has transmission coefficient of ~ 0.98 at 980 nm and ~ 0.97 at 910 nm, and reflection coefficient of ~ 0.997 at 808 nm. Hence, a PBS (model PBS122, Thorlabs) combines the two beams coming from the bottom and from the left in a single beam that is finally coupled into a 400-µm optical fiber by a pair of focusing lenses. In a real implementation, this system would also need a half-wave plate to rotate the polarization state of one of the two beams. In this case, the overall cost of the dichroic

mirrors, the half-wave plate and the PBS would be ~ 7.5 times less (~ 2,400 euros) than the whole cost of the dichroic mirrors of the system designed in Figure 5.21. Concerning the FAC lenses, BTSs and focusing lenses, the cost would be unchanged because they are the same elements of Figure 5.21. Table 5.4 reports the characteristics of the dichroic mirrors at the wavelengths of interest. Figures 5.24 and 5.25 report their transmission and reflection spectra, respectively.

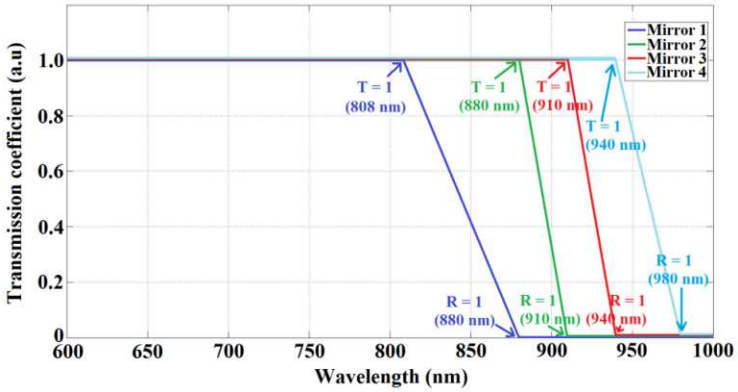

Figure 5.22. Ideal transmission spectra of 45°-tilted dichroic mirrors. The mirrors are labeled with "1, 2, 3, and 4" from the left to the right.

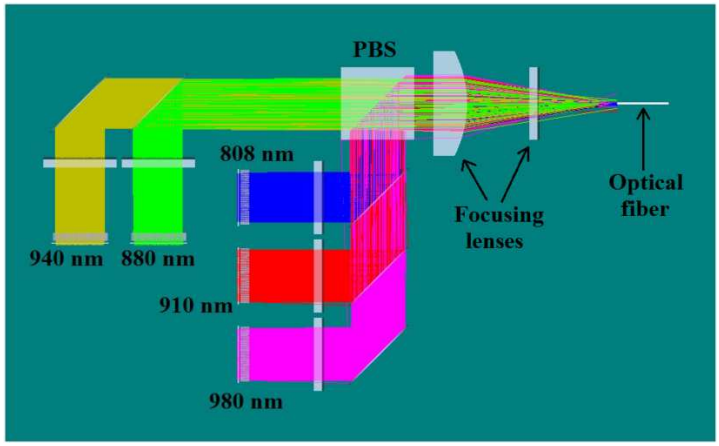

Figure 5.23. Alternative implementation of a multi-wavelength system in Zemax by using commercially available dichroic mirrors and PBS.

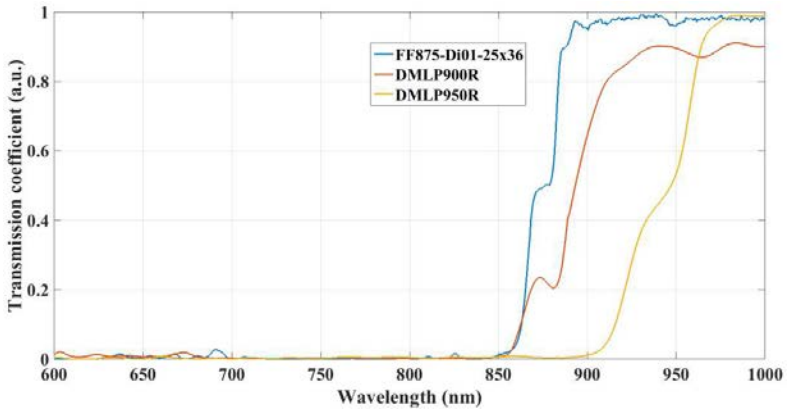

Figure 5.24. Transmission spectra of the dichroic mirrors used in the design of the multi-wavelength system.

Figure 5.26 illustrates the profile of the beam spot focused by the multi-wavelength system. Since the spot size is ~ 0.23 mm x 0.24 mm, it is coupled into a 400-µm optical fiber. The rays diffracted by the BTSs have been removed with filtering in Zemax. However, they represent a negligible portion of power.

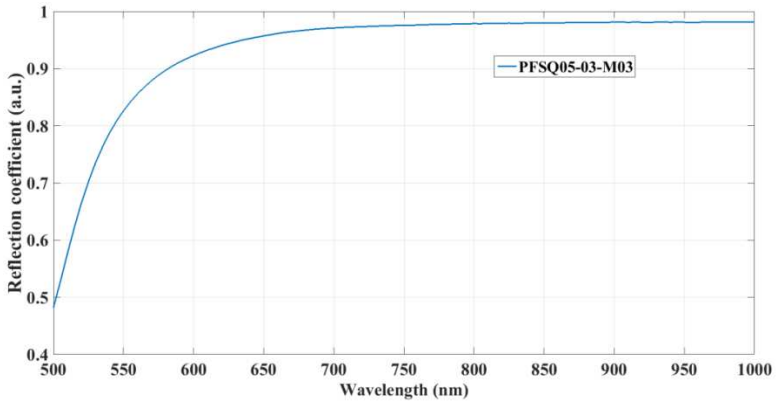

Figure 5.25. Reflection spectrum of the unprotected gold mirrors used to reflect the beam of 940 nm and 980 nm DLBs, respectively.

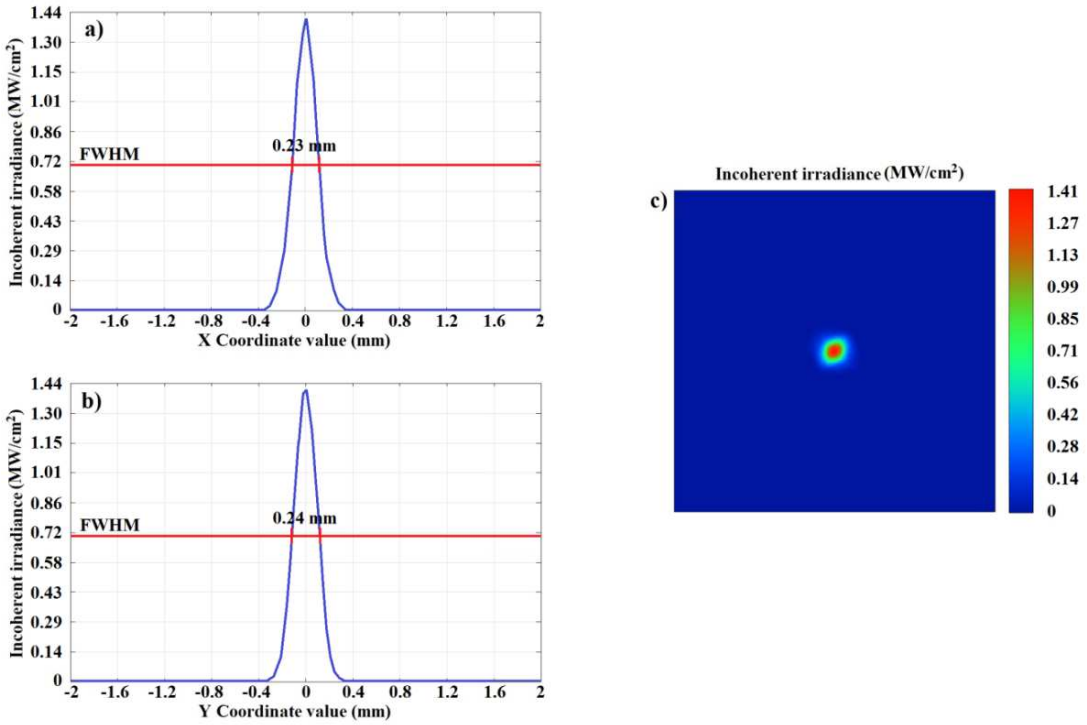

Figure 5.26. Beam profile of the spot focused by the multi-wavelength system: a) fast axis, b) slow axis, c) spot focused at the input of the optical fiber. The multi-wavelength combined beam is easily coupled into a 400-µm optical fiber.

Table 5.5 summarizes the performances achieved with the multi-wavelength design of Figure 5.23. The optical power is coupled into a 400-µm optical fiber and the coupling efficiency is 67.9 %.

Table 5.4. Characteristics of the dichroic mirrors used for the multi-wavelength DLB system. * P-polarization, ** S-polarization

	Characteristics		
Device model	Cutoff wavelength (nm)	Transmission coefficient	Reflection coefficient
PFSQ05-03-M03	560	~ 0.04 (940 nm, 980 nm)	~ 0.98 (940 nm, 980 nm)
FF875-Di01-25x36	875	~ 0.97 (910 nm) ~ 0.98 (980 nm)	~ 0.997 (808 nm)
DMLP900R	900	~ 0.90 (940 nm)	~ 0.78 (880 nm)
DMLP950R	950	~ 0.99 (980 nm)	~ 0.90 (910 nm)
PBS122	-	> 0.9*	> 0.995**

Table 5.5. Performances achieved with the multi-wavelength system. *compared to the power of the source

Characteristic	Value
Spot size (fast axis) (mm)	0.23
Spot size (slow axis) (mm)	0.24
Optical power before optical fiber* (%)	72.0
Optical power after optical fiber*(%)	67.9

5.6. Conclusions

In summary, the beam coupling of single DLBs into 400-µm optical fibers has been modelled at different wavelengths (i.e. 808 nm, 880 nm, 910 nm, 940 nm, and 980 nm) by using Zemax ray tracing software operating in a non-sequential mode. DLBs with different optical power and fill factor have ben simulated, showing significant performances of beam focusing and coupling efficiency into optical fibers. The use of FAC lenses and BTSs has been the key factor for proper beam shaping. In this way, the focusing into small spots has been feasible with additional focusing lenses. Finally, all the sources have been combined in a single package for beam focusing into a 400-µm optical fiber, making use of dichroic mirrors and PBS available in the market. Also, in this case, the results have showed a successful beam focusing in a small spot with very good coupling efficiency. The current multi-wavelength system can be furtherly expanded to other wavelengths (i.e. 630 nm, 650 nm, 760 nm, and 850 nm), following the design scheme proposed in this chapter. The successful coupling of a multi-spectral DLB-based source into a 400-µm optical fiber opens up new possibilities of applications in OAE that require non-invasive inspection of the body, but also for other emerging optoacoustic techniques.

Chapter 6

Conclusions and future work

The purpose of this thesis has been to study the applicability of high-power diode laser sources in optoacoustic systems, simulating their potential applications with some experiments. The necessity to improve the performances and reduce the costs of the existing optoacoustic systems for biomedical applications has been the main motivation of the work presented in this dissertation, in which high-power diode laser sources have been presented as possible candidate to replace the solid state lasers. An optoacoustic setup has been specifically designed and improved to quantify the optoacoustic response of different kinds of nanoparticles embedded in tissue-like phantoms or hosted in quartz cuvettes. To implement this system, a conceptual understanding of the optical propagation in tissues and the processes involved in the optical to acoustic conversion has been necessary.

This study has begun with a review of the optical propagation in attenuating media, where two key parameters associated with this process have been defined: optical absorption and scattering. These are characterized by the absorption and scattering coefficients, μ_{abs} and μ_{sca}, respectively. According to Beer-Lambert law, it has been seen that the optical energy passing through an attenuating medium decreases exponentially with the depth, where the decay constant is directly proportional to the abovementioned attenuation coefficients of the medium. For efficient optoacoustic signal generation to take place, the absorbed optical energy must fulfill both the conditions of stress and thermal confinement, due to thermoelastic expansion of the medium (i.e. a biological tissue) that is irradiated by the optical pulse. It has been shown that the amplitude of the initial pressure induced within the medium is directly proportional to the optical energy absorbed.

The work presented in this dissertation reflects the step-by-step improvements of the research activity realized during my doctoral studies over the last three years and a half. The main issue of this work was to develop a multi-wavelength optoacoustic system based on high-power diode laser sources. Let us summarize the most important achievements and the conclusions obtained for the research.

For the experiments carried out in the laboratory, it has been initially developed a dual-wavelength optoacoustic setup focusing the light emitted by high-power diode lasers (at 870 nm and 905 nm), disposed in a semicircular array, by means of lens tubes. In this case, solutions of double-walled carbon nanotubes and ink have been used in different concentrations, embedded in soft phantoms, to stimulate the optoacoustic signal emission. The preparation of optical phantoms, made of neutral gelatin and agar-agar have, has been shown step-by-step, underlining the importance of using alimentary preservatives to avoid the onset of fungus and permit a longer usage. The optical absorption of the diluted carbon nanotubes and ink solutions has been characterized by the optical power transmitted at 870 nm and 905 nm. Successively, it has been tested how the amplitude of the optoacoustic signals generated is proportional to the pulse width and the optical power applied.

Due to the incapability of the lens tubes to provide a stable alignment, they have been replaced with more stable optical fiber connections to be applicable in a realistic scenario. The beam coupling of the high-power diode lasers has been improved by using optical fibers joined together in fiber bundles to more efficiently illuminate the samples. However, the beam coupling of high-power diode lasers into optical fibers is necessary for endoscopic optoacoustic applications, due to their versatility and practicability. Light emitted by the high-power diode lasers has been first collimated and then focused in optical fibers through small lens systems formed by collimating and focusing lenses, making use of three-dimensional mechanic translators for optimal alignment. It has been mentioned the fabrication process applied to build the fiber bundles, which have been first connectorized using epoxy and afterwards cleaved using ruby scriber and polished. The single optical pulses emitted by the high-power diode lasers have been previously synchronized at both wavelengths before measurements. The optical pulses of the single high-power diode lasers have been first measured individually at the output of the optical fiber bundle. Successively it has been measured the resulting optical pulse when they operated all together. It has been shown that the individual and the combined optical pulses were perfectly overlapped in time and had the same shape, rise and fall times. This test has been very important to check the synchronization of the sources with each other in order to ensure an optimal power combining during the light focusing on the samples.

Secondly, this improved setup has been used to optoacoustically test solutions of graphene oxide (graphene oxide (GO), reduced graphene oxide (rGO), and graphene-oxide/gold nanoparticle hybrid (rGO@Au)) at 905 nm. In this case, the 870-nm sources have not been used because they were unavailable at that time. For this experiment three 905-nm high-power diode lasers coupled to a 675-µm fiber bundle of 200-µm optical fibers have been assembled. For this occasion new phantoms have been fabricated with square shape to host the graphene-oxide solutions. The attenuation coefficients of both the phantom and the graphene-oxide solutions have been characterized from the optical power transmitted, showing some approximations. The absorption coefficient of the phantom and the scattering coefficients of the graphene-oxide solutions have been considered negligible. Optoacoustic signals detected exhibited the highest amplitude with rGO and the lowest with rGO@Au. The optoacoustic sensitivity (optoacoustic signal amplitude/input power) has also been studied in each of the three cases.

Successively, two solutions of gold nanorods dispersed in distilled water (0.8 mg/ml) with absorption peak at ~ 860 nm and ~ 900 nm, respectively, and hosted in tissue-like phantoms have been used to generate optoacoustic signals at 870 and 905 nm. Three holes with different diameters (i.e. 1 mm, 2 mm, and 4 mm) have been done in the phantoms at different depths (0.9 cm, 1.8 cm, and 2.7 cm) to host the gold nanorods inclusions. Their optoacoustic response has been evaluated: the highest amplitude has been detected with the 4-mm inclusion and the lowest with the 1-mm inclusion. Also, their signal-to-noise ratios have been evaluated considering the floor noise as reference. In the same work it has been remarked that the high optoacoustic response exhibited by gold nanorods make them suitable for potential application in OAS as exogenous contrast agents to detect and monitor emerging diseases.

Afterward, an inverse algorithm has been proposed to estimate the concentrations C_m of M chromophores with known absorption coefficient spectra $\mu_m(\lambda_n)$, expressed in a NxM matrix, from the normalized optoacoustic signals $B(\lambda_n)$ detected at N wavelengths. It has been discussed the non-linear dependence of the parameter $B(\lambda_n)$ on the attenuation of the input optical power $P(\lambda_n)$ along the optical path d. Then, it has been assumed a linear system considering that all the signal amplitude comes from the entrance of

the cuvette (i.e. $d \ll 1$). Specifically, the absolute concentrations C_1 and C_2 of two gold nanorods solutions mixed in quartz cuvette in three different proportions (i.e. 40/60, 50/50, and 60/40) have been estimated from the analysis of the optoacoustic signals detected at 870 nm and 905 nm. The calculated values of C_1 and C_2 presented a maximum observational error of 2.76 % from the expected values. The pulses produced to generate optoacoustic signals have been alternated between the two wavelengths by a microcontroller circuit with fast switching (0.5 ms). Successively, a 972-nm diode laser bar has been added to the system to further reduce the error to a maximum value of 1.34 %. In this case, the switching times between the three wavelengths have been reduced to 0.33 ms. In this work, it has been discussed that one potential application of this method is the real-time assessment of the quantity of gold nanoparticles that should be administered to the patient to have appreciable contrast between the interested chromophores.

Finally, the discussed importance of achieving high optical energy levels for optoacoustic applications has prompted the last work presented in this dissertation, concerning the modeling of new high power diode laser sources by using the software Zemax. It has been proposed the design of several commercially available high-power diode laser bars with low (< 50 %) and high fill factor (> 50 %) (See also Appendix C) that can operate at both quasi-continuous wave and pulsed regimes in the near-infrared spectrum (i.e. 808 nm, 880 nm, 910 nm, 940 nm, and 980 nm). About this, it has been remarked that one potential application of diode laser bar sources is optoacoustic endoscopy that requires a non-invasive inspection of the human body. To do so, the beam coupling into optical fibers is required. In this regard, specific optical microlenses taken from catalogue (i.e. fast axis collimation lenses, beam twisters, and focusing lenses) have been modelled to achieve the focusing of their beams into 400-μm optical fibers showing very good coupling efficiencies (between ~ 76.3 % and ~ 78.8 %). Secondly, based on wavelength-beam combining technique, these sources have been simulated in a compact multi-wavelength scheme making use of dichroic mirrors and other optical elements to focus their combined beam into a 400-μm optical fiber, showing also in this case an high efficiency (~ 67.9 %). As a result, the high efficiency achieved demonstrates the capability of this assembled system to be applied in real optoacoustic applications.

In conclusion, it has been observed that the proposed multi-wavelength system based on diode laser bars can be furtherly expanded to other wavelengths (i.e. 630 nm, 650 nm, 760 nm, and 850 nm) for a more functional optoacoustic imaging, and needs fabrication to validate the novelty of the results achieved. The experimental work presented in this thesis has opened up new lines of investigation on the development and implementation of both diode laser sources and nanoparticles for optoacoustic applications. In addition, the accurate determination of absolute concentrations achieved with the gold nanorods by using diode laser sources (i.e. high-power diode lasers and a diode laser bar) represents a novelty for future applications involving the quantification of any chromophore or contrast agent present in human body.
However, the main issue of this challenge is represented by the limited availability of high-power diode laser sources in a large range of near infrared wavelengths. We have seen that diode laser bars offer more versatility in terms of high optical power and wavelengths of emission.
In this regard, a novel application of the multi-wavelength system designed in Chapter 5 with diode laser bars can be the determination of absolute concentrations of chromophores or contrast agents, since a large amount of optical power is required to penetrate in-depth inside the tissues. However, the optical power available for optoacoustic applications can be further increased by using diode laser stacks.

Conclusiones y trabajo futuro

El propósito de esta tesis ha sido de estudiar la aplicabilidad de fuentes de diodos láseres de alta potencia en sistemas optoacústicos, simulando sus potenciales aplicaciones con algunos experimentos. La necesidad de mejorar las prestaciones y reducir los costes de los sistemas optoacústicos existentes para aplicaciones biomédicas ha sido la principal motivación del trabajo presentado en esta disertación, en el cual se han presentado fuentes de diodos láseres de alta potencia como posibles candidatos para sustituir los láseres de estado sólido. Un sistema optoacústico ha sido específicamente diseñado y mejorado para cuantificar la respuesta optoacústica de diferentes tipos de nanoparticulas embedidas en phantoms con características ópticas similares a las de los tejidos biológicos o colocadas en cubetas de cuarzo. Para implementar este sistema, se ha necesitado una comprensión conceptual de la propagación óptica en los tejidos y de los procesos implicados en la conversión optoacústica.

Este estudio ha comenzado con una revisión de la propagación óptica en medios atenuantes, donde se han definido dos parámetros clave asociados con este proceso: absorción y dispersión óptica. Estos se caracterizan por los coeficientes de absorción y dispersión, μ_{abs} y μ_{sca}, respectivamente. De acuerdo con la ley de Beer-Lambert, se ha visto que la energía óptica que pasa a través de un medio atenuante disminuye exponencialmente con la profundidad, donde la constante de decaimiento es directamente proporcional a los coeficientes de atenuación del medio mencionados anteriormente. Para que tenga lugar una generación eficaz de señales optoacústicas, la energía óptica absorbida debe cumplir tanto la condición de confinamiento de estrés como la de confinamiento térmico, debido a la expansión termoelástica del medio (como por ejemplo un tejido biológico) que es irradiado por el pulso óptico. Se ha demostrado que la amplitud de la presión inicial inducida dentro del medio es directamente proporcional a la energía óptica absorbida.

El trabajo presentado en esta disertación refleja paso a paso los progresos de la actividad de investigación realizada durante mis estudios doctorales en los últimos tres años y medio. El principal asunto de este trabajo ha sido desarrollar un sistema optoacústico de múltiples longitudes de onda basado en fuentes de diodos láseres de alta potencia. Resumamos los logros más importantes y las conclusiones obtenidas con esta investigación.

Para los experimentos realizados en el laboratorio, se ha desarrollado inicialmente una configuración optoacústica de dos longitudes de onda enfocando la luz emitida por los diodos láseres de alta potencia (a 870 nm y 905 nm), dispuestos en una configuración semicircular, mediante tubos de lente. En este caso, unas soluciones de nanotubos de carbono "double-walled" y de tinta se han utilizado en diferentes concentraciones, embedidas en phantoms de baja dispersión, para estimular la emisión de señales optoacústicas. La preparación de phantoms ópticos, hechos de gelatina neutra y agar-agar, se ha mostrado paso a paso, acentuando la importancia de usar conservantes alimentarios para evitar la formación de hongos y permitir un uso más prolongado. La absorción óptica de las soluciones de nanotubos de carbono y de tinta diluidos se ha caracterizado con la potencia óptica transmitida a 870 nm y 905 nm. Sucesivamente, se ha probado cómo la amplitud de las señales optoacústicas generadas es proporcional al ancho de pulso y a la potencia óptica aplicada.

Debido a la inhabilidad de los tubos de lentes para proporcionar una alineación estable, esos han sido reemplazados con conexiones de fibras ópticas más estables para ser aplicables en un escenario real. El acoplo de los haces de los diodo láseres de alta potencia ha sido mejorado utilizando fibras ópticas unidas en "fiber bundles" para iluminar las muestras más eficientemente. Sin embargo, el acoplo de los haces de los diodos láseres de alta potencia en fibras ópticas es necesario para las aplicaciones optoacústicas endoscópicas, debido a su versatilidad y practicidad. La luz emitida por los diodos láseres de alta potencia ha sido primero colimada y luego enfocada en fibras ópticas a través de pequeños sistemas de lentes formados por lentes colimadoras y de enfoque, haciendo uso de sistemas mecánicos para una alineación óptima en las tres dimensiones. Se ha mencionado el proceso de fabricación aplicado para construir los fiber bundles, los cuales han sido primero conectados con epoxi y después partidos y pulidos usando un pulidor de rubí. Los pulsos ópticos individuales emitidos por los diodos láseres de alta potencia han sido previamente sincronizados en ambas longitudes de onda antes de las medidas. Los pulsos ópticos de los diodos láseres de alta potencia se han medido primero individualmente a la salida del fiber bundle. Sucesivamente se ha medido el pulso óptico resultante cuando todos los láseres operaban todos juntos. Se ha demostrado que los pulsos ópticos individuales y combinados se superponían perfectamente en el tiempo y tenían la misma forma y los mismos tiempos de subida y caída. Esta prueba ha sido muy importante para comprobar la sincronización de las fuentes con el fin de garantizar una óptima combinación de potencia durante el enfoque de la luz en las muestras.

En segundo lugar, este sistema mejorado se ha utilizado para probar optoacústicamente soluciones de óxido de grafeno (óxido de grafeno (GO), óxido de grafeno reducido (rGO) e híbrido de óxido de grafeno y nanoparticulas de oro (rGO@Au) a 905 nm. En este caso, las fuentes de 870 nm no se han utilizado porque no estaban disponibles en ese momento. Para este experimento se han ensamblado tres diodos láseres de alta potencia de 905 nm acoplados a un fiber bundle de 675 μm formado por fibras ópticas de 200 μm. Para esta ocasión se han fabricado nuevos phantoms con forma cuadrada para colocar las soluciones de óxido de grafeno. Los coeficientes de atenuación de las soluciones de óxido de grafeno y del phantom se han caracterizado a partir de la potencia óptica transmitida, mostrando algunas aproximaciones. El coeficiente de absorción del phantom y los coeficientes de dispersión de las soluciones de óxido de grafeno se han considerado despreciables. Las señales optoacústicas detectadas tenían la mayor amplitud con rGO y la más baja con rGO@Au. La sensibilidad optoacústica (amplitud de la señal optoacústica/potencia de entrada) también se ha estudiado en cada uno de los tres casos.

Sucesivamente se han utilizado dos soluciones de nanoparticulas de oro esparcidas en agua destilada (0,8 mg/ml) con picos de absorción a ~ 860 nm y ~ 900 nm, respectivamente, y colocadas en phantoms con características similares a las de los tejidos biológicos para generar señales optoacústicas a 870 y 905 nm. Se han realizado tres agujeros con diferentes diámetros (es decir 1 mm, 2 mm y 4 mm) en los phantoms a diferentes distancias (0,9 cm, 1,8 cm y 2,7 cm) para colocar las soluciones de nanoparticulas de oro. Se ha evaluado sus respuestas optoacústica: la mayor amplitud se ha detectado con la inclusión de 4 mm y la más baja con la inclusión de 1 mm. Además, sus relaciones señal-ruido se han evaluado considerando el ruido de fondo como referencia. En el mismo trabajo se ha observado que la elevada respuesta optoacústica exhibida por las nanoparticulas de oro los hacen adecuados para potenciales aplicaciones en espectroscopia optoacústica como agentes de contraste exógenos para detectar y controlar enfermedades emergentes.

Posteriormente, se ha propuesto un algoritmo inverso para estimar las concentraciones C_m de M cromóforos con espectros de absorción conocidos $\mu_m(\lambda_n)$, expresados en una matriz $N\,x\,M$, a partir de las señales optoacústicas normalizadas $B(\lambda_n)$ detectadas a N longitudes de onda. Se ha discutido la dependencia no lineal del parámetro $B(\lambda_n)$ sobre la atenuación de la potencia óptica de entrada $P(\lambda_n)$ a lo largo del camino óptico d. Luego, se ha asumido un sistema lineal considerando que toda la amplitud de la señal proviene de la entrada de la cubeta (es decir $d \ll 1$). Específicamente, se han estimado las concentraciones absolutas C_1 y C_2 de dos soluciones de nanoparticulas de oro combinadas en una cubeta de cuarzo en tres proporciones diferentes (es decir 40/60, 50/50 y 60/40) a partir del análisis de las señales optoacústicas detectadas a 870 nm y 905 nm. Los valores calculados de C_1 y C_2 han presentado un error de observación máximo de 2.76% de los valores esperados. Los pulsos producidos para generar señales optoacústicas han sido alternados entre las dos longitudes de onda por un circuito microcontrolador con conmutación rápida (0,5 ms). Sucesivamente, se ha añadido una barra de diodos láseres de 972 nm al sistema para reducir aún más el error hasta un valor máximo de 1,34%. En este caso, los tiempos de conmutación entre las tres longitudes de onda se han reducido a 0,33 ms. En este trabajo se ha discutido que una posible aplicación de este método es la evaluación en tiempo real de la cantidad de nanoparticulas de oro que se deben administrar al paciente para conseguir un contraste apreciable entre los cromóforos interesados.

Por fin, la argumentada importancia de alcanzar altos niveles de energía óptica para aplicaciones optoacústicas ha impulsado el último trabajo presentado en esta disertación sobre el modelado de nuevas fuentes de diodos láseres de alta potencia mediante el software Zemax. Se ha propuesto el diseño de varias barras de diodos láseres de alta potencia comercialmente disponibles con bajo (<50%) y alto "fill factor" (> 50%) (Véase también el Apéndice C) que pueden operar en ambos regímenes de onda cuasi-continua y pulsado en el espectro del infrarrojo cercano (es decir 808 nm, 880 nm, 910 nm, 940 nm y 980 nm). Sobre esto, se ha observado que una potencial aplicación de las barras de diodos láseres es la endoscopia optoacústica que requiere una inspección no-invasiva del cuerpo humano. Para esto, se requiere el acoplo del haz en fibras ópticas. A este respecto, se han modelado microlentes ópticas específicas elegidas en catálogos (como por ejemplo lentes FAC, "beam twisters" y lentes de enfoque) para conseguir el enfoque en fibras ópticas de 400 μm, mostrando muy buenas eficiencias de acoplo (entre el 76,3% y ~ 78,8%). En segundo lugar, basándose en la técnica de combinación de longitudes de onda, estas fuentes se han simulado en un esquema compacto de múltiples longitudes de onda utilizando espejos dicroicos y otros elementos ópticos para enfocar su haz combinado en una fibra óptica de 400 μm, mostrando también en este caso una alta eficiencia (~ 67,9%). Como resultado, la alta eficiencia obtenida demuestra la capacidad de este sistema ensamblado para ser aplicado en aplicaciones optoacústicas reales.

En conclusión, se ha observado que al sistema propuesto de múltiples longitudes de onda basado en barras de diodos láseres se pueden añadir otras longitudes de onda (es decir 630 nm, 650 nm, 760 nm y 850 nm) para una imagen optoacústica más funcional y necesita fabricación para validar la novedad de los resultados obtenidos. El trabajo experimental presentado en esta tesis ha abierto nuevas líneas de investigación sobre el desarrollo e implementación de fuentes de diodos láseres y nanoparticulas para aplicaciones optoacústicas. Además, la determinación exacta de las concentraciones absolutas de las nanoparticulas de oro usando fuentes de diodos láseres (es decir diodos láseres de alta potencia y una barra de diodos láseres) representa una novedad para futuras aplicaciones que implican la cuantificación de cualquier cromóforo o agente de contraste presente en el cuerpo humano.

Sin embargo, el problema principal de este reto está representado por la limitada disponibilidad de fuentes de diodos láseres de alta potencia en una amplia gama de longitudes de onda en el infrarrojo cercano. Se ha visto que las barras de diodos láseres ofrecen más versatilidad en términos de alta potencia óptica y longitudes de onda de emisión.

A este respecto, una nueva aplicación del sistema de múltiples longitudes de onda diseñado en el Capítulo 5 con las barras de diodos láseres puede ser la determinación de concentraciones absolutas de cromóforos o agentes de contraste, ya que se requiere una gran cantidad de potencia óptica para penetrar en profundidad dentro de los tejidos. Sin embargo, la potencia óptica disponible para aplicaciones optoacústicas se puede aumentar adicionalmente usando pilas de diodos láseres.

Appendix A

Principles of diode lasers

A.1. Introduction

Diode lasers (DLs) are electrically pumped semiconductor lasers able to generate optical gain by an electric current flowing through a heterostructure (p–n junction) where electrons and holes recombine, releasing the energy in the form of photons. This process can be spontaneous or stimulated by external pumping from other laser sources, leading to optical amplification. DLs have an optical feedback that is usually realized by cleaving the semiconductor material along its crystal planes. The harsh difference in refractive index between the crystal (~ 3.5) and the surrounding air causes the cleaved surfaces to act as reflectors. Consequently, the semiconductor crystal behaves both as a gain medium and as a Fabry-Perot optical resonator. On condition that the optical gain is sufficiently large, the feedback converts the optical amplification into an optical oscillation that produces *lasing*.

Some important properties of DLs are determined by the geometry of the cavity of the optical resonator. Basically, if the light is contained within a very thin layer (<< λ), the waveguide structure of the diode laser supports only a single optical mode (Figure A.1(a)) in the direction perpendicular to the layers. In this case the DL is known as “single-mode”. Some kinds of DLs, in particular the *distributed feedback lasers* [170], operate on a single resonance mode, so that the emission bandwidth is quite narrow. In the transverse direction, if the resonator length of the waveguide is large compared to the operating wavelength of light (>> λ), then the waveguide can support multiple transverse optical modes, and the DL is known as "multi-mode", or even “broad-area” (Figure A.1(b)).

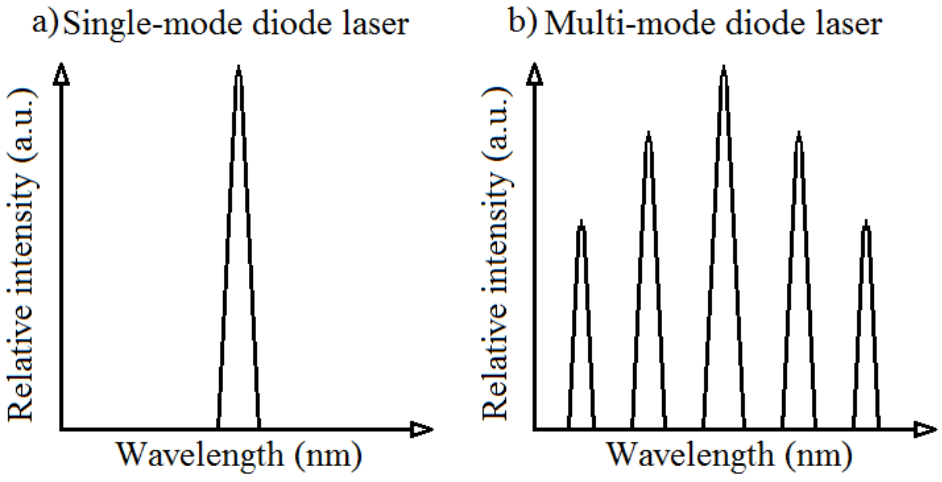

Figure A.1. Spectrum of: a) single mode and b) multi-mode diode lasers.

The typical emission width of broad-area DLs is between 100 μm and 300 μm, corresponding to several hundreds of times more their central emission wavelength, while the height is no more than 2 μm. Such as a broad waveguide supports many guided modes, resulting in the typical multimode beam characteristics of the DLs. The DLs used in this thesis are broad-area (i.e. 200 μm and 300 μm, respectively). They belong to the category of *edge-emitting lasers*, where the laser resonator is formed by coated or uncoated end facets. Most of them emit a beam with an optical bandwidth of a few nanometers. This bandwidth results from the simultaneous oscillation of multiple longitudinal (and possibly transverse) resonance modes that makes them multi-mode DLs.

The optical resonator of a DL consists of a waveguide layer built between two crystal facets working as mirrors (Fig. A.2). One of these facets is coated to achieve the optimal reflectivity, while the other one is low reflective to allow the light emission. The intensity distribution of the propagation modes and the number of modes in the vertical dimension are determined by the thickness and composition of the grown layers. The propagation modes can have two polarizations: one is nearly transverse electric (TE) and one nearly transverse magnetic (TM). The electrical field vector of the TE modes and the magnetic field vector of the TM modes oscillate in the parallel direction to the epitaxial layers. In the lateral direction, the mode distribution is determined by geometrical aspects of the current injection and by the waveguide structure. The efficiency of these devices is very high, since almost all the recombination processes can contribute to the optical gain.

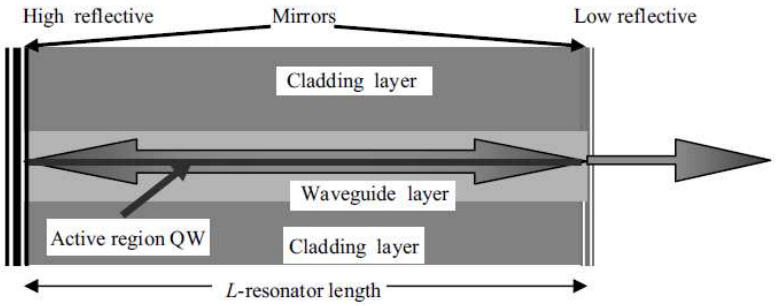

Figure A.2. Schematic of the optical resonator of a DL [171].

A typical scheme of a semiconductor DL structure is shown in Figure A.3. A DL is electrically a PIN diode; when a positive electrical potential is applied at the p-doped region, the holes will move to the n-doped region. A negative electrical potential at the n-doped region will drive the electrons to the p-doped region. In this way, the carriers (both electrons and holes) are pumped from the respective n- and p-doped regions into the active region (called also "pn-junction"), where they are recombined and create one photon. To achieve a substantial current flow, the electrical potential supplied must be at least slightly above the potential difference in the band gap. All modern lasers use the double-heterostructure implementation, where the carriers and the photons are confined in order to maximize their probabilities of recombination and light generation. The DL is formed by an epitaxial structure[1] that is grown on a metal n-contact starting from an n-doped cladding (substrate) and growing an n-doped waveguide layer, followed by the active region, a p-doped waveguide, a p-doped cladding, and finally a metal p-contact. In modern semiconductor DLs, due to development of modern epitaxial growth methods, the active region consists of a quantum well[2], which provide lower threshold current and higher efficiency [172].

[1]Epitaxial refers to the deposition of a crystalline overlayer on a crystalline substrate.

[2]The active region of the device is so narrow that quantum confinement occurs. The confining dimension is large compared to the wavelength of the particles confined.

In quantum well, a thin layer of about 10 nm (InGaAs, AlInGaAs or GaAsP) is surrounded by material with a larger band gap. The injected carriers are confined in a very thin layer by the potential barriers of the larger band gap material. DLs are fabricated using direct bandgap semiconductors (Fig. A.4).

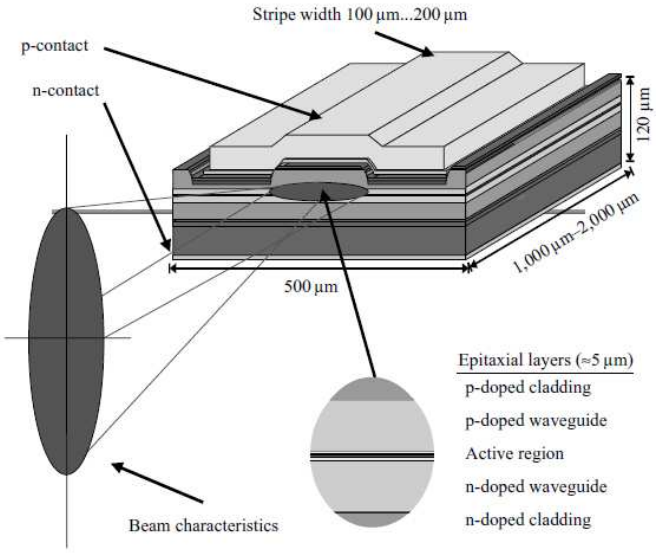

Figure A.3. Typical structure of a semiconductor DL formed by epitaxial layers [171].

When an electron is raised into the conduction band (i.e. by absorption of a photon or injected current), it leaves a hole in the valence band. The optical gain is then generated by radiative recombination of these electron-hole pairs. DLs are fabricated with III-V compound semiconductors that exhibit direct band gaps, so that they have high carrier mobility that makes them suitable for light-emitting optoelectronic components. Gallium arsenide, indium phosphide, gallium antimonide, and gallium nitride are typical examples of compound semiconductor materials that can be used to create DLs. The transition between the materials creates the direct bandgap property.

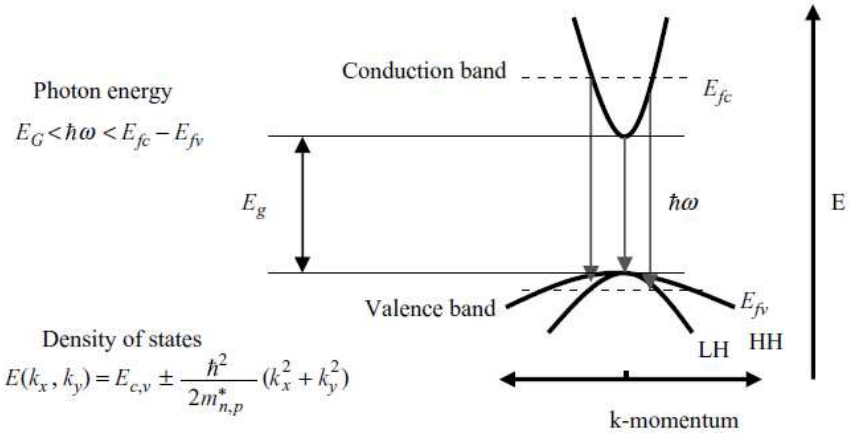

Figure A.4. Band structure of a DL based on direct bandgap property that allows efficient generation of light after electron-hole pair recombination. E_g is the energy difference between valence and conduction band, while E_{fc} and E_{fv} are the quasi-Fermi levels [171].

The energy of the generated photon corresponds to the difference between the energy levels of the valence band and conduction band. The wavelength of the emitted radiation is determined by the size of the band gap and by the composition of the active region. High-power DLs emitting in the wavelength region between 700 nm and 1 μm are typically realized with GaAs [171].
Some low-power DLs can emit light beams with relatively high beam quality. However, most high-power DLs exhibit a relatively poor beam quality that produces astigmatism, due to a high asymmetry of the beam profile between fast and slow axes (Fig. A.5). In far field the propagated beam has an elliptical cross-section. The axis with larger divergence angle is called "fast axis", while the axis with smaller divergence angle is called "slow axis". From the beam profiles of Figure A.5 it is possible to calculate the fast- and slow-axis divergence angles.

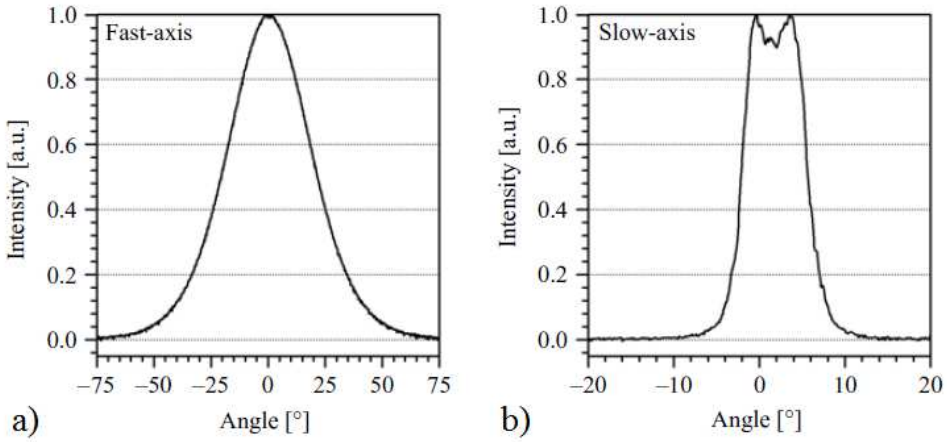

Figure A.5. Normalized far-field intensity distributions in a) fast axis and b) slow axis of a DL [171].

For the calculation of the divergence angles there are different definitions commonly used: i) the divergence angle at 50 % of the maximum intensity, i.e. the "full width at half-maximum" (FWHM) criterion, ii) the divergence angle at $1/e^2$ of the maximum intensity, and iii) the criterion of 95% of power inclusion that is motivated by the practical need of achieving a certain transmission efficiency through optics with limited aperture (Fig. A.6).

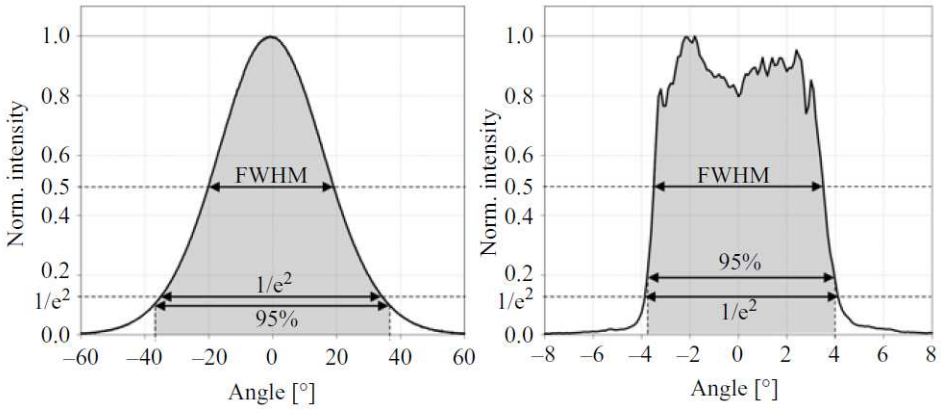

Figure A.6. Determination of divergence angles in according to different definitions [171].

The elliptical beam profile caused by asymmetric divergence angles can be adjusted by means of beam shaping lenses, such as collimating and focusing lenses. In this chapter collimating and focusing lens pairs are used to couple the DL beam into optical fibers.

Some mathematic models to describe the source field of a single emitter DL have been studied, such as Gauss model, exponent model, and Lorentz model. In practice, Gauss model has been widely used to describe the source field $E(x_0, y_0)$ and it is expressed as [173, 174]:

$$E(x_0, y_0) = A_0 \exp\left[-\left(\frac{x_0^2}{w_{0x}^2} + \frac{y_0^2}{w_{0y}^2}\right)\right], \tag{A.1}$$

where A_0 is the amplitude of the source field, w_{0x} and w_{0y} are the beam waist radius in fast and slow axis, respectively, while x_0 and y_0 denote fast and slow axes at source facet, respectively.

Analogously to a LED, a DL needs a forward voltage drop across the p-n junction to emit light. A forward current is then generated producing optical gain in the medium. Depending on the current intensity, a DL can operate in two different modalities: i) LED emitting region and ii) laser oscillating region. The current for which the gain satisfies the lasing condition is the threshold current of the laser I_{th} (laser oscillating region), below which a very little light is emitted by the laser structure (LED emitting region). For an applied current larger than the threshold current, the output optical power P_{out} increases linearly with the applied current, as illustrated in Figure A.7. The output optical power above the threshold current can be expressed by the following equation:

$$P_{out} = \eta \frac{h\nu}{q}\left(I_{op} - I_{th}\right), \tag{A.2}$$

where $h\nu$ is the energy per photon (Joule), η is the slope efficiency that indicates that only a fraction of the generated photons contributes to the output power of the laser due to the optical losses throughout the waveguide, q is the electric charge (~1.6×10^{-19} Coulomb), and I_{op} is the operation current.

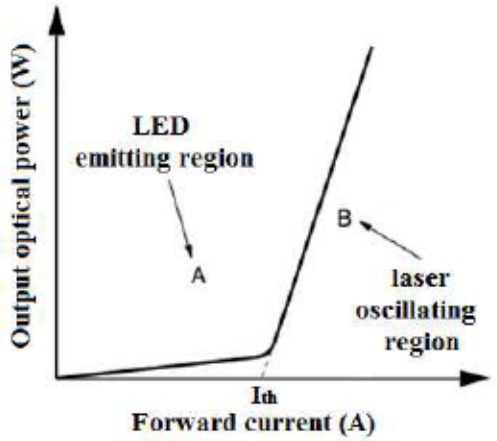

Figure A.7. Characteristic curve of a DL divided into two regions: below the threshold current I_{th} the output optical power emitted by the DL is very low (LED operation), while after I_{th} it starts to increase quickly in a linear relationship with the input current (laser operation).

A.2. Pulsed high-power diode lasers

DLs are subdivided into continuous and pulsed sources. Although the most common mode of operation of DLs is continuous-wave operation, many DLs can also generate optical pulses. In most cases, the principle of pulse generation is gain switching that consists in modulating the optical gain of the DL by switching the injection current. Small DLs can also be mode-locked to generate picosecond or even femtosecond pulses. In this dissertation, only pulsed high-power diode lasers (HPDLs) based on gain switching, whose current pulses are supplied by an external current driver, have been used. Normally, pulsed HPDLs emit optical pulses widths from ns to μs, while in our case the maximum ratings of the DLs require to not exceed 100 ns. For this category of DLs one important parameter is the duty cycle (d.c.), which is the ratio between the pulse width T_p and the repetition time T_r between two successive pulses. Alternatively, it can be expressed as the pulse width T_p multiplied by the repetition rate F_r. In both cases, it can be expressed as a percentage:

$$d.c.(\%) = \frac{T_p}{T_r} \times 100\ \% = T_p \times F_r \times 100\ \%. \tag{A.3}$$

The peak power P_{peak} of each pulse can be multiplied by the duty cycle (not in % this time) to achieve the average power P_{avg}:

$$P_{avg} = P_{peak} \times d.c. \tag{A.4}$$

This parameter is crucial in optoacoustic experiments, since it is used it to quantify the amount of power deposited in the absorbers. More important is the energy per pulse E_p that is defined as the ratio between the average power P_{avg} and the repetition rate F_r, but it can also be expressed as the peak power multiplied by the pulse width:

$$E_p = \frac{P_{avg}}{F_r} = P_{peak} \times T_p. \tag{A.5}$$

For the experiments carried out in this dissertation, HPDLs emitting nanosecond optical pulses of high peak power (~ 90 W) and average power of some μJ have been used.

HPDLs are commonly used in many applications as reliable, compact and high luminous sources. Pulsed driving currents with narrow pulses (in the order of ns), high power (generally up to ~ 100 W) and high repetition rates (in the order of kHz) make HPDLs very suited for optoacoustic imaging, spectroscopy and tomography. Additionally, the current pulses should have high quality shapes to fulfill the requirements of optoacoustic signal generation (i.e. $\tau_p < \tau_{th}$ and $\tau_p < \tau_{stress}$).

For these reasons, they require driving circuits based on power MOSFETs that are able to generate high current pulses with short pulse width and rectangular shape. The HPDLs used in this chapter operate with maximum output current and pulse width of 32-35 A and 100 ns, respectively.

Appendix B

Beam combination of high-power diode lasers for optoacoustic endoscopy

B.1. Introduction

The light coupling efficiency of two triplets of HPDLs at 870 nm and 905 nm is experimentally investigated into multimode optical fibers with 200-µm (FT200EMT, Thorlabs Inc., N.A. of 0.39) and 400-µm core diameter (FT400EMT, Thorlabs Inc., N.A. of 0.39), respectively, arranged in hexagonal disposition. These optical fibers are joined to form 7-to-1 round optical fiber bundles featuring a 675-µm and 1.2-mm aperture, respectively. In a second step, the output light of these fiber bundles is coupled into a 600-µm endoscopic fiber, reporting the corresponding coupling efficiencies. As a result, the coupling efficiency of the HPDLs is significantly higher with 400-µm core optical fibers, but at the output of 1.2-mm fiber bundle the coupling into a 600-µm endoscopic fiber is poorer if compared to 675-µm fiber bundle [175]. Fiber bundles with reasonable small core diameter are likely to be used for providing sufficient light energy to potential OAE applications. In this section, it is proposed the use of endoscopic optical fibers with < 1 mm diameter to reduce the invasiveness of the probes within the human body, even though the market offers catheters with larger diameters [176].

B.2. Power measurements

Figure B.1 shows the output of the fiber bundle connected to a power sensor (S120C, Thorlabs) for the measurements of optical average power.

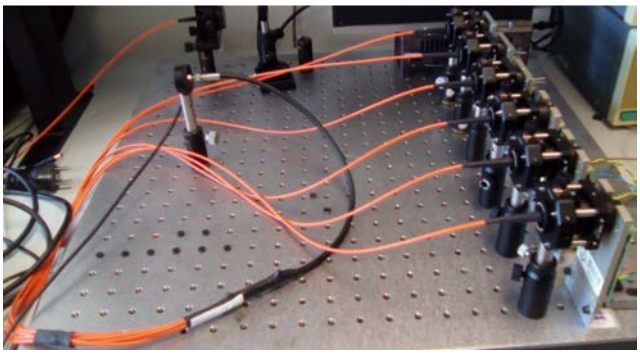

Figure B.1. Output of a fiber bundle connected to a power sensor for power measurements.

In Table B.1, it is reported the average power measured at the output of the fiber bundles when: i) each individual HPDL is coupled into the 200-µm optical fiber, ii) the three HPDLs are coupled simultaneously into the 675-µm fiber bundle, iii) each individual HPDL coupled into the 400-µm optical fiber, and iv) the three HPDLs are coupled simultaneously into the 1.2-mm fiber bundle. These values are

expected to be the sum of the average power from each singular HPDL, but actually they result less (≈ 90 % of the real value) because of the saturation of the power sensor when several sources are applied simultaneously. For this reason the real values, calculated with the sum of the power of the single sources, have been included in parenthesis. The values of average power have only been reported in mean values, whereas the standard deviations have been considered negligible.

Table B.1. Average power of 870-nm and 905-nm HPDLs measured in different steps of the setup.

	Individual average power (mW)	**Combined average power (mW)**	**Individual average power (mW)**	**Combined average power (mW)**
Diode Laser	**200-µm optical fiber**	**675-µm fiber bundle**	**400-µm optical fiber**	**1.2-mm fiber bundle**
HAMAMATSU 870 nm	4.914	14.19 (real: 14.81)	5.944	15.54 (real: 18.01)
	4.944		6.028	
	4.954		6.038	
OSRAM 905 nm	4.900	13.76 (real: 14.90)	5.704	15.59 (real: 17.57)
	4.985		5.900	
	5.010		5.967	

Table B.2 reports the coupling efficiencies of the single HPDLs achieved with 200-µm and 400-µm core optical fibers, achieved in experiments (mean values and standard deviations) and simulations, respectively. As expected, the coupling efficiency is significantly higher with a 400-µm optical fiber.

Table B.2. Coupling efficiencies of 200-µm and 400-µm optical fibers with 870-nm and 905-nm HPDLs.

	Coupling efficiencies			
	200-µm optical fiber		**400-µm optical fiber**	
Diode Laser	**Experiment**	**Simulation**	**Experiment**	**Simulation**
HAMAMATSU 870 nm	66.5 % ± 0.3 %	67.8 %	80.8 % ± 0.7 %	78.7 %
OSRAM 905 nm	64.8 % ± 0.8 %	62.9 %	76.4 % ± 1.8 %	77.4 %

In OAE applications, the output light of the endoscopic probe is delivered within a biological tissue to detect optoacoustic signals in deep tissues or internal vasculature. The next step is to couple the output of the fiber bundles into a 600-µm endoscopic fiber (N.A. = 0.5) and to calculate the coupling efficiencies at 870 nm and 905 nm.

Table B.3. Average power measured at the output of 600-µm fiber probe and corresponding coupling efficiencies at 870 nm and 905 nm.

	Fiber Bundle	**Average power**	**Coupling efficiency**
HAMAMATSU 870 nm	**675-µm**	12.40 mW	87.4 %
	1.2-mm	6.47 mW	41.6 %
OSRAM 905 nm	**675-µm**	11.94 mW	86.8 %
	1.2-mm	6.78 mW	43.5 %

The choice of 600-µm fiber is due to the size restrictions for OAE applications, since the endoscopic probe has to penetrate in depth into biological tissues. Table B.3 reports the average power measured after coupling the 675-µm and 1.2-mm fiber bundles with a 600-µm fiber probe, respectively, and the corresponding coupling efficiencies when two sets of three 870-nm and 905-nm HPDLs are applied.
Although a higher level of average power is coupled into a 1.2-mm fiber bundle (Table B.1), it is much more convenient to use a 675-µm fiber bundle when combining the output light to a 600-µm fiber probe.
In fact, the coupling efficiency is significantly higher by using a 675-µm than a 1.2-mm fiber bundle (Table B.3). However, the choice of the fiber bundle depends on the specific OAE application needed and should take into account a trade-off between efficiency and core diameter of the optical fibers.

Appendix C

Modelling of a lens system for the optical beam focusing of diode laser bars with high fill factor for optoacoustic applications

C.1. Introduction

A customized optical system composed of collimating and focusing lenses is proposed to achieve the beam focusing of high-brightness diode laser bars with high fill factor for optoacoustic applications. Through an optimized design, the beam of a 940-nm diode laser bar is first collimated and symmetrized between the fast and slow axes, and then is reduced in size into a square beam (~ 3.7 mm x 3.7 mm at $1/e^2$ of the peak) with intensity of ~ 3.2 kW/cm^2. In an optoacoustic environment, the optical spot achieved can illuminate a small region of tissue at high intensity to achieve in-depth imaging with high resolution.
High-power diode laser bars (DLBs) and stacks (DLSs) are extensively used in several applications, such as metal welding and soldering [177], surface treatments [171], solar cells fabrication [178], laser surgery [179], molecular and atomic spectroscopy, and military defense [180]. Recently, DLSs at 808 nm have been proposed also for optoacoustic applications [162]. These devices can provide very high values of optical peak power (from hundreds of W to several KW), but they suffer from high divergence of the beam propagated [171] that requires additional optical elements for beam shaping [181]. Industrial applications already have solutions for beam shaping of DLBs and DLSs with fill factor up to 50 % (the fill factor is the ratio between the emitter width and the emitter pitch and is expressed in percentile). Their brightness increases with the fill factor, but their beam gets more complex to handle due to the short distance between emitters. Unfortunately, the market does not offer appropriate lenses to collimate the beam of diode laser devices with fill factor greater than 50 %. In this case the beam collimation is problematic because the array of slow axis collimation (SAC) lenses should be very close to the source, due to the short distance between adjacent emitters that causes a “fast” divergence of the slow axis in short distances. Consequently, there would be not space to include a fast axis collimation (FAC) lens that normally comes first [182-183]. The technical goal is to develop a laser source to illuminate a target at high intensity with a near-square pattern. The approach is to use a high-power DLB with fill factor of 76 % (emitter width and pitch of 190 μm and 250 μm, respectively), taking into account a realistic model of Jenoptik (JDL-BAB-75-37-940-TE-300-1.5) with 37 emitters and radiating in the near-infrared (NIR) at the central wavelength of 940 nm, suitable for OAI [184]. A customized lens design is proposed for this DLB. Collimating and beam focusing lenses have been designed in Zemax environment to reduce the beam size of the abovementioned DLB. In this case, the collimating lenses have not been positioned close to the source but at a certain distance that allows the beam symmetrization between the two axes and the collimation. More specifically, cylindrical FAC and SAC lenses have been positioned at 12 mm and 23 mm from the DLB, respectively. In such a way, the beam is symmetrized and collimated at the same time.

As a result, the beam observed on a detector plane (at 40 mm from the source) shows a semi-square shape (~ 12.35 mm x 11.62 mm) that facilitates its handling in a successive stage. Then, a second pair of crossed cylindrical lenses has been designed to reduce the beam size. Successively, another pair of cylindrical lenses (one plano-concave and the other one plano-convex) is used to reshape the beam in a smaller spot with size of ~ 3.7 mm x 3.7 mm (at $1/e^2$) and intensity of ~ 3.2 kW/cm^2. Due to the large number of emitters, the beam spot could not be reduced more in the slow axis. Basically, the latter lens pair has been designed to achieve a square spot for optoacoustic applications in which a homogeneous beam profile is required for uniform light focusing on an absorbing target.

C.2. Simulations

The beam collimation is shown in Figure C.1 and the optical elements are arranged following the order of the abovementioned description. In Table C.1, the main characteristics of the DLB are reported. The high number of emitters (37) of this bar is responsible for such high output peak power (300 W) but goes to the detriment of the beam quality, due to a higher beam parameter product (*BPP*).

Table C.1. Main characteristics of the DLB. *Quasi-continuous wave

Characteristic	Value
Central wavelength	940 nm
Regime	QCW*
Output peak power	300 W
Fast axis beam divergence ($1/e^2$)	47.5 ± 1.5°
Slow axis beam divergence ($1/e^2$)	10 ± 1°
Single emitter contact width	190 µm
Emitter pitch	250 µm
Number of emitters	37
Fill factor	76%

The characteristics of the collimating lenses are listed in Table C.2. The beam-parameter product (*BPP*) is necessary to estimate the beam quality in both fast and slow axes. In fast axis, it is defined as the waist radius w_{0x} (i.e. the half of the vertical size in fast axis) multiplied by the half angle divergence $\theta_{\perp half}$ of the beam along the fast axis. Instead, in the slow axis it corresponds to the waist radius w_{0y} (which in our case corresponds to the half of the emitter width in slow axis (see Table C.1)) multiplied by the half angle divergence $\theta_{//half}$ of the beam along the slow axis and the number of emitters, normalized to the bar fill factor. Hence, the BPP_s in fast axis and slow axis (BPP_x and BPP_y) are respectively expressed by:

$$BPP_x = w_{0x} \times \theta_{\perp half}, \tag{C.1}$$

$$BPP_y = \frac{w_{0y} \times \theta_{//half} \times \text{number of emitters}}{\text{bar fill factor}}, \tag{C.2}$$

where the bar fill factor is normally expressed in % and is the ratio between the emitter width and the emitter pitch (Table C.1). In order to achieve the necessary beam quality for an efficient fiber coupling,

the BPP ratio (BPP_y/BPP_x) should be made as close as possible to 1 by means of beam shaping lenses. Assuming a vertical size of 2 μm (namely $w_{0x} = 1$ μm) for each emitter, at the output of the DLB, the BPP_s in fast axis (BPP_x) and slow axis (BPP_y) are respectively:

$$BPP_x = 1\ \mu m\ x\ 23.75^\circ \approx 0.41\ \mu m \times rad, \tag{C.3}$$

$$BPP_y = \frac{95\ \mu m\ x\ 5^\circ\ x\ 37\ \text{emitters}}{\text{fill factor}} \approx 403.607\ \mu m \times rad, \tag{C.4}$$

Hence, from Eqs. (C.3) and (C.4) it can be derived that:

$$\frac{BPP_y}{BPP_x} \approx 984.4\ , \tag{C.5}$$

that will be significantly reduced after collimation.

Table C.2. Characteristics of the collimating lenses.

Component	FAC lens	SAC lens
Material	N-LAF21	N-LAF21
Height (mm)	16	16
Thickness (mm)	4.5	3.8
Length (mm)	16	16
Radii of curvature (mm)	Infinite/ 11.1	Infinite/ 70
Conic constant	-1	-1
Distance from DLB (mm)	12	23

Figure C.2 shows more in detail the DLB composed of an array of emitters. It can be noticed how much is short the spacing between adjacent emitters. Even though the slow axis divergence is little (10 ± 1°), the rays of each emitter intersect those of the adjacent emitters at very close distances from the source. The beam profile simulated at 40 mm from the source is represented in Figures C.3 and C.4 as graph and image, respectively. Both the FAC and SAC lenses are plano-convex and their curvature is in the front face of the lenses. As a result, the collimated beam takes a semi-square shape (~ 12.35 mm x 11.62 mm at $1/e^2$ of the peak) that is easier to focus in a successive stage.

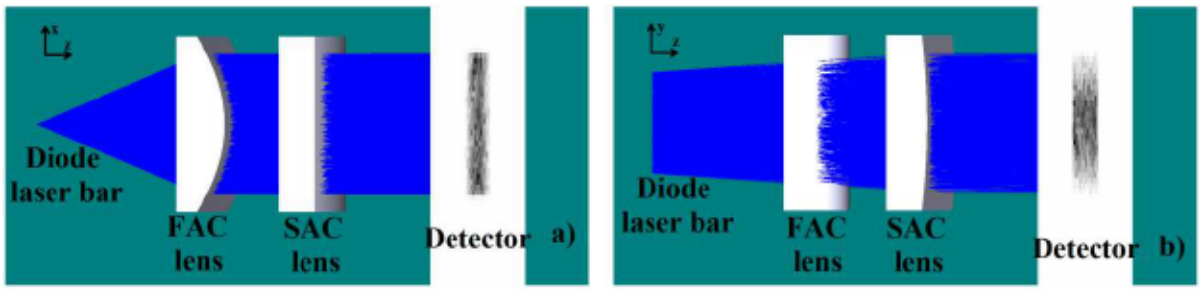

Figure C.1. Simulation scheme of the optical system collimating a DLB from Jenoptik (JDL-BAB-75-37-940-TE-300-1.5) with 37 emitters and 76 % fill factor: lateral view of a) fast axis and b) slow axis. The emitter width and pitch are 190 μm and 250 μm, respectively. The image shows very good collimation in both axes. Actually, the beam is not collimated but keeps a semi-square pattern for a certain distance after the SAC lens (i.e. ~ 88 mm).

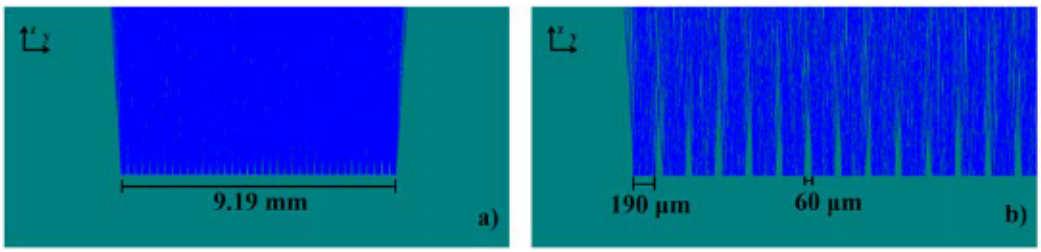

Figure C.2. DLB array of 37 emitters at close distance: a) size of the whole array, b) size of each emitter and pitch.

The detector image shows that the major contribution of power is in the central part of the beam, following the principle of Gaussian beam. In a second step the beam focusing is achieved in a square spot. Normally, in optoacoustic applications is required to focus the beam in a spot to illuminate small regions of biological tissues for in-depth imaging with high resolution. In this regard, the beam size has been reduced in a square spot of ~ 3.7 mm x 3.7 mm (at $1/e^2$) using two additional pairs of cylindrical lenses. The characteristics of these lenses are listed in Table C.3 and they are labeled with their numeration.

Figure C.5 shows the whole lens system including the focusing lenses to reduce the beam spot size. The square spot is captured at a distance of 75 mm from the source (Fig. C.6). The spot size is a square with size of ~ 3.7 mm x 3.7 mm and intensity of ~ 3.2 kW/cm^2 (Figs. C.6 and C.7). At this stage, the values for the two BPP_s have now been nearly symmetrized. The BPP_y has been reduced to 403.607 µm · rad /37 ≈ 10.908 µm · rad, while BPP_x has increased to 0.41 µm · rad x 37 ≈ 15.17 µm · rad. In such a way, it can be derived that:

$$\frac{BPP_x}{BPP_y} \approx 1.39\,, \tag{C.6}$$

which corresponds to a BPP reduction factor of ~ 708. Then, the footprint on the target is reduced by a linear factor of ~37, and the intensity on target is increased by a factor of ~ 37^2 = 1369. The intensity on the detector is limited by the inability to reduce the square footprint below 37 mm in the slow axis. This depends directly on the large value of BPP_y at the output of the DLB. Considering a typical pulse width of 200 ns in optoacoustic applications [185], the intensity of ~ 3.2 kW/cm^2 achieved with the proposed design corresponds to 0.64 mJ/cm^2, which is compatible with the limit of maximum energy density applicable to a biological tissue, which is 20 mJ/cm^2 following ANSI safety standard.

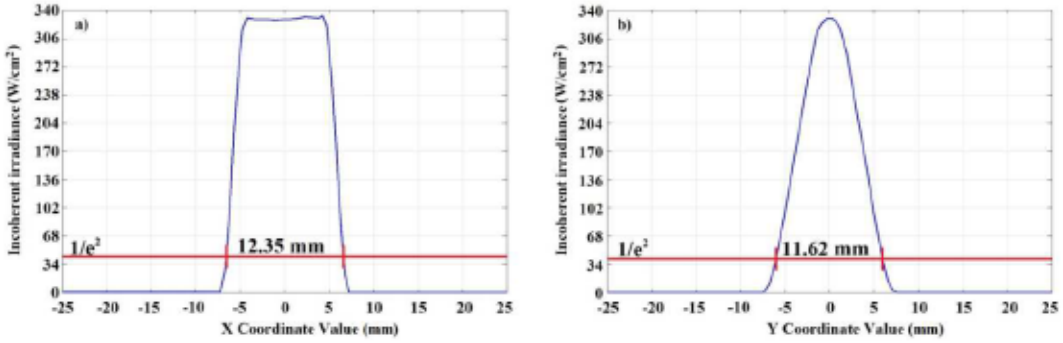

Figure C.3. Profile of the collimated beam in: a) fast axis and b) slow axis. The beam size is ~ 12.35 mm x 11.62 mm at $1/e^2$.

The large number of the emitters, combined with the high fill factor of this DLB, does not allow the beam focusing in a smaller spot that is required in OAE using coupling into optical fibers (< 600 μm), but consents other optoacoustic applications in free space.

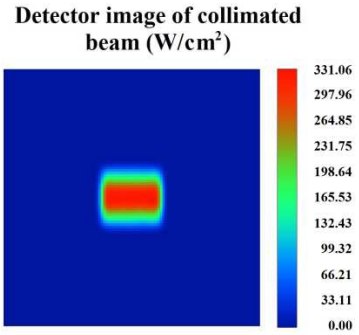

Figure C.4. Image of the beam profile observed on a detector located after collimating lenses.

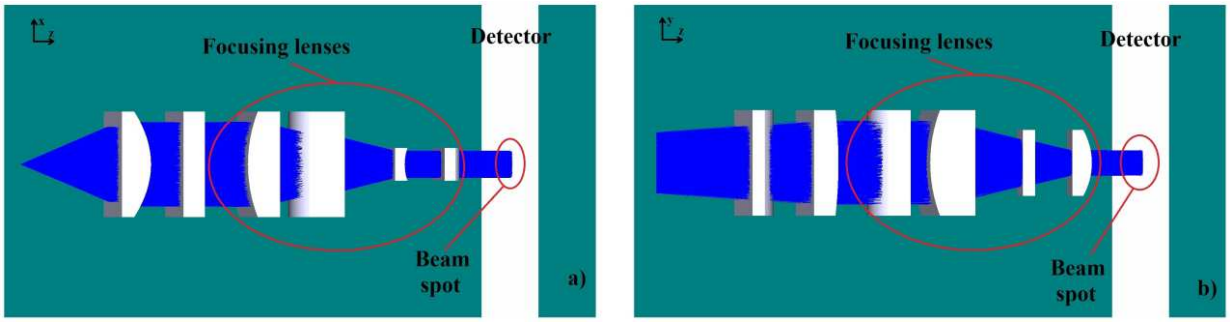

Figure C.5. Whole lens system to reduce the size of the beam spot: a) lateral view, b) top view. At longer distances (i.e. ~ 8 mm from the last focusing lens), the beam divergence would be larger in the slow axis due to the large number of emitters.

Table C.3. Characteristics of each focusing lens for beam size reduction.

Component	Focusing lens 1	Focusing lens 2	Focusing lens 3	Focusing lens 4
Material	S-LAH64	S-LAH64	S-TIH53	S-TIH53
Height (mm)	16	16	5	5
Thickness (mm)	5	7	1.5	3
Length (mm)	16	16	10	10
Radii of curvature (mm)	-21.984/ Infinite	-21.984/ Infinite	Infinite/ -7.5	Infinite/ 10
Conic constant	0	0	0	0
Distance from DLB (mm)	33	41	56.3	64

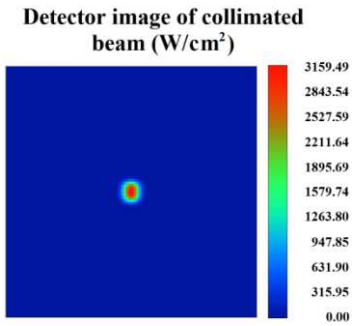

Figure C.6. Image of the beam focused observed on a detector.

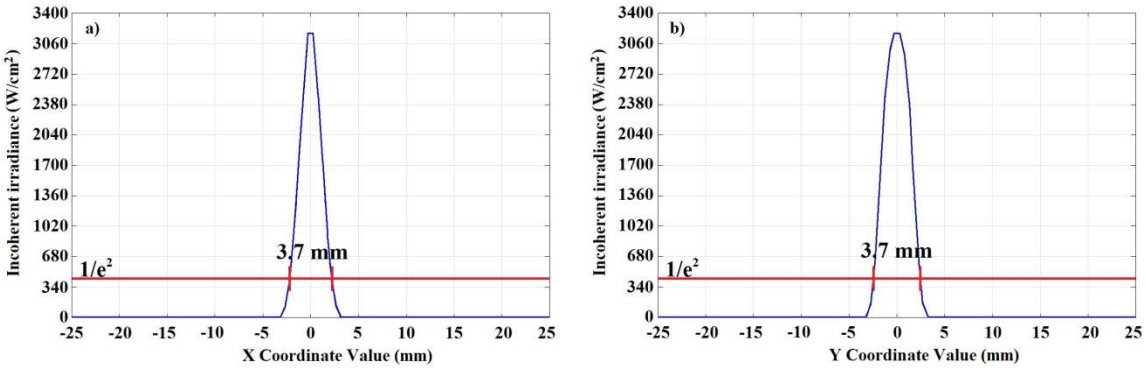

Figure C.7. Beam profile of the focused beam in: a) fast axis and b) slow axis. The beam size is ~ 3.7 x 3.7 mm at $1/e^2$.

List of publications

Journal papers:

[1] L. Leggio, S.B. Gawali, D.C. Gallego, S. Rodríguez, M. Sánchez, G. Carpintero, and H. Lamela, "Optoacoustic response of gold nanorods in soft phantoms using high-power diode laser assemblies at 870 and 905 nm," *Biomedical Optics Express* **8** (#3) pp. 1430-1440 (2017).

[2] M. Sánchez, S. Rodríguez, L. Leggio, S.B. Gawali, D. Gallego, and H. Lamela, "Beam profile improvement of a high-power diode laser stack for optoacoustic applications," *International Journal of Thermophysics* **38** (#48), 10 pages (2017).

[3] L. Leggio, B. Wiśniowski, S.B. Gawali, D. Gallego, M. Sánchez, S. Rodríguez, G. Carpintero, and H, Lamela, "Modelling of a lens system for the optical beam focusing of diode laser bars with high fill factor for optoacoustic applications," *AdvNanoBioM&D* **1** (#2), pp. 115-121 (2017).

[4] L. Leggio, D.C. Gallego, R. Arroyo, S.B. Gawali, S. Rodríguez, M. Sánchez, G. Carpintero, and H. Lamela, "Accurate determination of gold nanorods concentrations from optoacoustic signals detected at 870 nm and 905 nm by using high-power diode lasers with fast switching electronics," *Progress in Electromagnetic Research* (under publication 2017).

[5] L. Leggio, S.B. Gawali, D.C. Gallego, S. Rodríguez, M. Sánchez, G. Carpintero, and H. Lamela, "Determination of gold nanorods concentrations from optoacoustic signals using a three-wavelength hybrid system based on high-power diode lasers and a diode laser bar," *Advanced Nano-Bio-Materials and Devices* **1**(#2), pp. 122-134 (2017).

SPIE Conference Proceedings:

[1] L. Leggio, O. de Varona, P. Escudero, G. Carpintero, M. Osiński, and H. Lamela, "A compact multi-wavelength optoacoustic system based on high-power diode lasers for characterization of double-walled carbon nanotubes (DWCNTs) for biomedical applications," *Proc. of SPIE* **9531**, 953114 (2015).

[2] L. Leggio, O. de Varona, P. Escudero, G. Carpintero, M. Osiński, and H. Lamela, "Improvement of signal-to-noise ratio of optoacoustic signals from double-walled carbon nanotubes by using an array of dual-wavelength high-power diode lasers," *Proc. of SPIE* **9539,** 95390N (2015).

[3] L. Leggio, D.C. Gallego, S.B. Gawali, E. Dadrasnia, M. Sánchez, S. Rodríguez, M. González, G. Carpintero, M. Osiński, and H. Lamela, "Optoacoustic response from graphene-based solutions embedded in optical phantoms by using 905-nm high-power diode-laser assemblies," *Proc. of SPIE* **9708**, 97083M (2016).

[4] L. Leggio, D.C. Gallego, S.B. Gawali, M. Sánchez, S. Rodríguez, M. Osinski, J. Sacher, G. Carpintero, H. Lamela, "System analysis of wavelength beam combining of high-power diode lasers for photoacoustic endoscopy," *Proc. of SPIE* **9888**, 988807 (2016).

[5] S.B. Gawali, L. Leggio, M. Sánchez, S. Rodríguez, E. Dadrasnia, D.C. Gallego, and H. Lamela, "Combining high power diode lasers using fiber bundles for beam delivery in optoacoustic endoscopy applications," *Proc. of SPIE* **9892**, 98921W (2016).

[6] L. Leggio, B. Wiśniowski, S.B. Gawali, S. Rodríguez, M. Sánchez, D. Gallego, G. Carpintero, and H, Lamela, "Multi-wavelength photoacoustic system based on high-power diode laser bars," *Proc. of SPIE* **10064**, 1006441 (2017).

[7] M. Sánchez, S. Rodríguez, SB. Gawali, L. Leggio, D.C. Gallego, and H. Lamela, "Cost-effective optoacoustic system based on the combination of high-power diode lasers," *Proc. of SPIE* **10064**, 100644F (2017).

References

[1] A.G. Bell, "On the production and reproduction of sound by light," *American Journal of Science* **118**, pp. 305-324 (1880).

[2] A.G. Bell, "The production of sound by radiant energy," *Science* **2** (#48), pp. 242-253 (1881).

[3] M.D. Rabasovic, M.G. Nikolic, M.D. Dramicanin, M. Franko, and D.D. Markushev, "Low-cost, portable photoacoustic setup for solid samples," *Measurement Science & Technology* **20** (#9), pp. 1-6 (2009).

[4] A.C. Tam and C.K.N. Patel, "Optical absorptions of light and heavy water by laser optoacoustic spectroscopy," *Applied Optics* **18** (#19), pp. 3348-3358 (1979).

[5] G. Santiago, V. Slezak, and A.L. Peuriot, "Resonant photoacoustic gas sensing by PC-based audio detection," *Applied Physics B - Lasers and Optics* **77** (#4), pp. 463-465 (2003).

[6] F. Bijnen, F. Harren, J. Hackstein, and J. Reuss, "Intracavity CO laser photoacoustic trace gas detection: Cyclic CH4, H2O and CO2 emission by cockroaches and scarab beetles," *Applied Optics* **35** (#27), pp. 5357-5368 (1996).

[7] A.A. Oraevsky, S.L. Jacques, and F.K. Tittel, "Determination of tissue optical properties by piezoelectric detection of laser-induced stress waves," *Proc. of SPIE* **1882**, pp. 86-101 (1993).

[8] L.V. Wang, "Photoacoustic imaging and spectroscopy," *Optical Science and Engineering, CRC Press* (2009).

[9] S. Mallidi, G.P. Luke, and S. Emelianov, "Photoacoustic imaging in cancer detection, diagnosis, and treatment guidance", *Trends in Biotechnology* **29** (#5), pp. 213–221 (2011).

[10] A.A. Oraevsky and A.A. Karabutov, "Optoacoustic tomography," in "*Biomedical Photonics Handbook*," *CRC Press* (2003).

[11] M.H. Xu and L.V. Wang, "Photoacoustic imaging in biomedicine," *Review of Scientific Instruments* **77** (#4), 041101 (2006).

[12] P.C. Beard and B.T. Cox, "Biomedical Photoacoustic Imaging: Theory, Practice and Applications," *John Wiley & Sons* (2017).

[13] P.C. Beard, "Biomedical photoacoustic imaging," *Interface Focus* **1** (#4), pp. 602-631 (2011).

[14] A. Taruttis and V. Ntziachristos, "Advances in real-time multispectral optoacoustic imaging and its applications," *Nature Photon.* **9**, pp. 219-227 (2015).

[15] V. Tuchin, "Tissue Optics: Light Scattering Methods and Instruments for Medical Diagnosis," *III Edition, SPIE Press* (2015).

[16] R. Marbach, T. Koschinsky, F.A. Gries, and H.M. Heise, "Noninvasive blood-glucose assay by near-infrared diffuse-reflectance spectroscopy of the human inner lip," *Applied Spectroscopy* **47** (#7), pp. 875-881 (1993).

[17] I.J. Bigio and J.R. Mourant, "Ultraviolet and visible spectroscopies for tissue diagnostics: fluorescence spectroscopy and elastic-scattering spectroscopy," *Physics in Medicine and Biology* **42** (#5), pp. 803-814 (1997).

[18] A.S. Haka, Z. Volynskaya, J.A. Gardecki, J. Nazemi, R. Shenk, N. Wang, R.R. Dasari, M. Fitzmaurice, and M.S. Feld, "Diagnosing breast cancer using Raman spectroscopy: prospective analysis," *Journal of Biomedical Optics* **14** (#5), 054023 (2009).
[19] J. Laufer, C. Elwell, D. Delpy, and P.C. Beard, "In vitro measurements of absolute blood oxygen saturation using pulsed near-infrared photoacoustic spectroscopy: accuracy and resolution," *Physics in Medicine and Biology* **50** (#18), pp. 4409-4428 (2005).
[20] W.F. Cheong, S.A. Prahl, and A.J. Welch, "A review of the optical-properties of biological tissues," *IEEE Journal of Quantum Electronics* **26** (#12), pp. 2166-2185 (1990).
[21] J. Laufer, D. Delpy, C. Elwell, and P.C. Beard, "Quantitative spatially resolved measurement of tissue chromophore concentrations using photoacoustic spectroscopy: application to the measurement of blood oxygenation and hemoglobin concentration," *Physics in Medicine and Biology* **52** (#1), pp. 141-168 (2007).
[22] F. Bevilacqua, A.J. Berger, A.E. Cerussi, D. Jakubowski, and B.J. Tromberg, "Broadband absorption spectroscopy in turbid media by combined frequency-domain and steady-state methods," *Applied Optics* **39** (#34), pp. 6498-6507 (2000).
[23] B.J. Tromberg, N. Shah, R. Lanning, A. Cerussi, J. Espinoza, T. Pham, L. Svaasand, and J. Butler, "Non-invasive in vivo characterization of breast tumors using photon migration spectroscopy," *Neoplasia* **2**(#1), pp. 26-40 (2000).
[24] T.H. Pham, R. Hornung, H.P. Ha, T. Burney, D. Serna, L. Powell, M. Brenner, and B.J. Tromberg, "Noninvasive monitoring of hemodynamic stress using quantitative near-infrared frequency-domain photon migration spectroscopy," *Journal of Biomedical Optics* **7**(#1), pp. 34-44 (2002).
[25] P. Acedo, A. García, V. Cunningham, H. Lamela, and J.O. Santo Tomás, "Preliminary tests on a low-cost and compact optoelectronic system for optical mammography," *Proc. of SPIE* **5969**, 59691E (2009).
[26] P. Acedo, A. García, V. Cunningham, H. Lamela, and J.O. Santo Tomas, "Conception and description of a low-cost and compact optoelectronic frequency-domain system for optical mammography," *Proc. of SPIE* **5959**, 595903 (2005).
[27] B.J. Tromberg, A. Cerussi, N. Shah, M. Compton, A. Durkin, D. Hsiang, J. Butler, and R. Mehta, "Imaging in breast cancer - Diffuse optics in breast cancer: detecting tumors in pre-menopausal women and monitoring neoadjuvant chemotherapy," *Breast Cancer Research* **7**(#6), pp. 279-285 (2005).
[28] R. Ma, A. Taruttis, V. Ntziachristos, and D. Razansky, "Multispectral optoacoustic tomography (MSOT) scanner for whole-body small animal imaging," *Optics Express* **17** (#24), pp. 21414-21426 (2009).
[29] D. Razansky, M. Distel, C. Vinegoni, R. Ma, N. Perrimon, R.W. Koster, and V. Ntziachristos, "Multispectral optoacoustic tomography of deep-seated fluorescent proteins in vivo," *Nature Photonics* **3** (#7), pp. 412-417 (2009).

[30] S. Mallidi, T. Larson, J. Aaron, K. Sokolov, and S. Emelianov, "Molecular specific optoacoustic imaging with plasmonic nanoparticles," *Optics Express* **15** (#11), pp. 6583-6588 (2007).
[31] A.A. Oraevsky, R.O. Esenaliev, S.L. Jacques, and F.K. Tittel, "Laser optoacoustic tomography for medical diagnostics: Principles," *Proc. of SPIE* **2676**, pp. 22-31 (1996).
[32] R.O. Esenaliev, A.A. Oraevsky, S.L. Jacques, and F.K. Tittel, "Laser optoacoustic tomography for medical diagnostics: Experiments with biological tissues," *Proc. of SPIE* **2676**, pp. 84-90 (1996).
[33] C.H. Li and L.V. Wang, "Photoacoustic tomography and sensing in biomedicine," *Physics in Medicine and Biology* **54** (#19), pp. R59-R97 (2009).
[34] W. Lu, Q. Huang, G. Ku, X. Wen, M. Zhou, D. Guzatov, P. Brecht, R. Su, A.A. Oraevsky, L.V. Wang, and C. Li, "Photoacoustic imaging of living mouse brain vasculature using hollow gold nanospheres," *Biomaterials* **31** (#9), pp. 2617-2626 (2010).
[35] D. Razansky, A. Buehler, and V. Ntziachristos, "Volumetric real-time multispectral optoacoustic tomography of biomarkers," *Nature Protocols* **6**, pp. 1121-1129 (2011).
[36] L.V. Wang and S. Hu, "Photoacoustic tomography: In vivo imaging from organelles to organs," *Science* **335**, pp. 1458-1462 (2012).
[37] J. Xia and L.V. Wang, "Small-animal whole-body photoacoustic tomography: A review," *IEEE Trans. Biomed. Engineering* **61** (#5), pp. 1380-1389 (2014).
[38] M.R. Tomaszewski, I. Quiros-Gonzalez, J. Joseph, and S.E. Bohndiek, "Measurement of changes in blood oxygenation using Multispectral Optoacoustic Tomography (MSOT) allows assessment of tumor development," *Proc. of SPIE* **9708**, 97081F (2016).
[39] M. Mehrmohammadi, S.J. Yoon, D. Yeager, and S.Y. Emelianov, "Photoacoustic imaging for cancer detection and staging," *Curr. Mol. Imaging* **2**(#1). pp. 89-105 (2013).
[40] M. Heijblom, D. Piras, M. Brinkhuis, J.C.G. van Hespen, F.M. van den Engh, M. van der Schaaf, J.M. Klaase, T.G. van Leeuwen, W. Steenbergen, and S. Manohar, "Photoacoustic image patterns of breast carcinoma and comparisons with Magnetic Resonance Imaging and vascular stained histopathology," *Scientific Reports* **5**, 11778 (2015).
[41] J. Tang, J.E. Coleman, X. Dai, and H. Jiang, "Wearable 3-D photoacoustic tomography for functional brain imaging in behaving rats," *Scientific Reports* **6**, 25470 (2016).
[42] A.A. Oraevsky, "3D optoacoustic tomography: From molecular targets in mouse models to functional imaging of breast cancer," *Conference on CLEO Lasers and Electro-Optics,* 14822117 (2014).
[43] S.A. Ermilov, T. Khamapirad, A. Conjusteau, M.H. Leonard, R. Lacewell, K. Mehta, T. Miller, and A.A. Oraevsky, "Laser optoacoustic imaging system for detection of breast cancer," *Journal of Biomedical Optics* **14** (#2), 024007 (2009).
[44] H.P. Brecht, R. Su, M. Fronheiser, S.A. Ermilov, A. Conjusteau, and A.A. Oraevsky, "Whole-body three-dimensional optoacoustic tomography system for small animals," *Journal of Biomedical Optics* **14** (#6), 064007 (2009).

[45] H.P. Brecht, R. Su, M. Fronheiser, S.A. Ermilov, A. Conjusteau, A. Liopo, M. Motamedi, and A.A. Oraevsky, "Optoacoustic 3D whole-body tomography: experiments in nude mice," *Proc. of SPIE* **7177**, 71770E (2009).
[46] A.A. Oraevsky, "Detection, diagnostics and image-guided therapy of cancer using laser optoacoustic imaging system and gold nanoparticles," *APBP 2004: Second Asian and Pacific Rim Symposium on Biophotonics*, pp. 250-251 (2004).
[47] J.A. Copland, M. Eghtedari, V.L. Popov, N. Kotov, N. Mamedova, M. Motamedi, and A.A. Oraevsky, "Bioconjugated gold nanoparticles as a molecular based contrast agent: implications for imaging of deep tumors using optoacoustic tomography," *Molecular Imaging & Biology* **6** (#5), pp. 341-349 (2004).
[48] A.V. Liopo, R. Su, and A.A. Oraevsky, "Melanin nanoparticles as a novel contrast agent for optoacoustic tomography," *Photoacoustics* **3**, pp. 35-43 (2015).
[49] A.B.E. Attia, G. Balasundaram, W. Driessen, V. Ntziachristos, and M. Olivo, "Phthalocyanine photosensitizers as contrast agents for *in vivo* photoacoustic tumor imaging," *Biomed. Opt. Express* **6** (#2), pp. 591-598 (2015).
[50] H. Lamela, V. Cunningham, P. Pedreira, D.C. Gallego, P. Acedo, W. Fritzsche, A. Csaki, G. Festag, and A. Steinbruk, "Comparative analysis of optical absorption and optoacoustic signal generation in nanoparticles," *Proc. of SPIE* **6856**, 68560L (2008).
[51] H. Lamela, V. Cunningham, P. Pedreira, D.C. Gallego, P. Acedo, W. Fritzsche, A. Csaki, G. Festag, and A. Steinbruk, "Analysis of the diffuse light and optoacoustic signal generation in nanoparticles," *Proc. of SPIE* **7022**, 702207 (2007).
[52] V. Cunningham, H. Lamela, P. Pedreira, D. Gallego, P. Acedo, W. Fritzsche, A. Csaki, G. Festag, and A. Steinbruk, "Optoacoustic signal generation by using nanoparticles and nanorods for biomedical imaging," *The 2nd International Topical Meeting on Optical Sensing and Artifical Vision, OSAV 2008* (2008).
[53] M. Eghtedari, A.A. Oraevsky, J.A. Copland, N.A. Kotov, A. Conjusteau, and M. Motamedi, "High sensitivity of in vivo detection of gold nanorods using a laser optoacoustic imaging system," *Nano Letters* **7 (#7)**, pp. 1914-1918 (2007).
[54] K.H. Song, C. Kim, K. Maslov, and L.V. Wang, "Noninvasive in vivo spectroscopic nanorod-contrast photoacoustic mapping of sentinel lymph nodes," *European Journal of Radiology* **70** (#2), pp. 227-231 (2009).
[55] A. Taruttis, E. Herzog, D. Razansky, and V. Ntziachristos, "Real-time imaging of cardiovascular dynamics and circulating gold nanorods with multispectral optoacoustic tomography," *Optics Express* **18** (#19), pp. 19592-19602 (2010).
[56] Z.M. Zhao and R. Myllylä, "The effects of optical scattering on pulsed photoacoustic measurement in weakly absorbing liquids," *Meas. Sci. Technol.* **12**, pp. 2172-2177 (2001).
[57] R.G.M. Kolkman, W. Steenbergen, and T. G. van Leeuwen, "In vivo photoacoustic imaging of blood vessels with a pulsed laser diode," *Lasers Med. Sci.* **21** (#3), pp. 134-139 (2006).
[58] T.J. Allen and P.C. Beard, "Pulsed near-infrared laser diode excitation system for biomedical photoacoustic imaging," *Optics Letters* **31** (#23), pp. 3462-3464 (2006).

[59] T.J. Allen and P.C. Beard, "Dual wavelength laser diode excitation source for 2D photoacoustic imaging," *Proc. of SPIE* **6437**, 64371U (2007).
[60] K. Maslov and L.V. Wang, "Photoacoustic imaging of biological tissue with intensity-modulated continuous-wave laser," *Journal of Biomedical Optics* **13** (#2), 024006 (2008).
[61] L.M. Zeng, G.D. Liu, D.W. Yang, and X.R. Ji, "Portable optical-resolution photoacoustic microscopy with a pulsed laser diode excitation," *Appl. Phys. Lett.* **102** (#5), 053704 (2013).
[62] T.H. Wang, S. Nandy, H.S. Salehi, P.D. Kumavor, and Q. Zhu, "A low-cost photoacoustic microscopy system with a laser diode excitation," *Biomed. Opt. Express* **5** (#9), pp. 3053-3058 (2014).
[63] V. Cunningham and H. Lamela, "Efficient combination of multiple high power semiconductor laser sources for photoacoustic signal generation in biomedical phantoms," *Proc. of SPIE* **6191**, 619106 (2006).
[64] L. Leggio, D.C. Gallego, S.B. Gawali, E. Dadrasnia, M. Sánchez, S. Rodríguez, M. González, G. Carpintero, M. Osiński, and H. Lamela, "Optoacoustic response from graphene-based solutions embedded in optical phantoms by using 905-nm high-power diode-laser assemblies," *Proc. of SPIE* **9708**, 97083M (2016).
[65] L.M. Zeng, G.D. Liu, D.W. Yang, and X.R. Ji, "3D-visual laser-diode-based photoacoustic imaging," *Optics Express* **20** (#2), pp. 1237-1246 (2012).
[66] K. Daoudi, P.J. van den Berg, O. Rabot, A. Kohl, S. Tisserand, P. Brands, and W. Steenbergen, "Handheld probe integrating laser diode and ultrasound transducer array for ultrasound/photoacoustic dual modality imaging," *Opt. Express* **22** (#21), pp. 26365- 26374 (2014).
[67] C.-S. Friedrich, M.P. Mienkina, C. Brenner, N.C. Gerhardt, M. Jörger, A. Strauß, M.F. Beckmann, G. Schmitz, and M.R. Hofmann, "Photoacoustic blood oxygenation imaging based on semiconductor lasers," *Photon. & Optoelectron.* **1** (#3), pp. 48-54 (2012).
[68] M.F. Beckmann, B.S. Gutrath, A. Buchkremer, T. Eckert, J. Timper, A. Leifert, W. Richtering, U. Simon, and G. Schmitz, "Size dependent photoacoustic signal response of gold nanoparticles using a multispectral laser diode system," *Proc. IEEE International Ultrasonics Symp.*, pp. 2336-2339 (2012).
[69] J.M. Yang, C. Favazza, R. Chen, J. Yao, X. Cai, K. Maslov, Q. Zhou, K.K. Shung, and L.V. Wang, "Toward dual wavelength functional photoacoustic endoscopy: laser and peripheral optical systems development," *Proc. of SPIE* **8223**, 822316 (2012).
[70] J.M. Yang, K. Maslov, H.C. Yang, Q. Zhou, K.K. Shung, and L.V. Wang, "Photoacoustic endoscopy," *Optics Letters* **34** (#10), pp. 1591-1593 (2009).
[71] J.-M. Yang, C. Favazza, R. Chen, J. Yao, X. Cai, K. Maslov, Q. Zhou, K.K. Shung, and LV. Wang, "Simultaneous functional photoacoustic and ultrasonic endoscopy of internal organs in vivo," *Nature Medicine* **18**, pp. 1297-1302 (2012).
[72] T.-J. Yoon and Y.-S. Cho, "Recent advances in photoacoustic endoscopy," *World Journal of Gastrointestinal Endoscopy* **5** (#11), pp. 534-539 (2013).

[73] J.-M. Yang, R. Chen, C. Favazza, J. Yao, C. Li, Z. Hu, Q. Zhou, K.K. Shung, and L.V. Wang, "A 2.5-mm diameter probe for photoacoustic and ultrasonic endoscopy," *Optics Express* **20** (#21), pp. 23944-23953 (2012).
[74] S. Tang, J. Chen, P. Samant, S. Kelly, and L. Xiang, "Transurethral photoacoustic endoscopy for prostate cancer: a simulation study," *IEEE Transactions on Medical Imaging* **35** (#7), pp.1780-1787 (2016).
[75] K. Jansen, M. Wu, A.F. Van der Steen, and G. van Soest, "Lipid detection in atherosclerotic human coronaries by spectroscopic intravascular photoacoustic imaging," *Optics Express* **21** (# 18), pp. 21472-84 (2013).
[76] K. Jansen, A.F. van der Steen, M. Wu, H.M. van Beusekom, G. Springeling, X. Li, Q. Zhou, K.K. Shung, D.P. de Kleijn, and G. van Soest, "Spectroscopic intravascular photoacoustic imaging of lipids in atherosclerosis," *Journal of Biomedical Optics* **19** (# 2), 026006 (2014).
[77] R. Ansari, E. Zhang, S. Mathews, A.E. Desjardins, and P.C. Beard, "Photoacoustic endoscopy probe using a coherent fibre-optic bundle," *SPIE/OSA European Conference on Biomedical Optics*, 953905 (2015).
[78] K. Jansen, A.F. van der Steen, H.M. van Beusekom, J. Oosterhuis, and G. van Soest, "Intravascular photoacoustic imaging of human coronary atherosclerosis," *Optics Letters* **36** (# 5), pp. 597-599 (2011).
[79] L.V. Wang and H.I. Wu, "Biomedical optics: principles and imaging," *New Jersey: John Wiley & Sons* (2007).
[80] V. Cunningham (Doctoral thesis), "New optoacoustic spectroscopy system to quantify and characterize absorbers in turbid media. Experimental measurements and analysis of gold nanoparticles for biomedical applications," *UC3M* (2010).
[81] W.M. Star, "Diffusion theory of light transport," in *Optical-Thermal Response of Laser-Irradiated Tissue*, *Springer Netherlands*, pp. 131-206 (2011).
[82] S.Y. Emelianov, S.R. Aglyamov, A.B. Karpiouk, S. Mallidi, S. Park, S. Sethuraman, J. Shah, R.W. Smalling, J.M. Rubin, and W.G. Scott, "1E-5 synergy and applications of combined ultrasound, elasticity, and photoacoustic imaging," *IEEE Ultrasonics Symposium* **1-5**, pp. 405-415 (2006).
[83] T. Vo-Dinh, "Biomedical photonics," *CRC Press* (2003).
[84] J.M. Conway, K.H. Norris, and C.E. Bodwell, "A new approach for the estimation of body composition: infrared interactance," *American Journal of Clinical Nutrition* **40** (#6), pp. 1123-1130 (1984).
[85] D.C. Gallego (Doctoral thesis), "High sensitivity interferometric sensors for optoacoustic imaging in biomedical applications," *UC3M* (2016).
[86] V.Ė. Gusev and A.A. Karabutov, "Laser optoacoustics," *American Institute of Physics* (1993).
[87] T.J. Allen, B.T. Cox, and P.C. Beard, "Generating photoacoustic signals using high-peak power pulsed laser diodes," *Proc. of SPIE* **5697**, pp. 233-242 (2005).

[88] R.O. Esenaliev, A.A. Karabutov, and A.A. Oraevsky, "Sensitivity of laser opto-acoustic imaging in detection of small deeply embedded tumors," *IEEE Journal on Selected Topics in Quantum Electronics* **5** (#4), pp. 981-988 (1999).
[89] C.A. Di Marzio, and T.W. Murray, "Medical imaging techniques combining light and ultrasound," *Subsurface Sensing Technologies and Applications* **4** (#4), pp. 289-309 (2003).
[90] A.A. Oraevsky, S.L. Jacques, and F.K. Tittel, "Measurement of tissue optical properties by time-resolved detection of laser-induced transient stress," *Applied Optics* **36** (#1), pp. 402-415 (1997).
[91] S. Kumar, and V. Singh, "Pseudo-Grüneisen parameter of organic liquids," *Indian journal of pure & applied physics* **30** (#3), pp. 89-93 (1992).
[92] M. Xu, and L.V. Wang, "Pulsed-microwave-induced thermoacoustic tomography: filtered backprojection in a circular measurement configuration," *Medical Physics* **29** (#8), pp. 1661-1669 (2002).
[93] A.A. Oraevsky and A.A. Karabutov, "Ultimate sensitivity of time-resolved optoacoustic detection," *Proc. of SPIE* **3916,** pp. 228-239 (2000).
[94] L.V. Wang, "Tutorial on photoacoustic microscopy and computed tomography," *IEEE Journal of Selected Topics in Quantum Electronics* **14** (#1), pp. 171-179 (2008).
[95] K. Sun, X. Chen, W. Chai, X. Fei, C. Fu, X. Yan, Y. Zhan, K. Chen, K. Shen, and F. Yan, "Breast cancer: diffusion Kurtosis MR imaging-diagnostic accuracy and correlation with clinical-pathologic factors," *RSNA Radiology* **277** (#1), pp. 46-55 (2015).
[96] D. Razansky, N.C. Deliolanis, C. Vinegoni, and V. Ntziachristos, "Deep tissue optical and optoacoustic molecular imaging technologies for pre-clinical research and drug discovery," *Current Pharmaceutical Biotechnology* **13** (#4), pp. 504-522 (2012).
[97] G.P. Luke, D. Yeager, and S.Y. Emelianov, "Biomedical applications of photoacoustic imaging with exogenous contrast agents," *Annals of Biomedical Engineering* **40** (#2), pp. 422-437 (2012).
[98] C. Kim, C. Favazza, and L.V. Wang, "In vivo photoacoustic tomography of chemicals: high-resolution functional and molecular optical imaging at new depths," *Chemical Reviews* **110** (#5), pp. 2756-2782 (2010).
[99] A.A. Oraevsky, "Gold and silver nanoparticles as contrast agents for optoacoustic tomography," in *Photoacoustic imaging and spectroscopy*, *L. Wang (Ed.), CRC Press*, pp. 373–386 (2009).
[100] S. Ijima, "Helical microtubules of graphitic carbon," *Nature* **354**, pp. 56–58 (1991).
[101] M.S. Dresselhaus, "Fullerenes: Down the straight and narrow," *Nature* **358**, pp. 195–196 (1992).
[102] M.S. Dresselhaus, G. Dresselhaus, and P.C. Eklund, "Science of Fullerenes and Carbon Nanotubes," *Academic Press Elsevier* (1996).
[103] http://www.lbl.gov

[104] R. Alshehri, A.M. Ilyas, A. Hasan, A. Arnaout, F. Ahmed, and A. Memic, "Carbon nanotubes in biomedical applications: factors, mechanisms, and remedies of toxicity," *Journal of Medicinal Chemistry* **59** (#18), pp. 8149–8167 (2016).
[105] R. Zhang, Y. Zhang, Q. Zhang, H. Xie, W. Qian, and F. Wei, "Growth of half-meter long carbon nanotubes based on Schulz–Flory distribution," *ACS Nano* **7** (#7), pp. 6156–61 (2013).
[106] X. Wang, Q. Li, J. Xie, Z. Jin, J. Wang, Y. Li, K. Jiang and S. Fan, "Fabrication of ultralong and electrically uniform single-walled carbon nanotubes on clean substrates," *Nano Letters* **9** (#9), pp. 3137–41 (2009).
[107] T. Zhang and H. Cui, "Carbon nanoparticles in photoacoustic imaging," *SPIE Press Spotlight SL04* (2015).
[108] S. Zanganeh, H. Li, P.D. Kumavor, U. Alqasemi, A. Aguirre, I. Mohammad, C. Stanford, M.B. Smith, and Q. Zhu, "Photoacoustic imaging enhanced by indocyanine green-conjugated single-wall carbon nanotubes," *Journal of Biomedical Optics* **18** (#9), 096006 (2013).
[109] H. Cui, C. Hong, A. Ying, X. Yang, and S. Ren, "Ultrathin gold nanowire-functionalized carbon nanotubes for hybrid molecular sensing," *ACS Nano* **7** (#9), pp. 7805–7811 (2013).
[110] R.M. Pramanik, K.H. Song, M. Swierczewska, D. Green, B. Sitharaman, and L.V. Wang, "In vivo carbon nanotube-enhanced non-invasive photoacoustic mapping of the sentinel lymph node," *Physics in Medicine and Biology* **54** (#11), pp. 3291–3301 (2009).
[111] L. Xiang, Y. Yuan, D. Xing, Z. Ou, S. Yang, and F. Zhou, "Photoacoustic molecular imaging with antibody-functionalized single-walled carbon nanotubes for early diagnosis of tumor," *Journal of Biomedical Optics* **14** (#2), 021008 (2009).
[112] J.-W. Kim, E.I. Galanzha, E.V. Shashkov, H.-M. Moon, and V.P. Zharov, "Golden carbon nanotubes as multimodal photoacoustic and photothermal high-contrast molecular agents," *Nature Nanotechnology* **4** (#10), pp. 688-694 (2009).
[113] F. Zhou, S. Wu, Y. Yuan, W.R. Chen, and D. Xing, "Mitochondria-targeting photoacoustic therapy using single-walled carbon nanotubes," *Small* **8** (#10), pp. 1543-50 (2012).
[114] P. You, Y. Yang, M. Wang, X. Huang, and X. Huang, "Graphene oxide-based nanocarriers for cancer imaging and drug delivery," *Current Pharmaceutical Design* **21** (#22), pp. 3215-22 (2015).
[115] Y. Yang, A.M. Asiri, Z. Tang, D. Du, and Y. Lin, "Graphene based materials for biomedical applications," *Materials Today* **16** (#10), pp. 365-373 (2013).
[116] N. Rahmanian, M. Eskandani, J. Barar, and Y. Omidi, "Recent trends in targeted therapy of cancer using graphene oxide-modified multifunctional nanomedicines," *Journal of Drug Targeting* **25** (#3), pp. 202-215 (2017).
[117] M. Nasrollahzadeh, F. Babaei, P. Fakhri, and B. Jaleh, "Synthesis, characterization, structural, optical properties and catalytic activity of reduced graphene oxide/copper nanocomposites," *RSC Advances Issue* **5** (#14), pp. 10782–10789 (2015).
[118] J.L. Hammond, N. Formisano, P. Estrela, S. Carrara, and J. Tkac, "Electrochemical bio-sensors and nanobiosensors," *Essays in Biochemistry* **60** (#1), pp.69-80 (2016).

[119] I. Khalil, N.M. Julkapli, W.A. Yehye, W.J. Basirun, and S.K. Bhargava, “Graphene–gold nanoparticles hybrid-synthesis, functionalization, and application in an electrochemical and surface-enhanced Raman scattering biosensor,” *Materials* **9** (#6), 38 pages (2016).
[120] S. Gurunathan, J.W. Han, V. Eppakayala, and J.H. Kim, “Green synthesis of graphene and its cytotoxic effects in human breast cancer cells,” *International Journal of Nanomedicine* **8**, pp. 1015-1027 (2013).
[121] B. Book Newell, Y. Wang, and J. Irudayaraj, “Multifunctional gold nanorod theragnostics probed by multi-photon imaging,” *European Journal of Medicinal Chemistry* **48**, pp. 330-337 (2012).
[122] O. Betzer, R. Ankri, M. Motiei, and R. Popovtzer, “Theranostic approach for cancer treatment: multifunctional gold nanorods for optical imaging and photothermal therapy,” *Journal of Nanomaterials*, 7 pages (2015).
[123] B. Buckway, N. Frazier, A.J. Gormley, A. Ray, and H. Ghandehari, “Gold nanorod-mediated hyperthermia enhances the efficacy of HPMA copolymer-90Y conjugates in treatment of prostate tumors,” *Nuclear Medicine and Biology* **41** (#3), pp. 282-289 (2014).
[124] Z. Ma, H. Xia, Y. Liu, B. Liu, W. Chen, and Y. Zhao, “Applications of gold nanorods in biomedical imaging and related fields,” *Chinese Science Bulletin* **58** (#21), pp. 2530–2536 (2013).
[125] G. Mie, “A contribution to the optics of turbid media, especially colloidal metallic suspensions,” *Annals of Physics* **25** (#3), pp. 377-445 (1908).
[126] A.M. Alkilany, L.B. Thompson, S.P. Boulos, P.N. Sisco, and C.J. Murphy, “Gold nanorods: their potential for photothermal therapeutics and drug delivery, tempered by the complexity of their biological interactions,” *Advanced Drug Delivery Reviews* **64** (#2), pp. 190-199 (2012).
[127] https://www.nanopartz.com/
[128] L. Rayleigh (John Strutt), “On the scattering of light by small particles," *Philosophical Magazine* **4** (#41), pp. 447-457 (1871).
[129] S. Link, M.B. Mohamed, and M.A. El-Sayed, “Simulation of the optical absorption spectra of gold nanorods as a function of their aspect ratio and the effect of the medium dielectric constant,” *Journal of Physical Chemistry B* **103** (#16), pp. 3073-3077 (1999).
[130] B.M.I. van der Zande, L. Pages, R.A.M. Hikmet, and A. van Blaaderen, “Optical properties of aligned rod-shaped gold particles dispersed in poly(vinyl alcohol) films,” *Journal of Physical Chemistry B* **103** (#28), pp. 5761-5767 (1999).
[131] E.M. Purcell and C. Pennypacker, “Scattering and absorption of light by nonspherical dielectric grains,” *Astrophysical Journal* **186** (#2), pp. 705-714 (1973).
[132] J. Nelayah, M. Kociak, O. Stephan, N. Geuquet, L. Henrard, F.J.G. de Abajo, I. Pastoriza-Santos, L.M. Liz-Marzan, and C. Colliex, “Two-dimensional quasistatic stationary short range surface plasmons in flat nanoprisms,” *Nano Letters* **10** (#3), pp. 902-907 (2010).
[133] E. Hao, G.C. Schatz, and J.T. Hupp, “Synthesis and optical properties of anisotropic metal nanoparticles,” *Journal of Fluorescence* **14** (#4), pp. 331-341 (2004).

[134] J.H. Weaver and H.P.R. Frederikse, "Optical properties of selected elements," *in CRC Hanbook of Chemistry and Physics, CRC Press*, pp. 12-123 (2009).
[135] P.B. Johnson, and R.W. Christy, "Optical - constants of noble-metals," *Physical Review B*, 6 (#12), pp. 4370-4379 (1972).
[136] X. Yang, E.W. Stein, S. Ashkenazi, and L.V. Wang, "Nanoparticles for photoacoustic imaging," *Wiley Interdisciplinary Reviews: Nanomedicine and Nanobiotechnology* **1** (#4), pp. 360-368 (2009).
[137] M. Eghtedari, A.A. Oraevsky, J.A. Copland, N.A. Kotov, A. Conjusteau, and M. Motamedi, "High sensitivity of in vivo detection of gold nanorods using a laser optoacoustic imaging system," *Nano Letters* **7** (#7), pp. 1914-1918 (2007).
[138] M. Eghtedari, A.V. Liopo, J.A. Copland, A.A. Oraevsky, and M. Motamedi, "Engineering of hetero-functional gold nanorods for the in vivo molecular targeting of breast cancer cells," *Nano Letters* **9** (#1), pp. 287-91 (2009).
[139] Y.-S. Chen, W. Frey, S. Kim, P. Kruizinga, K. Homan, and S. Emelianov, "Silica-coated gold nanorods as photoacoustic signal nanoamplifiers," *Nano Letters* **11** (#2), pp. 348–354 (2011).
[140] J.R. Cook, R.R. Bouchard, and S.Y. Emelianov, "Tissue-mimicking phantoms for photoacoustic and ultrasonic imaging," *Biomedical Optics Express* **2** (#11), pp. 3193-3206 (2011).
[141] Z. Xu, C. Li, and L.V. Wang, "Photoacoustic tomography of water in phantoms and tissue," *Journal of Biomedical Optics* **15** (#3), 036019 (2010).
[142] L. Leggio, O. de Varona, P. Escudero, G. Carpintero, M. Osiński, and H. Lamela, "A compact multi-wavelength optoacoustic system based on high-power diode lasers for characterization of double-walled carbon nanotubes (DWCNTs) for biomedical applications," *Proc. of SPIE* **9531**, 953114 (2015).
[143] L.Z. Feng and Z. Liu, "Graphene in biomedicine: opportunities and challenges," *Nanomedicine* **6** (#2), pp. 317-324 (2011).
[144] Y. Wang, Z.H. Li, J. Wang, J.H. Li, and Y.H. Lin, "Graphene and graphene oxide: biofunctionalization and applications in biotechnology," *Trends in Biotechnology* **29** (#5), pp. 205-212 (2011).
[145] H. Shen, L.M. Zhang, M. Liu, and Z.J. Zhang, "Biomedical applications of graphene," *Theranostics* **2** (#3), pp. 283-294 (2012).
[146] H.Y. Mao, S. Laurent, W. Chen, O. Akhavan, M. Imani, A.A. Ashkarran, and M. Mahmoudi, "Graphene: promises, facts, opportunities, and challenges in nanomedicine," *Chemical Review* **113** (#5), pp. 3407-3424 (2013).
[147] J.H. Chen, R.Q. Lin, H.N. Wang, J. Meng, H.R. Zheng, and L. Song, "Blind-deconvolution optical-resolution photoacoustic microscopy in vivo," *Optics Express* **21** (#6), pp. 7316-7327 (2013).
[148] M.A. Patel, H. Yang, P.L. Chiu, D.D.T. Mastrogiovanni, C.R. Flach, K. Savaram, L. Gomez, A. Hemnarine, R. Mendelsohn, E. Garfunkel, H.B. Jiang, and H.X. He, "Direct

production of graphene nanosheets for near infrared photoacoustic imaging," *ACS Nano* **7** (#9), pp. 8147-8157 (2013).
[149] G. Lalwani, X. Cai, L.M. Nie, L.V. Wang, and B. Sitharaman, "Graphene-based contrast agents for photoacoustic and thermoacoustic tomography," *Photoacoustics* **1** (#3-4), pp. 62-67 (2013).
[150] D. Wu, L. Huang, M.S. Jiang, and H.B. Jiang, "Contrast agents for photoacoustic and thermoacoustic imaging: A review," *Int. J. Mol. Sci.* **15** (#12), pp. 23616-23639 (2014).
[151] H.W. Moon, D. Kumar, H.M. Kim, C. B. Sim, J.-H. Chang, J.-M. Kim, H. C. Kim, and D.-K. Lim, "Amplified photoacoustic performance and enhanced photothermal stability of reduced graphene oxide coated gold nanorods for sensitive photoacoustic imaging," *ACS Nano* **9** (#3), pp. 2711-2719 (2015).
[152] W. Li and X. Chen, "Gold nanoparticles for photoacoustic imaging," *Nanomedicine* **10** (#2), pp. 299-320 (2015).
[153] S.L. Jacques, "Corrigendum: optical properties of biological tissues: a review," *Physics in Medicine and Biology* **58** (#11), pp. 5007-5008 (2013).
[154] J.G. Laufer, B. Cox, E. Zhang, and P.C. Beard, "Quantitative determination of chromophore concentrations from 2D photoacoustic images using a nonlinear model-based inversion scheme," *Applied Optics* **49** (#8), pp. 1219-33 (2010).
[155] B. Cox, J.G. Laufer, S. Arridge, and P.C. Beard, "Quantitative spectroscopic photoacoustic imaging: a review," *Journal of Biomedical Optics* **17** (#6), 061202 (2012).
[156] http://www.microchip.com
[157] X. Huang and M.A. El-Sayed, "Gold nanoparticles: optical properties and implementations in cancer diagnosis and photothermal therapy," *Journal of Advanced Research* **1** (#1), pp. 13–28 (2010).
[158] J. Kim, S. Park, J. E. Lee, S. M. Jin, J. H. Lee, I. S. Lee, I. Yang, J.-S. Kim, S. K. Kim, M.-H. Cho, and T. Hyeon, "Designed fabrication of multifunctional magnetic gold nanoshells and their application to magnetic resonance imaging and photothermal therapy," *Angew. Chem. Int. Ed. Engl.* **45** (#46), pp. 7754–7758 (2006).
[159] A.W. Lin, N.A. Lewinski, J.L. West, N.J. Halas, and R.A. Drezek, "Optically tunable nanoparticle contrast agents for early contrast agents for early cancer detection: model-based analysis of gold nanoshells," *Journal of Biomedical Optics* **10** (#6), 064035 (2005).
[160] V. Cunningham, H. Lamela, and D. C. Gallego, "Laser optoacoustic scheme for highly accurate characterization of gold nanostructures in liquid phantoms for biomedical applications", *Journal of Nanophotonics* **7** (#1), 073078 (2013).
[161] https://www.rp-photonics.com/m2_factor.html
[162] M. Sánchez, S. Rodríguez, L. Leggio, S.B. Gawali, D. Gallego, and H. Lamela, "Beam profile improvement of a high-power diode laser stack for optoacoustic applications," *International Journal of Thermophysics*, 38 (#48), 10 pages (2017).
[163] ISO/DIS-Standard 11 146, International Organization for Standardization.

[164] F.Z. Fang, Z. Xiong, and X.T. Hu, "Ultra-precision machining of reflector array for laser diode beam shaping," *Optoelectronics Letters* **3** (#2), pp. 141-143 (2007).
[165] P. Loosen and A. Knitsch, "Incoherent beam superposition and stacking," in *High power diode lasers: technology and applications, (Editors: F. Bachmann, P. Loosen, and R. Poprawe) Springer,* pp. 121-179 (2007).
[166] L. Leggio, B. Wiśniowski, S.B. Gawali, S. Rodríguez, M. Sánchez, D. Gallego, G. Carpintero, and H, Lamela, "Multi-wavelength photoacoustic system based on high-power diode laser bars," *Proc. of SPIE* **10064**, 1006441 (2017).
[167] www.limo.de/en/products-and-solutions/mikrooptik/beam-transformation-system
[168] https://www.edmundoptics.com/optics/laser-optics/laser-lenses/400m-pitch-24-emitter-beam-twister
[169] J. Yu, L. Guo, H. Wu, Z. Wang, S. Gao, and D. Wu, "Optimization of beam transformation systems for diode laser bars," *Optics Express* **24** (#17), pp. 19728-19735 (2016).
[170] A. Yariv, "Quantum electronics," *III Edition, New Jersey: John Wiley & Sons* (1985).
[171] M. Behringer, G. Erbert, and R. März, "High-power diode laser technology and characteristics" in *High power diode lasers: technology and applications (Editors: F. Bachmann, P. Loosen, and R. Poprawe) Springer,* pp. 5-74 (2007).
[172] L.A. Coldren, S.W. Corzine, and M.L. Mashanovitch, "Diode lasers and photonic integrated circuits," *II Edition, New Jersey: John Wiley & Sons* (2012).
[173] M. Born and E. Wolf, "Principles of optics. Electromagnetic theory of propagation, interference and diffraction of light," *Pergamon Press Oxford* (1964).
[174] K. Duan and B. Lü, "Propagation properties of vectorial elliptical Gaussian beams beyond the paraxial approximation," *Optics & Laser Technology* **36** (#6), pp. 489–496 (2004).
[175] S.B. Gawali, L. Leggio, M. Sánchez, S. Rodríguez, E. Dadrasnia, D.C. Gallego, and H. Lamela, "Combining high power diode lasers using fiber bundles for beam delivery in optoacoustic endoscopy applications," *Proc. of SPIE* **9892**, 98921W (2016).
[176]www.bostonscientific.com/content/dam/bostonscientific/Interventional%20Cardiology/portfolio-group/Imaging-Systems/opticross/L10_BC10213_Opticross_Spec_Sheet_150dpi.pdf
[177] A. Sanchez-Rubio, T.Y. Fan, S.J. Augst, A.K. Goyal, K.J. Creedon, J.T. Gopinath, V. Daneu, B. Chann, and R. Huang, "Wavelength beam combining for power and brightness scaling of laser systems," *Lincoln Laboratory Journal* **20** (#2) (2014).
[178] N. Lichtenstein, R. Baettig, R. Brunner, J. Müller, B. Valk, A. Gawlik, J. Bergmann, and F. Falk, "Scalable, high power line focus diode laser for crystallizing of silicon thin films," *Physics Procedia* **5**, Part A, pp. 109-117 (2010).
[179] C. Webb and J. Jones, "Handbook of laser technology and applications: laser design and laser systems," Vol. 2, *CRC Press* (2004).
[180] A.D. McAulay, "Military laser technology for defense: technology for revolutionizing 21st century warfare," *John Wiley & Sons* (2011).
[181] V. Sturm, H. G. Treusch, and P. Loosen, "Cylindrical microlenses for collimating high-power diode lasers," *Proc. of SPIE* **3097** (1997).

[182] L. Leggio, D.C. Gallego, S.B. Gawali, M. Sánchez, S. Rodríguez, M. Osiński, J. Sacher, G. Carpintero, and H. Lamela, "System analysis of wavelength-beam combining of high-power diode lasers for photoacoustic endoscopy," *Proc. of SPIE* **9888** (2016).
[183] J. Yu, L. Guo, H. Wu, Z. Wang, S. Gao, and D. Wu, "Optimization of beam transformation system for laser-diode bars," *Optics Express* **24** (#17), 19728 (2016).
[184] T.F. Fehm, X.L. Deán-Ben, P. Schaur, R. Sroka, and D. Razansky, "Volumetric optoacoustic imaging feedback during endovenous laser therapy – an ex vivo investigation," *Journal of Biophotonics* **9** (#9), pp. 934–941 (2016).
[185] T.J. Allen and P.C. Beard, "Dual wavelength laser diode excitation source for 2D photoacoustic imaging," *Proc. of SPIE* **6437** (2007).